Volume 2 , Issue 1, June 2016 ISSN 2356-8569

ACADEMY Publishing Center

Journal of
Renewable Energy and Sustainable Development

RESD

Academy Publishing Center
Journal of Renewable Energy and Sustainable Development (RESD)
First edition 2015

Permissions may be sought directly Academy Publishing Center, Arab Academy for Science, Technology, and Maritime Transport, Abu Kir Campus
Alexandria, EGYPT:
P.O. Box: Miami 1029
Tel:(+203) 5622366/88 – EXT 1069 and (+203) 561 1818
Fax: (+203) 561 1818
Web Site: http://apc.aast.edu

Volume 2, Issue 1, June 2016

ISSN: 2356-8518 Print Version

ISSN: 2356-8569 Online Version

ACADEMY Publishing Center

Journal of Renewable Energy and Sustainable Development

RESD

Renewable Energy and Sustainable Development (RESD) is a biannual international peer-reviewed journal which presents a global forum for dissemination of research articles, case studies and reviews focusing on all aspects of renewable energy and its role in sustainable development. The topics of focal interest to RESD include, but are not limited to, all aspects of wind energy, wave/tidal energy, solar energy, as well as energy from biomass and biofuel. The integration of renewable energy technologies in electrical power networks and smart grids is another topic of interest to RESD. Experimental, computational and theoretical studies are all welcomed to RESD.

Sustainable development is a multidisciplinary advancing to the center of energy research with the declaration of UN millennium development goals for the first time in 2000, and continued to constitute a challenge in energy technologies in the past decade. RESD is mainly interested in case studies of sustainable development and its relation to transition economies in the Middle East, Africa, Asia and Oceania.

RESD has an outstanding editorial board of eminent scientists, researchers and engineers who contribute and enrich the journal with their vast experience in different fields of interest to the journal. The journal is open-access with a liberal Creative Commons Attribution-NonCommercial-NoDerivatives 4.0 International License. Which preserves the copyrights of published materials to the authors and protects it from unauthorized commercial use or derivation. The journal is financially supported by Arab Academy for Science, Technology and Maritime Transporting in order to maintain quality open-access source of research papers on renewable energy and sustainable development.

Editorial Commitee

Table of Contents

Editorial Articles

Journal Articles

Journal of Renewable Energy and Sustainable Development (RESD)   Volume 2, Issue 1, June 2016 - ISSN 2356-8569
http://dx.doi.org/10.21622/RESD.2016.02.1.001

Developing Water Resources Within and Without Borders: Egypt's Road to Achieve Sustainable Development

Prof. Hossam Moghazy
Minister of Water Resources and Irrigation

Egypt is currently facing a significant challenge to strike a balance between the increasing demand of water and its available amounts; hence, the Egyptian Ministry of Water Resources and Irrigation has laid down a water policy that takes into consideration the present challenges and the future changes. To counter these challenges, this water policy is based on eight pivotal points as follows:

- Developing water resources within and outside borders in cooperation with the River Nile basin countries;
- Rationing water usage to make the best use of water resources;
- Improving water quality so as to protect the environment and citizens' general health;
- Supporting national projects and integrated development along with promoting investment and exports;
- Consolidating and rehabilitating facilities and water-lifting stations to guarantee optimal usage control, develop irrigation condition, and upgrade irrigation and drainage networks;
- Protecting coasts and facilities from climate changes and torrents threats; and
- Adopting the concept of water resources integrated management.

The Ministry of Water Resources and Irrigation strongly believes that developing water resources both within and outside borders is Egypt's road to achieve sustainable development, and therefore the Ministry adopts all scientific and executive measures to reach these goals for the welfare of Egyptian citizens.
I would like to thank the Renewable Energy and Sustainable Development Journal issued by the Arab Academy for Science, Technology and Maritime Transport Publishing House and to wish its board every success.
May God Almighty guide us towards the welfare of our beloved Egypt.

About Prof. Hossam Eldin Mohamed Murad Mughazy

Prof. Hossam Eldin assumed the portfolio of the Egyptian Ministry of Irrigation in September 2015. He got his baccalaureate with first grade of honours in 1982 and was granted his Master Degree in Science from the Faculty of Engineering, Alexandria University in 1985. In 1990, he obtained his PhD from the University of London, UK and Alex UNV on the topic: Optimal Well Design to Utilise Groundwater in Dry Areas.
Prof. Hossam Mughazy has been a professor of Irrigation and drainage Engineering since 2000 and held the position of the head of the Irrigation and Hydraulics Engineering Department at the Faculty of Engineering, Alexandria University in August 2010.
He has a lot of scientific publications and specialised articles published in a multiplicity of scientific periodicals and conferences in the fields of groundwater, irrigation and drainage engineering, as well as protecting the water environment. He has also supervised a lot of MSc theses and PhD dissertations in a number of Egyptian and Arab universities. Prof. Mughazy was awarded Alexandria University encouragement trophy in 1998.

Journal of Renewable Energy and Sustainable Development (RESD) Volume 2, Issue 1, June 2016 - ISSN 2356-8569
http://dx.doi.org/10.21622/RESD.2016.02.1.002

Silent Revolution in Research for Sustainability

Bruce Currie-Alder
Regional Director, Canada's International Development Research Centre (IDRC) in Cairo

Is research 'fit-for-purpose' for realizing sustainable development? More than two decades after the Brundtland report and UNCED Earth summit, the world has now adopted Sustainable Development Goals (SDGs). Rather than a cause for celebration, this delay should encourage reflection on the role of research in society. Why is it so difficult to realize sustainability in practice? The answer lies in the fact that universities and research centres persist with 19th century methods of data gathering, scholarly analysis, and journal articles. Today's world needs science in real-time, whether to detect drought, confront Ebola, or assist refugees. Research needs to work faster and embrace 21st century practices including data science, open access, and infographics.

A silent revolution is occurring in the ways of organizing and conducting research, enabled by new technology and encouraging work that tackles the key challenges facing society. A variety of new arrangements have come into existence that promote international collaboration, including Horizon 2020 with its emphasis on societal challenges, the Bill & Melinda Gates Foundation which has inspired a family of grand challenges funds on health and development, and the Future Earth joint program of research for global sustainability. These arrangements not only control billions of dollars in research funding, they also influence the strategies of national research councils and international organizations. The result is no less than a transformation in the incentives that reward how researchers invest their time and effort.

Why is a revolution needed? Within research, substantial growth in knowledge production coincided with fragmentation among disciplines. One can easily find expertise and publications in soil science or agronomy, yet integrated efforts on food security and climate adaptation remain scarce. Beyond research, society remains largely uninformed, as academics avoid engaging in public debate or policy advice. Research often fails to raise public awareness or inform practitioners regarding the issues facing society and the options for responding to them. For example, research on food security can and must go beyond quantifying how many people are hungry or undernourished. Society needs solutions that connect changes in farm-level production, to how the market mediates access to food, and the ultimate health outcomes among citizens.

The emerging vision is one where research helps society understand and respond to global problems. Research that is 'fit-for-purpose' demonstrates an ability to bridge ingenuity gaps, address grand challenges, and foster social resilience. Ingenuity gaps concern the knowledge needed to address rising complexity and new vulnerabilities introduced by globalization and technological change. Grand challenges describe a shift in the scale, scope, and ambition of research objectives. Social resilience refer to society's ability to cope with stress and reinvent itself in response to shocks and pressures. In short, Together these attributes describe an expectation that research helps society to 'mind the gap', 'think big', and 'bounce'.

Research needs to speak back to society. While the journal article and scholarly publications remain important determinants of a research career, they are increasingly supplemented by attention to data visualization, social media, and research impact. Research still needs rigour: deep knowledge of theory and data, and how to uncover patterns and establish explanation. Scientists have a long history of using pie charts, line graphs, and network diagrams to communicate among themselves. Yet research also needs a keen sense of design: an appreciation for how to convey relationships, categories, and magnitude through the creative use of lines, colours, symbols, position and size. Evidence-based illustrations, or infographics, convey complex issues in greater depth than long reports or TV commentaries. Research tells a story: starting with a compelling problem or question, and using data to provide perspective. Rather than offer society potential solutions or policy recommendations, newer techniques allow anyone to interact with data to create their own visualizations and test hypotheses “on demand”.

In summary, there is a silent revolution in research for sustainability. Research is expected to help understand and address the problems facing society. The opportunities to engage in research are shifting, rewarding those who are embrace the practices of open science and data, those who are connected to international scientific networks, and those that help society to better understand and solve global problems.

About Bruce Currie-Alder

Regional Director, based in Cairo, with Canada's International Development Research Centre (IDRC) which invests in knowledge, innovation and solutions to improve the lives of people in the developing world. Trained as an environmental scientist, he is an expert in natural resource management and on the policies that govern public research priorities and funding. Before joining IDRC, he worked on water governance, coastal management, and the oil industry in Latin America. His recent works include “Research for the Developing World” and “International Development: ideas, experience and prospects” (Oxford University Press). Bruce holds a PhD in Public Policy (Innovation, Science & Environment) from Carleton University. He is also member of the executive board of International Water Resources Association (IWRA), a network of multidisciplinary experts on water resources.

Journal of Renewable Energy and Sustainable Development (RESD) Volume 2, Issue 1, June 2016 - ISSN 2356-8569
http://dx.doi.org/10.21622/RESD.2016.02.1.004

Substantial Research Secures the Blue Future for our Blue Plant

Prof. Moustafa Abdel-Maksoud
Director, Institute for Fluid Dynamics and Ship Theory
Hamburg University of Technology (TUHH), Germany

Earth, the blue planet, is our home, and seas and oceans cover more than 70% of its surface. As the earth's population rapidly increases and available resources decrease, seas and oceans can play a key role in assuring the long-term survival of humankind. Renewable maritime energy has huge potential to provide a considerable part of the earth's population with decarbonised electricity generation systems. Renewable maritime energy is very flexible and can be harvested above the water's free surface by using offshore wind turbines, on the water's surface by using wave energy converters or below the water's surface by using current or tidal turbines. The supposed conflict between environmental protection measures and economic interests is neither viable nor reasonable. Renewable maritime energy can be the motor for considerable substantial economic growth for many maritime regions and therefore for society at large.

The fastest growing sector of renewable maritime energy is offshore wind. The annual report of the European Wind Energy Association from the year 2015 confirms the growing relevance of the offshore wind industry. In 2015, the total installed and grid-connected capacity of wind power was 12,800 MW in the EU and 6,013.4 MW in Germany. 38% of the 2015 annual installation in Germany was offshore, accounting for a capacity of 2,282.4 MW. However, there are a limited number of available installation sites in shallow water, meaning that there is an urgent need to develop new offshore structures for water depths greater than 50m. The persistent trend towards deeper waters has encouraged the offshore wind industry to look for floating wind turbine structures and larger turbines.

Floating wind turbine technologies are at an early stage of development and many technical and economic challenges will still need to be faced. Nonetheless, intensive research activities and the employment of advanced technologies are the key factors in accelerating the design process and ensuring the safe operation of floating wind turbines. In order to optimise the overall system, interdisciplinary numerical simulation methods are essential for evaluating the dynamic structure's behaviour. Due to the motion of the floating structure, the wind turbine design and the power generation system must be optimised to withstand high accelerations. Advanced control systems are crucial for maintaining a safe operation of the system.

Reducing costs is a main challenge for the offshore wind industry. One strategy in this effort is to assemble floating structure and the wind turbine onshore and then towing them out to sea. This procedure eliminates the need to use installation jack-up vessels with high crane capacity and therefore reduces overall installation time and costs. Floating structures are designed to accommodate large turbines; therefore, it should be expected that the final cost per MWh will be lower.

Another important resource of renewable maritime energy is wave energy. It has a considerable extracting potential and is available nearly up to 90 per cent of the time, which is not the case for wind and solar energy. However, there is no converged solution for the best method of extracting wave energy. Research in this area is still in a very early stage as compared to wind or solar energy technologies.
The main challenge in designing wave energy converters (WEC) is the strong fluctuation of the available

wave power levels, which can vary by a factor of 100. This means a WEC has to work efficiently at a low energy level and withstand extreme wave conditions that can occur once every few years. That is not only a structural problem but it is also a design problem with many challenges with respect to optimising the hydrodynamic behaviour of the system and the dynamic characteristics of the power take-off systems. The efficiency of a WEC can be significantly increased by using an adaptive active control of the power take-off. Current research focuses on the performance of the overall system, which includes developing new concepts for the WEC as well as the individual subcomponents of the system. This research is currently ongoing for developing advanced control approaches for efficiently extracting energy, and for developing concepts to minimise energy losses via the transmission of the slow reciprocating motion of the floating bodies into the rotary motion of the power generator and power transmission system.

Another attractive renewable maritime energy source is the tidal stream, the intensity of which has the benefit of being accurately predicted far in advance. Tidal energy is the oldest renewable maritime energy, with tide mills being used by the eighth century C.E. in many countries along the European west coast. Tides are very long waves, which take place twice a day and induce a movement of a huge amount of water. High current velocities can occur when the water enters certain confined areas such as bays or between two neighbouring islands. The tidal energy can be harnessed in such coastal areas using tidal turbine devices which are designed to extract kinetic energy from the tidal stream. The tidal turbine designs are very similar to wind turbines except that the rotor is driven by the tidal current. The rotor can be mounted on a founded or floating structure. As the density of water is more than 800 times higher than air, the diameter required of a turbine rotor to achieve a certain power is much smaller than a wind turbine rotor. Similar to a WEC, there is no converged solution for the best method of extracting wave energy but in the last years a number of promising concepts have been presented that can be further developed. While implementing reliable tidal turbine designs with low installation and operation costs still requires more time and research, tidal turbines are an attractive solution for some coastal locations far from the public electricity net, such as small islands or holiday regions.

In some coastal regions, the geographical conditions allow for building a near shore tidal dam to accumulate tidal water. The water enters the dam at high tide and leaves it at low tide. The tidal energy can be harnessed by using conventional water turbines which convert the hydraulic power into electric power. The turbines in this case are well developed and therefore only some minor improvement are necessary. The cost of constructing the tidal dam is high; however, the operation costs are relatively low. A tidal dam can have a strong Influence on aquatic life and therefore the environmental impacts of such a project must be investigated very accurately.It is therefore essential to intensify the research and development activities on renewable maritime energy technology to make the vision of a blue future for our blue planet to become reality.

About Prof. Moustafa Abdel-Maksoud

Professor Moustafa Abdel-Maksoud is the head of the Institute for Fluid Dynamics and Ship Theory at Hamburg University of Technology in Germany. He is well-known for his contributions to a wide range of hydrodynamic analysis and experiments in the area of naval architecture and ocean engineering. His recent research interests include ship hydrodynamics and dynamics; design and optimization of ship propulsion systems; Fluid-Structure Interaction and Renewable Maritime Energy. Prof. Maksoud is the leader developing *pan*MARE in-house panel code with wide industry applications. He has leaded and coordinated various national and EU projects. The most relevant project in the renewable energy area is Maritime Safety Aspects Regarding Installation and Maintenance of Offshore Wind Turbines supported by Research and Science Foundation Hamburg.

Prof. Moustafa Abdel-Maksoud obtained a B.Sc. in Marine Engineering and Naval Architecture at Alexandria University in 1982. He took his M.Sc. at the same, and then studied for his doctorate which he obtained in 1992 at the TU Berlin. Following research positions and headship at Potsdam Model Basin, he became Professor at the Institute of Ship Technology and Transport systems, Duisburg-Essen University in 2003, and subsequently became Head of Institute of Fluid dynamics and Ship Theory, TUHH in 2007. Prof. Abdel-Maksoud is a member of numerous professional associations.

Journal of Renewable Energy and Sustainable Development (RESD) Volume 2, Issue 1, June 2016 - ISSN 2356-8569
http://dx.doi.org/10.21622/RESD.2016.02.1.005

Comparative Study of Modulation Techniques for Two-Level Voltage Source Inverters

P Li, G P Adam, Member IEEE, D Holliday and B W Williams
University of Strathclyde, Glasgow, United Kingdom.
peng.li@strath.ac.uk

***Abstract* -** A detailed comparative study of modulation techniques for single and three phase dc-ac inverters is presented. Sinusoidal Pulse Width Modulation, Triplen Sinusoidal Pulse Width Modulation, Space Vector Modulation, Selective Harmonic Elimination and Wavelet Modulation are assessed and compared in terms of maximum fundamental output, harmonic performance, switching losses and operational mode. The presented modulation techniques are applied to single and three phase voltage source inverters and are simulated using SIMULINK. The simulation results clarify the inverter performance achieved using the different modulation techniques.

***Keywords* -** Modulation techniques, two-level voltage source inverter, comparative study, fundamental and harmonics.

I. INTRODUCTION

The most recently proposed modulating strategies are generally for application in complicated cascaded modular inverters, matrix converters or other novel converter configurations [1-4]. However, all these modulation strategies are based on classical theory and techniques, such as Sinusoidal Pulse Width Modulation (SPWM), Space Vector Modulation (SVM) and Selective Harmonic Elimination (SHE).

Wavelet modulation (WM) theory has been proposed [5, 6], in which it is claimed that wavelet based PWM has advantages over traditional modulation strategies, specifically SPWM, SVM and SHE. Some of the claimed advantages are [5]: extension of the modulation index linear range beyond that possible with SHE and SVM, and five-level line-to-line voltage waveform, hence low harmonic content and dv/dt. Tri-state leg output voltages are assumed from a two-level voltage source inverter with an inductive load [5], yet this condition can only be created with PWM current source inverters. The implication of such a tri-state condition is that a large capacitive output filter must be connected to ensure that load current is continuous. In addition, the new wavelet PWM technique is not suitable for variable speed drive applications since the modulation index can only vary within a narrow range, which is limited by the switching frequency. In an attempt to clarify some of the claims relating to WM [5, 6], this paper presents a detailed comparison between wavelet based and traditional PWM strategies. The comparison considers maximum attainable fundamental output voltage, harmonic performance based on weighted total harmonic distortion (wTHD), switching frequency per device and operational mode. The comparison uses wTHD rather than THD since it better reflects the individual voltage harmonics in the load current.

II. REVIEW OF INVERTER VOLTAGE MODULATION TECHNIQUES

Two-level voltage-source-converter modulation techniques have been intensively researched. In principle, all modulation methods aim to lower harmonic distortion in the output voltage and current, improve dc link utilization, and minimize switching losses, among which there is a trade-off in order to achieve balanced inverter performance under all operating conditions. The three-phase bridge converter in Fig.1 is widely employed in low and medium voltage applications.

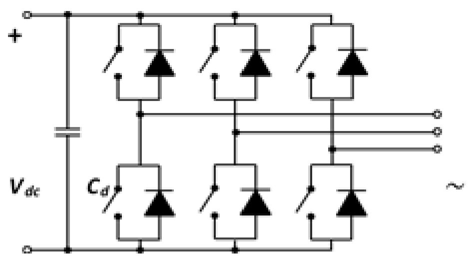

Fig .1. Three-phase voltage source inverter

Generally, SPWM generates a train of pulses having a volt-second area the same as that of the reference signal over one switching or fundamental period. Its disadvantages are that the maximum linear modulation index is limited to 1pu (4/π being that for a square-wave fundamental) and that the switching devices experience the full carrier frequency. Third harmonic (or triplen) injection SPWM (TSPWM) extends the maximum modulation index to 1.155pu, but inherent are all the other features of SPWM as well as the introduced zero-sequence components in the phase voltages that do not contribute to the three-phase load currents. SVM is developed from the space vector representation of the inverter output voltage in the α-β plane. DC voltage utilization is 1.155pu. The technique offers additional flexibility in terms of pulse placement and switching pattern selection, hence switching losses can be optimized. SVM is suitable for real-time and digital implementation. SHE controls the fundamental voltage and eliminates specific harmonics by directly calculating the switching instants. In this manner, SHE can generate high quality output voltage at a lower switching frequency when compared to other methods, and a relatively high modulation index is achievable in three-phase systems.

The WM method defines the linearly combined scaling function (1) to generate a train of rectangular pulses with various widths and shifts.

$$\varphi_j(t) = \phi_H(2^{j+1}t) + \phi_H(2^{j+1}(t-1+2^{-(j+1)})) \qquad (1)$$

where scale j is defined as j=1, 2, 3, ... and φ_H is the Haar-scaling function [5]. The scale-base linearly combined synthesis scaling function at scale j is defined by (2) [5].

$$\tilde{\varphi}_j(t) = \phi_H(t) - \varphi_j(t) \qquad (2)$$

Fig.2. illustrates the generation of WM modulation gating signals using (1) and (2).

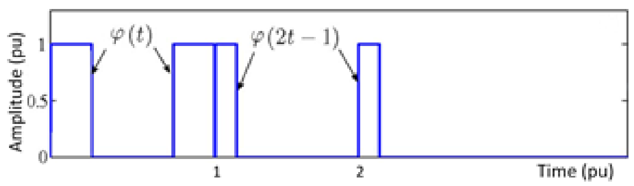

(a) switching instants calculated by defined scaling function (1)

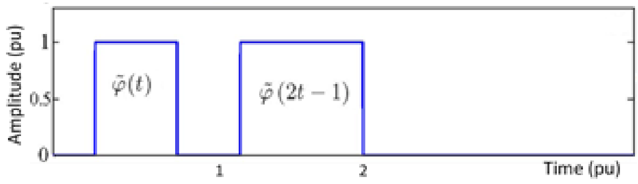

(b) synthesis scaling function for gate signals defined in (2)

Fig .2 Basic functions in wavelet modulation theory

Reference [5] shows that the three-phase inverter output line voltage has five voltage levels, which means that the phase voltage must be 3-level. This is not achievable with an inductive load.

In open-loop applications, WM can be implemented on-line since, advantageously, the real-time calculations are linear and can be solved by a processor without significant delay.

The switching frequency fsw with the WM method is determined by the maximum scale value J, as shown in (3) where f0 is the fundamental frequency, and where quarter-wave and half-wave symmetrical output waveforms can be obtained. The output voltage contains no even order harmonics.

$$f_{sw} = (4J-1)\, f_o \qquad (3)$$

The modulation index, related to half of the dc bus voltage, V_{dc}, for WM, can be determined by **Error! Reference source not found.** where V_{p1} is the peak line-to-line fundamental voltage, j = 1, 2... J and (t_{j1}, t_{j2}) = (j+$2^{-(j+1)}$, j+1-$2^{-(j+1)}$) are the switching instants on a normalized time axis used to define the new scale-based linearly-combined scaling function.

$$m_a = \frac{V_{p1}}{\frac{1}{2}V_{dc}} = \frac{4}{\pi}\left(2\cos(\xi t_{J1}) - 1 + 2\sum_{j=1}^{J-1}(\cos(\xi t_{j1}) - \cos(\xi t_{j2}))\right) \qquad (4)$$

where $\xi = \dfrac{\pi}{2J-1}$.

From (3) and (4), the switching frequency and modulation index for WM are coupled by the maximum scale J, which means the output voltage can only be adjusted in a narrow range to avoid an irrational switching frequency.

http://dx.doi.org/10.21622/RESD.2016.02.1.005

Fig.3 plots the theoretical variation of modulation index with J. It can be concluded that the modulation index limit for WM is 1.273 (4/π): the same as with square wave inversion. The available modulation index range is, however, limited to 0.95-1.15, corresponding to J varying discretely between 5-10. If J exceeds this recommended range, low-order voltage harmonics are observed to increase rapidly, where these harmonics exhibit fixed leading or lagging phase shifts with respect to the fundamental.

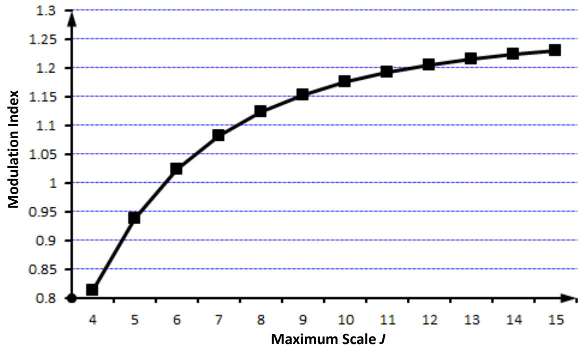

Fig .3 Theoretical modulation index versus maximum scale J for WM

III. COMPARATIVE STUDY OF MODULATION METHODS

In this comparison, the inverter of Fig.1 with V_{dc} =100V and f_0=60Hz, as detailed in Table I, is the basis for the simulation study. Five modulation techniques: SPWM, TSPWM, SVM, SHE and WM are analyzed.

The dc voltage utilization coefficient *λ*, defined by **Error! Reference source not found.**, specifies the voltage transfer limit and is inherently restricted to 1.1 for a square wave mode.

$$\lambda = \frac{V_{p1}}{V_{dc}} \qquad (5)$$

Harmonic performance is usually evaluated using THD. Since low-order harmonics contribute the most significant current components to the load, wTHD is used in this case to determine the effective harmonic content of the output voltage waveform. The method for calculating wTHD is shown in (6), with an upper limit of the 75th harmonic being specified for this comparative study.

$$wTHD = \frac{\sqrt{\sum_{n=2}^{\infty}\left(\frac{V_{np}}{n}\right)^2}}{V_{p1}} \qquad (6)$$

Fig.4 shows the output voltage waveforms for the wavelet modulated VSI. For different modulation methods at maximum linear output, the various positions and widths in the rectangular pulses contribute to the different spectra, as indicated in Fig.5. The dc bus voltage is the base used to normalize the spectral component magnitudes, thereby allowing performance comparison between each modulation method. The detailed and quantitative results for the output fundamental and harmonic component amplitudes are shown in Table I. For each of the five modulation techniques investigated, the table also shows dc voltage utilization, the amplitudes of the first eight significant harmonics expressed as a percentage of the fundamental and the WTHD.

A. SPWM:

Fig.5 (a) shows the spectrum of output line-to-line voltage for SPWM and that all of the significant harmonics are concentrated around the sidebands of the switching frequency components. The maximum dc voltage utilization is 86.6% and WTHD is 1.57%, as shown in Table I.

B. TSPWM:

As shown in Fig.5 (b) and Table I, injection of the 3rd harmonic into the modulating wave extends the linear modulation index to 115.5% of that of SPWM and that the output 3rd harmonics in each phase are cancelled by the three-phase configuration. The wTHD is decreased to 1.36% due to the increased fundamental component.

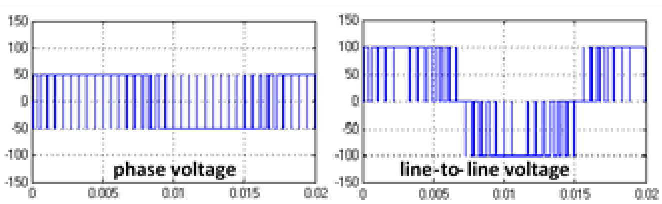

Fig 4. Output voltages for a two-level VSI with WM (J=8) horizontal axis: Time (ms); vertical axis: Voltage (V)

C. SVM:

SVM generates waveforms with a similar maximum fundamental output to TSPWM, as shown in Fig.5 (c) and Table I. The corresponding WTHD is 1.35%. However, there will be deviation from the ideal situation as the sidebands around the first switching frequency manifest as low order harmonics.

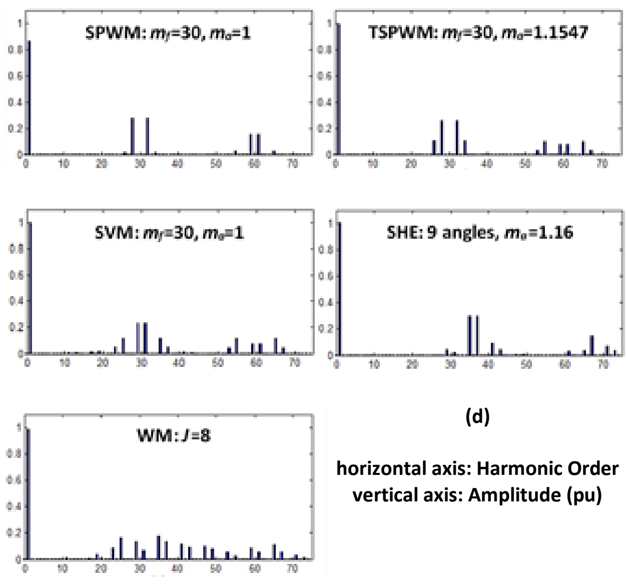

Fig 5. Line-to-line voltage spectra for different modulation methods (peak value normalized to Vdc) versus Harmonic order

D. SHE:

The WTHD under SHE modulation with an equivalent switching frequency of 19 times the fundamental (which is lower than for the other methods) is 1.24%, and the first significant harmonics are the 29th and 31st, as shown in **Error! Reference source not found.** I and Fig.5 (d). By design, the low-order harmonic amplitudes are all close to zero and the fundamental peak is slightly higher than those for SVM and TSPWM. By constraining the maximum linear modulation index to 1.16, nine controllable switching angles eliminate up to the 25th order harmonic.

E. VM:

With WM, the maximum scale J offers the only degree of freedom with which to determine the switching frequency, the modulation index and the location of each switching edge. From Table I, the WTHD for WM is 1.28%, and the fundamental peak value is slightly lower than for SVM for a similar switching frequency as used in the SPWM, TSPWM and SVM cases. The limitation of wavelet modulation theory is, however, the lack of harmonic distribution control, with the result that the low-order harmonic content can be significant. Fig.5 (e) shows that the significant harmonics are distributed over a wide range of the spectrum and, adversely, in the vicinity of the baseband. As a result, large output filters, which are expensive and complex to design, are needed to achieve acceptable harmonic levels specified by IEEE and IEC standards.

Fig.6 shows output line-to-line voltage THD for SPWM, TSPWM, SVM, SHE and WM as a function of modulation index, where TSPWM, SPWM, SVM and WM all have the same switching frequency. In most modulation methods, the THD and WTHD decrease with increasing modulation index. However, the THD (and the wTHD) characteristic for WM would not be monotonic since operation over the entire range of modulation index requires a change in J, as shown in Fig.3, which in turn modifies the harmonic profile of the WM scheme.

The total number of commutations per cycle directly influences device switching losses. SVM offers the capability to optimize the switching sequence, hence switching losses can be minimized. SHE offers the lowest switching frequency, while its harmonic performance is better than that of the other modulation methods. However, switching losses are generally determined not only by the switching frequency but also by the distribution of switching instants and by the load current at each switching instant.

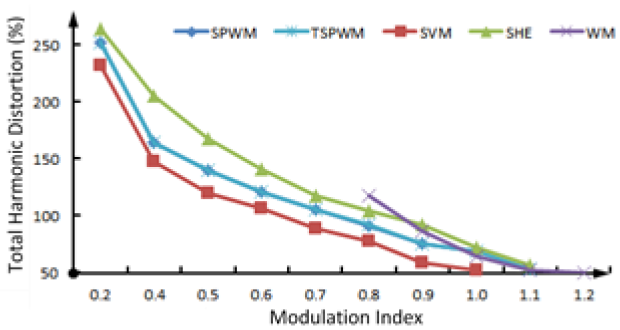

Fig 6. Total Harmonic Distortion versus Modulation index

Realization of each modulation technique can be achieved either on-line and in real-time or off-line using a pre-

http://dx.doi.org/10.21622/RESD.2016.02.1.005

calculated look-up table. The on-line or real-time implementations can be supplied by directly observed variables, facilitating a highly accurate control strategy. However, significant real-time calculation increases processor requirements and the digitization process can introduce distortion, such as low order harmonics. An off-line or look-up table implementation employs several pre-computed local-data tables to avoid on-line calculation, making any control decision instantaneous. The penalty is reduced control flexibility, or reduced accuracy if interpolation between stored data points is required. In addition, a large quantity of data must be downloaded into read-only memory prior to inverter activation. When incorporating feedback to control voltage source inverters, the run mode of each modulation method influences the practicality and the realization complexity due to the principle of the modulating method itself. Table II lists the recommended operational closed-loop modes, accounting for algorithm complexity and commercial processor speeds. With SPWM, TSPWM and SVM the dc voltage utilization coefficient is linearly dependent on modulation index over a wide range, making control calculation simple and efficient. Given the speeds of currently available processors, an on-line operational mode is viable, with remaining processor capacity available to monitor all status parameters and variables.

Table 1. SIMULATION RESULTS FOR DIFFERENT MODULATION METHODS

V_{dc}=100V, f_o=60Hz																				
	Three-Phase Voltage Source Inverter												Single-Phase H-Bridge Voltage Source Inverter							
Modulation Technique	SPWM m_f=30 m_a=1		TSPWM m_f=30 m_a=1.1547		SVM m_f=30 m_a=1 Sequence #2		SHE m_a=1.16 9 angles		WM max. scale J=8		Square-Wave Inversion		SPWM m_f=30 m_a=1, Unipolar		SHE m_a=1.2135 3 angles Unipolar		WM max. scale J=8 Unipolar		Square-Wave Inversion	
f_{sw} (kHz)	1.8		1.8		1.8		1.14		1.86		0.06		1.8		0.42		1.86		0.06	
λ (V_{1p} /V_{dc})	0.866		0.9977		0.9977		1.0046		0.9898		1.1026		0.9998		1.2134		1.208		1.2732	
THD (%)	68.62		52.62		52.55		56.66		53.33		31.09		53.06		37.05		45.04		48.35	
First 8 significant harmonics V_{1p} = 1pu	order	V_p (%)	order	V_p (%)	order	V_p (%)	order	V_p (%)	order	V_p (%)	order	V_p (%)	order	V_p (%)	order	V_p (%)	order	V_p (%)	order	V_p (%)
	26	1.8	26	10.43	17	1.4	29	4.61	11	1.63	5	20	25	2.79	3	22.24	3	23.62	3	33.34
	28	31.79	28	25.94	19	1.95	31	2.01	17	1.05	7	14.28	27	18.19	5	5.43	5	11.2	5	20
	32	31.79	32	25.94	23	5.44	35	30.01	19	3.98	11	9.09	29	16.45	7	1.81	7	6.95	7	14.29
	34	1.83	34	10.41	25	11.92	37	29.55	23	9.02	13	7.69	31	16.48	9	3.49	9	5	9	11.11
	55	3.35	53	3.54	29	23.37	41	9.11	25	16.59	17	5.88	33	18.18	11	5.27	11	4.47	11	9.09
	59	18.15	55	10.27	31	23.38	43	4.53	29	13.59	19	5.26	35	2.78	13	3.82	13	3.74	13	7.69
	61	18.13	59	7.55	35	11.89	47	1.19	31	6.81	23	4.35	53	4.18	15	1.31	15	3.76	15	6.67
	65	3.3	61	7.57	37	5.38	61	3.6	35	18.17	25	4	55	10.3	17	7.88	17	4.06	17	5.88
wTHD (%)	1.57		1.36		1.35		1.24		1.28		4.64		1.21		7.54		8.34		12.11	

To implement SHE and WM, significant arithmetic processing is required, therefore off-line techniques using look-up tables and interpolation are employed. The switching instants for different modulation indices are stored as local data so that a specific output voltage can be obtained by an interpolation method. The technical feasibility of WM in closed-loop operation is restricted by a narrow modulation index range. WM cannot be used when, for example, the inverter is required to offer black-start capability.

Table 2. OPERATION MODE COMPARISON FOR EACH MODULATION METHOD

Recommended Closed-loop Operation Mode		
Modulation	SPWM/TSPWM/SVM	SHE/WM
Run-mode	On-line	Off-line

IV. CONCLUSION

Five modulation techniques, viz. SPWM, TSPWM, SVM, SHE and WM, have been analyzed in order to provide a detailed review of their performance.
Low dc link voltage utilization is the main problem with SPWM, but this shortcoming is overcome with TSPWM and SVM. With SHE, 9 angles (19 switching actions per cycle) eliminates harmonics up to 25th order and provides a higher fundamental output. The performance of WM in three-phase situations is no better than that of SVM and may require a large ac filter to meet IEEE and IEC harmonics standards.

A disadvantage associated with the WM technique is the narrow range over which the modulation index may be adjusted for a given value of J, which may hinder its closed-loop use. Additionally, Table I shows that for the single-phase case SHE better utilizes the DC link voltage, and has reduced THD and wTHD at a significantly lower switching frequency when compared to WM. Multiple SHE solutions exist which provide further improvements over WM. The limitations and operating features highlighted as part of this analysis of WM are inconsistent with the claims made elsewhere [5, 6] regarding its performance. For example, this study was unable to replicate the 5-level line-to-line voltage waveforms theoretically, in simulation or practically from the standard six-pulse three-phase inverter, with an inductive load, as presented in [5].

To conclude, for a given average switching frequency, SHE modulation provides the best performance for three-phase inverter applications, with high-quality output and optimal circuit operation. Local data look-up with interpolation has been proven to be robust in closed-loop operation.

REFERENCES

[1] C. Govindaraju and K. Baskaran, "Efficient Sequential Switching Hybrid-Modulation Techniques for Cascaded Multilevel Inverters",Power Electronics, IEEE Transactions on, vol. 26, pp. 1639-1648, 2011.

[2] P. Kiatsookkanatorn and S. Sangwongwanich, "A Unified PWM Method for Matrix Converters and Its Carrier-Based Realization Using Dipolar Modulation Technique", Industrial Electronics, IEEE Transactions on, vol. 59, pp. 80-92, 2012.

[3] K. Kobravi, R. Iravani and H.A. Kojori, "Three-Leg/Four-Leg Matrix Converter Generalized Modulation Strategy - Part I: A New Formulation", Industrial Electronics, IEEE Transactions on, vol. 60, pp. 848-859, 2013.

[4] B. York, Y. Wensong and L. Jih-Sheng, "Hybrid-Frequency Modulation for PWM-Integrated Resonant Converters", Power Electronics, IEEE Transactions on, vol. 28, pp. 985-994, 2013.

[5] S.A. Saleh, C.R. Moloney and M.A. Rahman, "Analysis and Development of Wavelet Modulation for Three-Phase Voltage-Source Inverters", Industrial Electronics, IEEE Transactions on, vol. 58, pp. 3330-3348, 2011.

[6] S.A. Saleh, C.R. Moloney, and M.A. Rahman, "Development and Testing of Wavelet Modulation for Single-Phase Inverters", Industrial Electronics, IEEE Transactions on, vol. 56, pp. 2588-2599, 2009.

http://dx.doi.org/10.21622/RESD.2016.02.1.012

Control and Management of Energy in a PV System Equipped with Batteries Storage

Kamal Hirech , Mustapha Melhaoui, Khalil Kassmi* and Rachid Malek

* Laboratory LETSER, Dept of Physics, Faculty of Science, University Mohamed I, Oujda, Morocco.

E-mail: khkassmi@yahoo.fr

Abstract - In this paper the researchers present a work concerning the conception, implementation and testing of a photovoltaic system that is equipped with a new concept of control and management of energy in a PV system with battery storage. The objective is to exploit the maximum of power using Hill climbing improved algorithm that considers optimal electrical characteristics of PV panels regardless of the system perturbation, to manage the energy between blocs of PV system in order to control the charge/discharge process and inject the energy surplus into the grid and also to estimate the state of charge with precision. Moreover, the system guarantees the acquisition and presentation of results on computer, supervision and so on. The results obtained show the robustness of the PV system, good control and protection of batteries under the maximum of energy provided by the PV panels. The state of charge estimation is evaluated by using measured parameters in real time; it shows an improvement of around 5% compared to the conventional technique.

Keywords - regulator; photovoltaic system; charge/discharge; Battery; SoC, MPPT; Converter.

I. INTRODUCTION

Nowadays, there are many works about photovoltaic systems (PV) that operate the energy in order to inject it into the grid [1] or in the stand-alone installations. [2]

The autonomous systems or those connected to the grid [1-3] are equipped with batteries in order to satisfy the needs of the local demand of energy [4] or facilitate coupling and solve the problems of adaptation between production and demand [3-4]. The major challenges for these structures are the protection, stability and storage of energy when the batteries are fully charged. However, those batteries suffer from various types of degradation due to their bad use, a bad control of charging/discharging, and the impact of temperature.

So, all optimization of the life-time of the battery requires a system to control and manage its functioning.

In This paper, the researchers study a structure of a photovoltaic system equipped with a new concept to control and manage the energy supplied by panels in the charge/discharge process with a good precision of the state of charge estimation (SoC), this is by a regulation system based on: Firstly the hash of current supplied by panels via a PWM signal controlling the switch Buck or Boost DC/DC converter to maximize the power to the output and secondly, the hash of current supplied to the output of the converter to charge the batteries.

A part of energy produced and unabsorbed by the batteries during the charging is injected into the grid with the minimum of energy loss. All functioning tasks of this system, which are under optimal conditions by maximization of the power transferred to the converter output, increase the rapidity of charging and improve efficiencies by an improved Hill climbing algorithm of MPPT, taking into consideration the optimal electrical characteristics of panels. The state of charge SoC determination is achieved by the combination of two methods to correct estimation errors and to increase precision. The initialization of SoC is fixed by the method of open circuit voltage (OCV) [5] when the batteries are at rest: a first recalibration of the SoC is applied. The quantity of charge absorbed or delivered by the batteries is calculated by the Coulomb Counting method in real time [6] and a second recalibration of the SoC is applied when the batteries reach full charge conditions. The proposed method is characterized by being simple and easy to implement and does not require the use of additional hardware.

The various measurements and parameters will be displayed on an LCD and transferred through a serial connection to a computer [7].

II. FUNCTIONING OF THE PV SYSTEM

A. Architectural PV system

The synoptic diagram of the PV system designed and tested (Fig. 1) consists of various:

- Two PV panels mounted in parallel [7].
- Two lead acid solar batteries in series.
- DC or AC load through a DC/AC converter (lamp,...)
- A DC/DC Boost (or Buck) converter to adapt the PV panels to the batteries [7].
- The management and supervision system (MSS), which is based on the use of a microcontroller to perform all the tasks of: optimization of the system functioning by the MPPT control, regulation of charge/discharge process, control of the energy transfer between various blocs, acquisition and display of different quantities (voltages, currents, powers, SoC, performance, illumination, and temperature) on the screen of a PC or LCD and communication to the computer by a serial link [7].
- Block of energy flow controller, formed by three power circuit (circuit 1 to 3) presented in Fig .1.

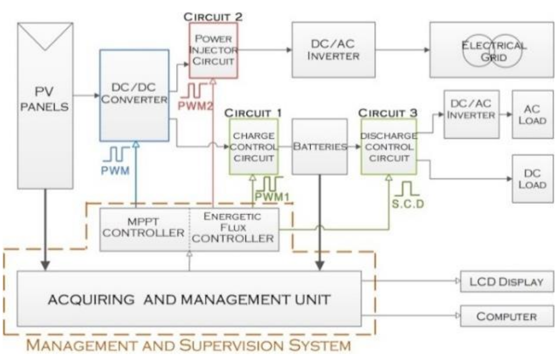

Fig .1. Synoptic diagram of the PV system designed.

B. The MPPT control

The MPPT control, which is characterized by its robustness and precision [8], generates a PWM signal of a frequency of 10 kHz with variable duty cycle α. Its main role is to converge instantly the functioning point of the PV panels to the MPP, regardless of weather or load variations. The principle is to take into account the performance of the PV panels. The improvement provided is to search the PPM in an optimal voltage range which is previously determined by the user depending on panels used and weather conditions, in our case between 12V and 16V. This algorithm is based on the determination of the system evolution from the sign of dPpv / dt generated by the panels that forces the system to search MPP between (Vmin, Vmax) by executing the algorithm in Fig. 4. This is by a flow test of the timer TM and the verification of the state of the signal Vstate which allows, at the end of the algorithm, to increment the duty cycle if Vstate = 1, or to decrement it if Vstate = 0.

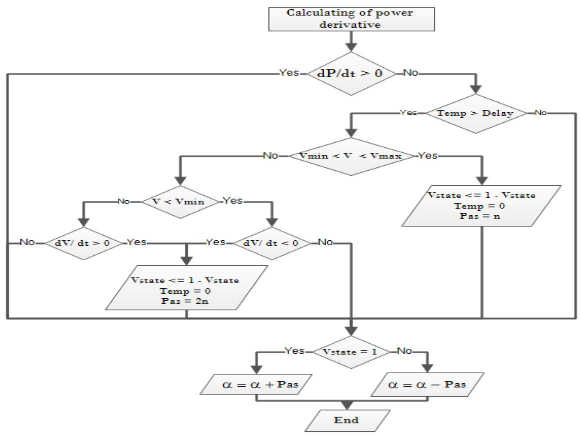

Fig .2. The MPPT algorithm used in this work [8].

C. Regulation of charging/ discharging process

The method proposed in this work for the control of energy provided by the PV system is carried out by hashing current supplied to the output of the converter by PWM signals. This energy is used to charge the batteries following three phases described by the algorithm in Fig. 3 and the surplus is injected into the grid. In the case at hand, the charge process is done by using the technical characteristics of the batteries shown in Table 1.

The discharging control of batteries is based on the situation of the installation using the algorithm of Fig. 4. This process is activated/deactivated on the basis of batteries estimation of state of charge SoC:

- If the SOC reaches the limit value SoCmin.D, the process of discharge will stop,
- If the SOC is higher than SoCmin.R, the discharge

Journal of Renewable Energy and Sustainable Development (RESD) Volume 2, Issue 1, June 2016 - ISSN 2356-8569
http://dx.doi.org/10.21622/RESD.2016.02.1.012

process will be activated,

- If SoCmin.D is <SoC< SoCmin.R, the situation of the installation will determine the charge/discharge process. If the discharge takes place following the normal cycle (dSoC/dt≤0), the batteries will discharge until SoC=SoCmin.D (Table 1). If a new charge cycle takes place (dSoC/dt>0), the discharge will be blocked until the SoC reaches SoCmin.R.

Table 1. ELECTRICAL CHARACTERISTICS AND VALUES CHARGE/DISCHARGE PARAMETERS OF BATTERIES AT 25 °C.

Characteristics and conditions of charge	***Batteries of 12 cells***
Nominal voltage	*24V*
Nominal capacity	*110Ah*
Voltage of regulation V_R	*28.4V*
Voltage of floating V_{FLT}	*27,3V*
Current of over charge terminate I_{OCT}	*1A*
Limit Voltage of discharge ***LVD***	*22.8V*
State of charge. minimum to disconnect ***SoCmin.D***	*40%*
State of charge. minimum to reconnect ***SoCmin.R***	*45%*

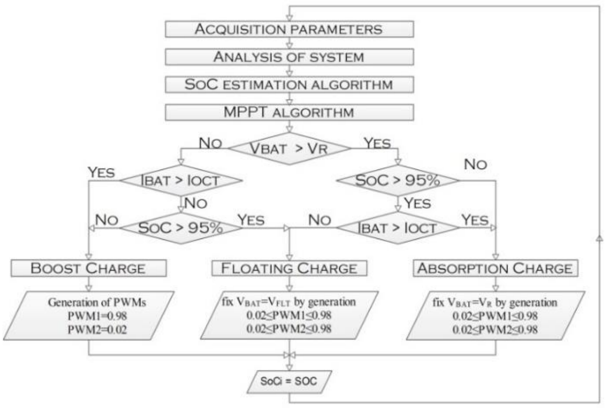

Fig .3. Control algorithm of the batteries charge.

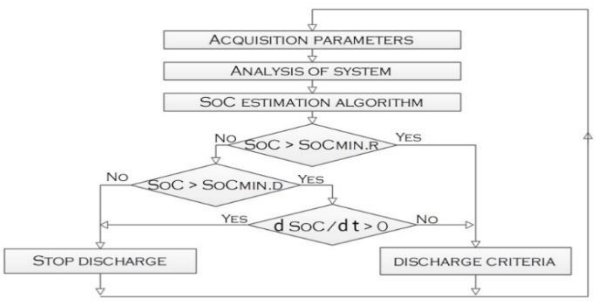

Fig .4. Control algorithm of the batteries discharge.

D. State of charge estimation

For a good energy management of batteries, the system must be equipped with an estimation model of the state of charge in order to know the real state of the battery during its use. In this system, this is guaranteed by a model that incorporates the use of two methods for a good estimate. For a battery of a nominal capacity Qo, the initial state of charge SoCi is estimated by the OCV method [9].

The quantity of charge absorbed or delivered is calculated by an algorithm that integrates the current during the charge (I_{BAT}) and discharge (Idech) as a function of time and taking into consideration the faradaic efficiency (η). A recalibration of SOC is activated when the batteries reach the condition of the final charge as they are fully charged to minimize errors of integration and the effects of temperature. During the charge/discharge, the expression of the SoC is [10]:

$$\mathrm{SoC(t)} = \mathrm{SoCi} + [100\%/\mathrm{Qo}] \times \left| \int (\eta \times Ibat(t) - Idech(t))dt \right| \quad (1)$$

The initial state of charge is determined by OCV method following the empirical equation (Eq.(3)) [11]:

$$\mathrm{SoCi(T)} = \mathrm{SoC(25°C)} \times (1 + 0.003 \times (T - 25)) \quad (2)$$

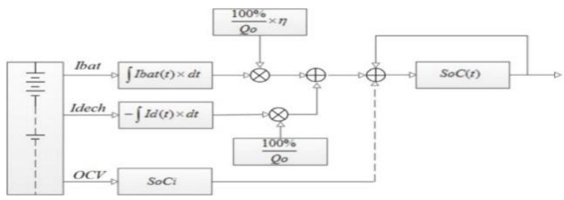

Fig .5 The proposed method to estimate the state of charge SOC.

III. EXPERIMENTAL RESULTS

A. Experimental procedure

Fig. 5 presents the fully automated bench of electrical measurement and the PV system designed and tested when this system is equipped by:

- Two monocrystalline PV panels mounted in parallel. Each one provides, under optimum conditions, a power of 65W at the voltage 14.2V and a current of 4.4 A. [7].

- Two lead acid batteries mounted in series. Each one has a nominal voltage and capacity of 12V and 110Ah.

- A DC / DC boost converter dimensioned to operate at a frequency of 10 kHz, a power of about 200 W and a current ranging between 1A and 10A [7].
- A management and supervision system (MSS) (Fig. 6), which allows management of the acquired data to control the communication between the different blocks of the PV system. This ensures a good functioning of the MPPT control, regulation, control of the energy flow and estimation of the SoC. In addition, it displays all electrical parameters and control switches. A serial link is used to transfer data and store them in a computer.

- The power circuits (circuits 1 to 3) controlled by PWM signals whose form ensures the good functioning of energy transfer.

- A weather station equipped with a pyranometer and temperature sensor.

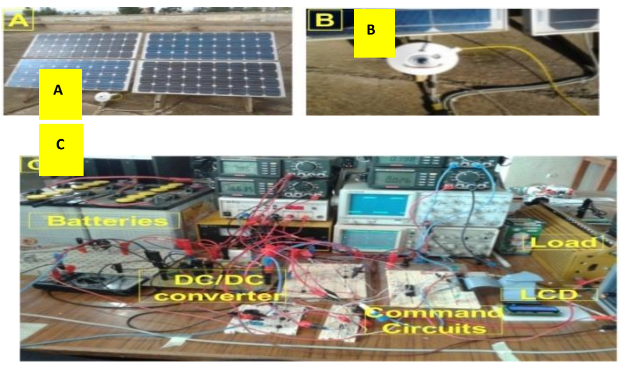

Fig .5 The photovoltaic system designed and digital bench of measurement installed at the Laboratory: (A): photovoltaic panels. (B): pyranomete. (C): designed system (batteries, converter, measurement instrument, LCD…).

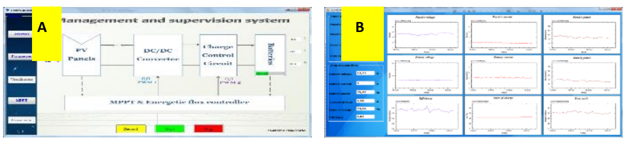

Fig .6 Management and supervision system: (A): global interface. (B): electrical quantities visualization.

B. Energy flow management in the PV system

1. Batteries regulation charge

During 8 days (D1 to D8), the batteries charging system conceived is analysed (Fig. 5) where the irradiance reaches 800 W/m2 (Fig. 7). At first, When the system starts functioning, the acquisition interface performs measurements of batteries voltage under the conditions of open circuit (OCV =24.28V), and then calculates the SoCi. The interface displays a SoCi =42%. Fig. 8 and Fig. 9 present different results obtained that show:

- During Boost phase (0h to 38h) (Fig. 8): the batteries are charged with a current IBAT that reaches 2 A towards midday. The voltage VBAT and SoC increase until the threshold limit VBAT = VR . The SoC shows that more than 90% of the battery capacity is recovered during this phase (Fig. 9). In the same figure of the SoC, the values obtained by the two methods, that was proposed in this work (Eq.(1)) and OCV method [5] are traced. This latter (the OCV method) requires a very long period of rest. This reflects the estimation errors observed. However, the proposed method does not require a rest period except in the calculation of the SoCi. So a difference of the order of 5% appears between the two methods. The SoC values estimated by the proposed method coincide perfectly with those concluded from the batteries when these last enter in a long period of rest. Improvement of obtaining SoC by our method as compared to the conventional method can be estimated at 5%.

- During the absorption phase (38h-50h) (Fig. 8): The batteries are charged by current pulses IBAT in order to fix VBAT around 28.4V to complete the charging of batteries up to SoC = 95% (without reaching overcharge). At this phase (Fig. 9), the SoC increases slowly due to the progressive decrease of the charge current absorbed by the batteries. The end of this phase is determined by a SoC of over 95% and a current above IOCT = 0.8A. During this phase, the surplus of energy is injected into the grid.

- During the floating phase (50h to 55h) (Fig. 8): the batteries are fully charged (Fig. 9). To compensate self-discharging, the system provides the charge through current pulses of low value (0.3A) around the float voltage VFLT=27.3V (away from the gassing range). So, the totality of the energy is injected into the grid (the batteries absorb a low quantity of energy).

http://dx.doi.org/10.21622/RESD.2016.02.1.012

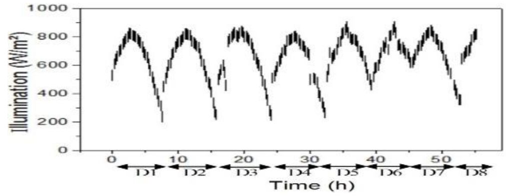

Fig .7 The typical illumination variation during the experimentation days.

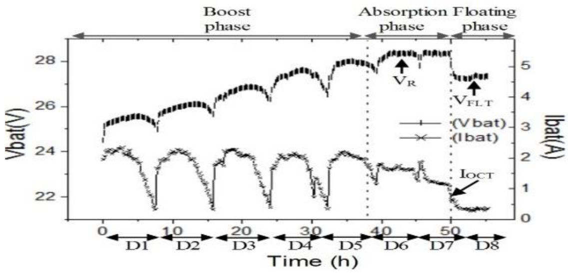

Fig .8 Variation of the charging VBAT and IBAT as a function of time.

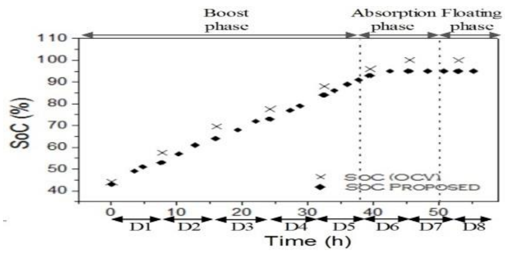

Fig .9 The variation of the state of charge SoC as a function of time.

2. Management of the batteries energy

To show the good functioning during the different control modes: charging cycle, discharging cycle and charging/discharging cycle. The PV system is experienced in order to manage the transfer of energy between panels and batteries and also between batteries and loads. The typical results are shown in Fig. 10. In this case, the charging current IBAT is approximately 4.5A and the initial battery voltage is VBAT=12.27V. While this installation is tested, the management and supervision system (MSS) performs the following operations:

- The initial state of charge estimation SoCi= 57%.
- During the charge cycle (between 0 and 3h), when the charge current is IBAT=4.5A and discharge current Idech=0A (Fig.10B), an increase of VBAT and SoC is observed (Fig.10A). While the SoC reaches 67%.
- During the discharge cycle (between 3 and 8h), when the current Idech=6.5A and IBAT=0A (Fig. 10B) a decrease of VBAT and SoC is observed (Fig. 10A) and when SoCmin.D reached SoC = 40%, the system stops the discharge to protect the batteries (Idech = 0A).
- During the charge/discharge cycle (between 8 and 11h), as long as the SoC is lower than a threshold of reconnection SoCmin.R = 45% (Fig. 10A), the discharge is blocked. Above this threshold and depending on the demand, a discharge can take place. When the discharge current is low (Idech=1A) between 9.5h and 10h (Fig. 10B), VBAT and SoC increase slowly since some of the power injected into the batteries is consumed by the load (Fig. 10A). When the discharge current is high (Idech=6A) between 10h and 11h, VBAT and SoC decrease, since the power injected in the batteries does not compensate this consumed by the load.
- All the results obtained in this section show the good control of energy transferred during charge cycle, discharge cycle and charge/discharge cycle of batteries depending on the use. This demonstrates the validation of the simulation results and therefore of the proposed charge/discharge technique of the PV system conceived (Fig. 5).

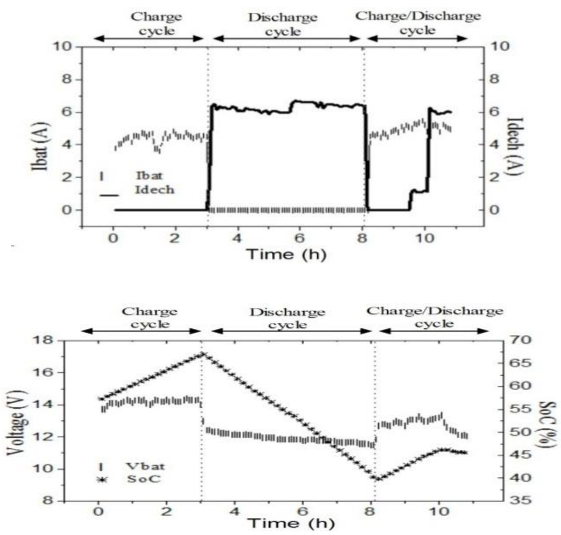

Fig .10 The evolution of electrical characteristics of the batteries during a charge cycle. (A): Variation of VBAT and SoC. (B): Variation of IBAT and Idech

3. Optimal functioning of the PV system

Concerning the optimal functioning of the PV system, where HILL CLIMBING improved algorithm is adopted (Fig. 4), the PWM signal that ensures the MPPT control, the search time to converge to the MPP and generated by the MSS and the electrical quantities (voltage, current and power) of PV panels and batteries during their charging/discharging process are extracted. From these results, the efficiency of the panels (□panel), DC/DC converter (□cnv) and global PV system (□sysPV) are inferred. Taking into consideration the same graphs, the results of optimal simulation obtained in Pspice under the same conditions are reported [12]. All the results obtained (Fig. 11 to Fig. 16) show that:

- There is a very good agreement between the results of optimal simulation and the experimental ones.
- The duty cycle of the PWM signal generated by the MSS system by using HILL CLIMBING improved algorithm, to ensure the MPPT control (Fig. 11) is practically the optimum one. The rapidity of the system convergence to the MPP is tested by experimentation and comparison of this algorithm to the classical presented in reference [11]. The results (Fig. 12) showed that the search time ratio of the classical (Tcla) and improved algorithms (Timp) clearly depends on the irradiance and the position of the functioning point of the PV panel. The improved algorithm is much faster and the search time can reach 50% compared to the search time using the classical algorithm.
- The electrical quantities (voltages, currents and powers) of the PV panels (Fig. 13) are practically the optimum ones, throughout all the batteries charging process. This shows that the MPPT controller has performed its role. It optimizes the functioning of the panels without divergence.
- The efficiency of the PV panels is around 9.5 % (Fig. 14). This shows, firstly, a good agreement between the type of PV panels used and their ageing and, secondly, low losses of the power supplied by the PV panels while the installation is working.
- During the first phase (Boost) of charging (0- 38h), the DC/DC converter efficiency (Fig. 15) is the efficiency of the battery charging since all the power supplied by the batteries is absorbed. This efficiency, which is about 85%, is very satisfactory and close to optimum.
- During the second and third phases of charging (38h - 55h), the efficiency while injecting into the grid increases and that of the batteries charge decreases (Fig. 15). This is so due to the decrease (increase) of the power absorbed (injected) by the batteries (grid).
- The global efficiency of the PV system during the charging and the injection into the grid (Fig. 16) is around 8.5%. It is very satisfactory and considered as the best percentage according to the literature [13-14].
- During the functioning of the PV system, the batteries are charged in three phases determined by the algorithm of Fig. 4 that take into consideration the parameters set (Thresholds charges MPPT control, power circuits ...). The different results obtained show the reliability of the system designed, in addition, the efficiencies presented in Fig. 14 to Fig. 16 guarantee the performance of the various blocks of the PV system: DC / DC converters, power system, etc.

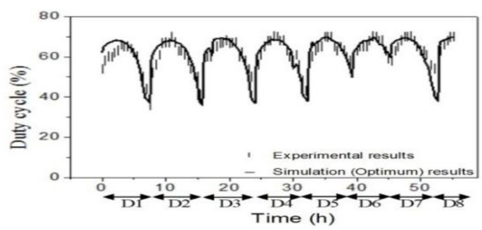

Fig .11 The evolution of the duty cycle as a function of time.

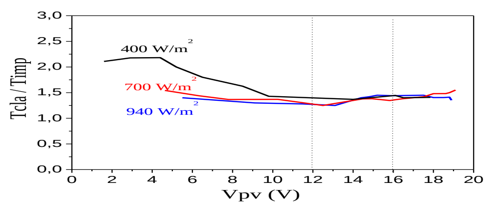

Fig .12 Relationship between the search times of the MPP in the presence of the classic and improved algorithms in function of the Vpv and the irradiance

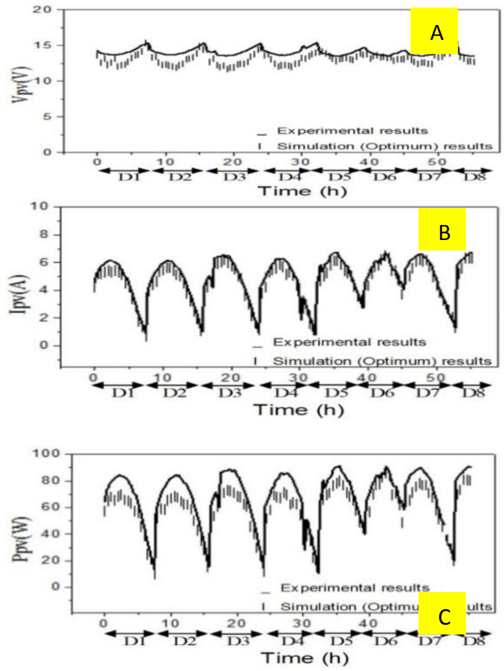

Fig .13 The evolution of: (A): experimental and simulated (Optimum) results of Vpv voltage (B): experimental and simulated (Optimum) results of Ipv current. (C): experimental and simulated (Optimum) results of Ppv power

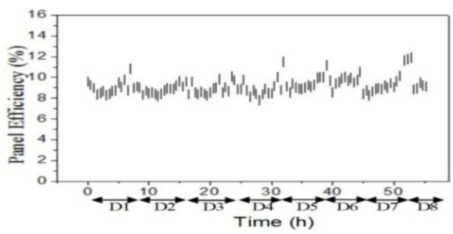

Fig .14 Efficiency of the PV Panels.

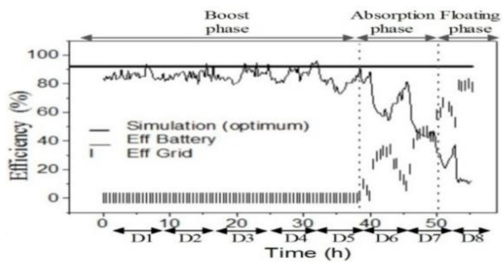

Fig .15 Efficiency of DC/DC converter (experimental and simulation (optimum) results) during the charging and the injection into the grid.

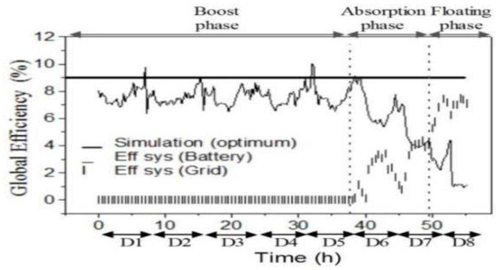

Fig .16 The global efficiency of PV system (experimental and simulation (optimum) results) during the charging and the injection into the grid.

IV. CONCLUSION

In this paper, the designed photovoltaic system is studied, which is equipped with a management and digital control system. The experimentation shows that the PV system works under optimal conditions and the search time of the MPP is significantly improved by 50% compared to the search time by using the classical algorithm. The PV system becomes fast and accurate. Also, the batteries are fully charged in three phases with a good estimation of the state of charge (around 5% of improvement as compared to the traditional method). During this operation, the control circuit of energetic flow allows to efficiently manage the energy supplied by the PV panels and to inject the surplus into the grid when the batteries are charged and even during the charging phases while the regulation is in order to minimize losses and for better use of energy. All this is accompanied by a good performance of the converter and the global PV system (85% and 8.5%).

The global results obtained in this work demonstrate the reliability and optimization of the PV system. Firstly, the digital card of the management and supervision system is configured according to the technical characteristics of this equipment (PV panels, batteries ...) and, secondly, he uses algorithms which are adaptable to all situations such as changes in illumination, loads and temperature.

V. ACKNOWLEDGEMENTS

This work is supported by:

- Belgian Development Agency CTB (Project MIP/012/010), Morocco.
- United Nations Development Programme UNDP Art Gold Morocco, ENV 2008 2 OO.
- Cooperation Moroccan-Belgian "Institutional University Commission", IUC, Oujda, 2008-2012 (Water and Environment Activity / Sub-Activity Renewable Energy).

REFERENCES

[1] Eftichios Koutroulis, and Frede Blaabjerg, “Design optimization of transformerless grid-Connected PV inverters including reliability,” IEEE TRANSACTIONS ON POWER ELECTRONICS, Vol. 28, no. 1, Jan 2013, p. 325.

[2] Rodolfo Dufo-López , Juan M. Lujano-Rojas, José L. Bernal-Agustín, “Comparison of different lead–acid battery lifetime prediction models for use in simulation of stand-alone photovoltaic systems,” Applied Energy, 115 (2014), pp. 242–253.

[3] Hongbin Wu, Shuzhao Wang1, Bo Zhao2 and Chengzhi Zhu2, “Energy management and control strategy of a grid-connected PV/battery system,” International Transactions on Electrical Energy Systems Article first published online: 18 April 2014, DOI: 10.1002/etep.1926.

[4] Mehdi Dali a, Jamel Belhadj, Xavier Roboam, “Hybrid solar-wind system with battery storage operating in grid–connected and standalone mode: Control and energy management experimental investigation, Energy, 35 (2010), pp. 2587-2595.

[5] Chang Yoon Chun a, Jongbok Baek a, Gab-Su Seo a, B.H. Cho a, *, Jonghoon Kim b, Il Kwon Chang c, Sangwoo Lee c, “Current sensor-less state-of-charge estimation algorithm for lithium-ion batteries utilizing filtered terminal voltage,” Journal of Power Sources, 273 (2015), pp. 255-263.

[6] Saeed Sepasi a,*, Reza Ghorbani a, Bor Yann Liaw b, “A novel on-board state-of-charge estimation method for aged Li-ion batteries based on model adaptive Extended Kalman filter,” Journal of Power Sources, 245 (2014), pp. 337-344.

[7] K. Hirech, M. Melhaoui, F. Yaden, E. Baghaz, K. Kassmi, “Design and realization of an autonomous system equipped with a regulator of charge/discharge and digital MPPT command,” The Mediterranean Green Energy Forum 2013, MGEF-13.

[8] M. Melhaoui, E. Baghaz, K. Hirech, F. Yaden, Khalil Kassmi, “Contribution to the improvement of the MPPT control functioning of photovoltaic systems,” International Review of Electrical Engineering (IREE), [S.l.], v. 9, n. 2, pp. 393-400, apr. 2014. ISSN 1827-6679.

[9] Kong-Soon Ng, Yao Feng Huang, Chin-Sien Moo, and Yao-Ching Hsieh, “An enhanced Coulomb counting method for estimating state-of-charge and state-of-health of lead-acid batteries,” IEEE Transaction. Published in Telecommunications Energy Conference, 2009. INTELEC 2009. 31st International.

[10] Hongxing Yang, Zhaohong Fang, Wei Zhou, “Battery behavior prediction and battery working states analysis of a hybrid solar-wind power generation system,” Renewable Energy 33, 2008, pp. 1413–1423.

[11] Baghaz, M. Melhaoui, F. Yaden, K. Hirech, K. Kassmi. “Design, realization and optimization of the photovoltaic systems equipped with analog and digital MPPT commands,” Energy Procedia, 42 (2013).

[12] Web-page : http://www.cadence.com, 2014.

[13] Jung Hun So, Young SeokJung, Gwon Jong Yu, Ju Yeop Choi, Jae Ho Choi, “Performance results and analysis of 3 kW grid-connected PV systems, Renewable Energy 32, 2007, pp. 1858–1872.

[14] Danny H.W. Li, K.L. Cheung, Tony N.T. Lam, Wilco W.H. Chan, “A study of grid-connected photovoltaic (PV) system in Hong Kong,” Applied Energy, 90, 2012, pp. 122–127. Contents lists available at Science Direct Applied Energy.

http://dx.doi.org/10.21622/RESD.2016.02.1.020

Conception and Realization of a PV System Provided with a Sun Tracker Operating at Dual Axis

R. GAAMOUCHE, A. LAMKADDEM, S. TALBI, K. KASSMI

* Mohamed Premier University, Faculty of Science, dept. of Physics, Laboratory LETSER (Team MEER), Oujda, Morocco.

E-mail: khkassmi@yahoo.fr

***Abstract* -** In this paper, The researchers present the conception, the realization and the experimentation of a photovoltaic (PV) system provided with a sun tracker reliable and low cost operating at dual axis. The tracker's role is to orient the PV generator, whose weight is about 9 Kg, perpendicular to the sun with very good accuracy. This tracking is based on the use of four LDR sensors, which detect the intensity of light scattered by a sun processing unit, from command and control (UTCC), which manages all of the sun tracking tasks (the end detection of parcours, regulation of the power supplied by the PV panels (Command MPPT), ...). The results obtained show a significant improvement of the energy produced, compared to conventional PV installations where generators are fixed and oriented south at a tilt 45°. During a day of operation, improvement could reach 41% and consumption of the tracking does not exceed 0.55% of the energy production produced by the PV generator (an improvement of 5 % compared to existing trackers).

***Keywords* -** Orientation of the photovoltaic generators, maximum power, tracker of the sun, microcontroller, LDR sensors, optimal collection of illumination, end detection of purposes parcours, MPPT command, consumption of energy, cost.

I. INTRODUCTION

The renewable photovoltaic energy (PV) is in the center of all attentions mainly because of its safety character to the environment [1]. This represents, certainly, a release track overlooked from the consumption mode of fossils energies. However, the conversion system to PV energy presents problems related to the yields of PV generators which do not pickup sufficient intensity of the solar radiation [2]. This is due to the positioning of the PV generators and to the type of system that ensures sunlight racking. In general, there is a multitude of methods and techniques that can be divided into two main categories [3]:

- The automatic tracking systems which use optical sensors to detect the position of the sun and then, initiate if necessary, motion of the tracker of the PV generator [4]. Their major disadvantage is additional losses of energy due to the consumption of the control system which remains activated permanently [5].

- The automatisms to calculate forecasts of the sun path in order to start or not the tracking system, by comparison with the real trajectory. This is called then programmed trackers (regulated) or astronomical pursuit [6]. In this type of technique, the tracking depends on the zone in which the system will be located.

- Currently, the sun tracking systems proposed in the literature have the disadvantages [7]: complicated regulation [8], complex structure [9], mechanical stability problems, consumption when tracking the sun (greater than 8 Wh/day, for a panel of 100 WCrete) and high cost [10].

In order to enhance reliability of the structure, the functioning, the consumption and the cost of the sun tracker, the researchers propose in this paper the conception of a sun tracker system operating at dual axis two axes having the technical characteristics:

- Moving a PV generator of 200 W Crete and a weight of the order of 5.4 kg,

- the operative part is molting thanks to two motors,

- collecting the irradiance intensity by using four sensors LDR [11],

- the command part uses a processing unit, command and control (UTCC), programmed for the piloting of the actuators in order to track with precision the trajectory of the sun depending on the illumination image voltages from LDR sensors, and voltage from the specific circuitry to automatically detect from purposes parcours (sunrise and sunset, ...).

The researchers first present the structure and the functioning of each bloc of PV system provided with the sun tracker. Then, they analyze the experimental results concerning the functioning of the complete system during a the whole day. An attention will be particularly given to production and losses of energy in each bloc of the system: PV generators, DC/DC converter, tracker,…

II. CONCEPTION AND FUNCTIONING OF THE PV SYSTEM PROVIDED WITH A SUN TRACKER

A. Structure of the PV system

The bloc diagram of the PV system provided with a sun tracker operating at dual axis is presented on figure 1. This system is conceived to track the maximum intensity of the diffuse light by the sun during the whole day. It has the following blocs:

- Four LDR sensors (C1, C2, C3 and C4) positioned in four locations of the PV panel. They provide voltages depending on the intensity of illumination [9]. The displacement of the PV panel depends strongly on these voltages.
- A PV generator [12] which provides a power of 180 W, under a voltage of 35.8V and a current of 5 A.
- A DC/DC converter “Boost” [13] (figure 2). The components of the converter (Inductance L, capacities CE and CS) are dimensioned so that this one operates at a quench frequency of 10 kHz and a power which could reach 500 W.
- A digital MPPT command [13] which allows searching the maximum power point (MPP) of the PV panel [14,15] independently of meteorological conditions (irradiance, temperature) and the load.
- A resistive load.
- A sun tracker composed by:

• a mechanical system that tracks the position of the sun automatically, by varying two angles of the support of the PV panels following a horizontal rotation (East and West) and a vertical rotation (North and South)[16]. This mechanical system is ordered by an electronic board based on a microcontroller through two actuators: the first one acts on the horizontal axis and the second on the vertical axis.

• The actuators used are two electric jacks based on engine with continuous current with a magnet permanent with a reducer (supporting voltages of 36 V, current 4.8 A) [17]. The electric jacks used transform the rotational movement created by an electric motor in translator movement using a metal stem. The displacement of this stem varies linearly with the rotation speed of the engine and the system of transformation of movement. The choice of this type of jacks is justified by its availability on the market, its moderate cost, and its ease of use, besides it does not require other articulations during usage .

• a processing unit, command and control (UTCC) which represents the heart of the movements management of the PV generators used and the regulation of the power supplied by these (MPPT command). This bloc (UTCC) is based on the use of a microcontroller provided with an oscillator with quartz of frequency 20 MHz and a circuit of power which plays the role of an interface to realize all the spots: speed of both engines, direction of displacement and end detection of parcours (the West and the East).

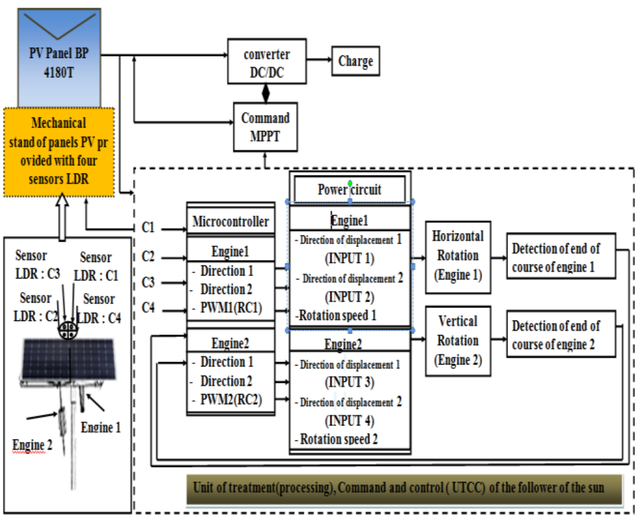

Fig .1. Schematic diagram of the solar system with the sun tracking.

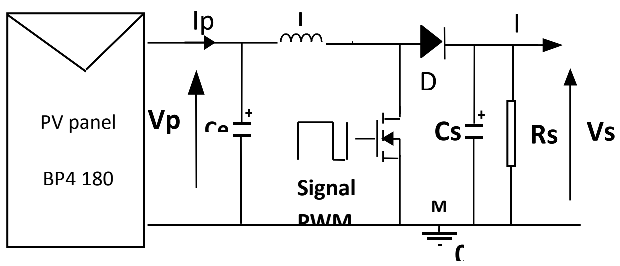

Fig .2. Structure of DC-DC converter "Boost".

B. Functioning of the sun tracking system

The functioning of the tracker at dual axis (Figure1), conceived and realized during this work, is based on the acquisition and the analysis of the voltages of the LDR sensors. This voltage decreases with the increase of the irradiance intensity received by the LDR sensors. The orientation of panels is made according to the information received and sent by the microcontroller of the UTCC unity in the following way:

- The microcontroller receives and exploits the imbalance created between four LDR sensors through the analog pines of the microcontroller.
- The microcontroller receives voltages from the specific circuits, realized during this work, to detect purposes of the parcours through the analog pines of the microcontroller.
- The rotation speed of engines is fixed by a signal PWM, sent by the microcontroller, of frequency 1500 Hz and of duty cycle 0,75.
- The direction of displacement of motor movement is set by the power circuit [18] (H-bridge) based on the states of these inputs (INPUT 1, INPUT 2, INPUT 3 and INPUT 4). In table 1, the researchers have summarized the various situations which can take place (sens1, sens2 and stop).

The whole of tracking the sun tasks is realized by the microcontroller according to the algorithm of continuation represented in figure 3:

- Configuration of input and output pines of the PIC,
- Reading of the various voltages (V1, V2, V3 and V4)
- which are proportional to illuminations of four LDR sensors ,
- Comparison of the voltages V1, V2, V3 and V4, converted by the PIC.
- Activation of the two pines RC1 and RC2 of the PIC to generate two PWM signals of frequencies 1500 Hz and of cyclical reports adequate to secure the speed of rotation of the two motors.
- Generation of the pulses (5 V or 0 V) on the pines of the power module (Input 1 to 4) when the PIC detects an imbalance in the sensors voltage .
- Fixing the direction of the currents in the engines, following table 2, so that the PV panel picks up the maximum of the illumination power.
- Displacements of the engines with the possibility of detection of the ends of course.

Table 1. DIFFERENTES SEQUENCES DU SENS DE DEPLACEMENT DES MOTEURS 1 ET 2.

Input 1	Input 2	State motor 1	Input 3	Input 4	State motor 2
0	0	Stop Motor	0	0	Stop Motor
0	1	Direction 1 (EAST towards the WEST)	*0*	1	direction 1 (SOUTH towards the NORTH)
1	0	Direction 2 (WEST towards the EAST)	*1*	0	Direction 2 (NORTH towards the SOUTH)
1	1	Stop Motor	*1*	1	Stop Motor

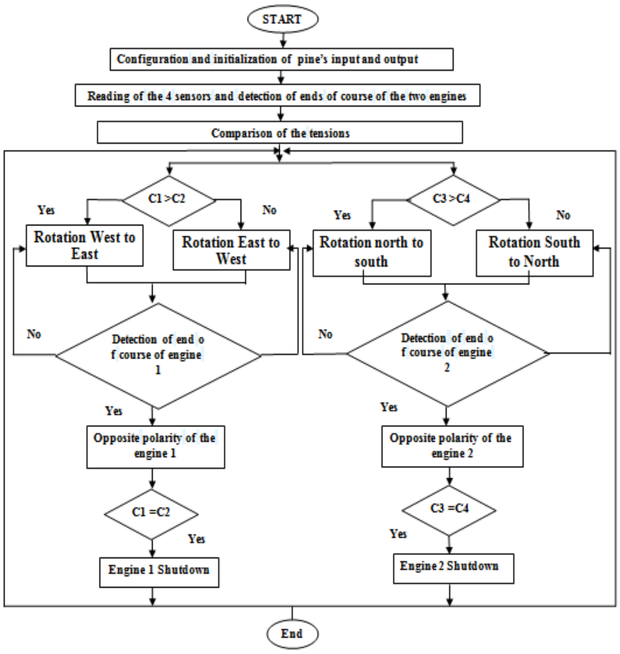

Fig .3. Algorithm of a tracker of the sun in two axes.

III. EXPERIMENTAL RESULTS

A. Experimental procedure

Figure 4 represents the bench electrical measurement automated and the PV system, fitted with the tracker, conceived and made in the researchers' laboratory during this study . The bench and the system are composed by:

- Equipment of measures connected to computer: multimeter (Keithley 2700), digital oscilloscope…
- PV Panel (180 Wcrete) in monocrystalline silicon is provided by a pyranometer with Meteon which measures the value of illumination directly.
- Tracker of the sun whose role is to position the panel perpendicular to the sun in order to collect the maximum of the sun. It is formed by a mechanical support provided with two engines, in order to direct panel PV along two axes, and of a control unit (UTCC).
- An energy DC-DC converter type 'Boost' fitted with a MPPT command which follows the maximum power point (PPM) of the PV panel.
- A resistive charge of value 50 Ω

Fig .4. Bench of automated measurements, prototype photovoltaic (panels, tracker of the sun, Converter Boost MPPT command).

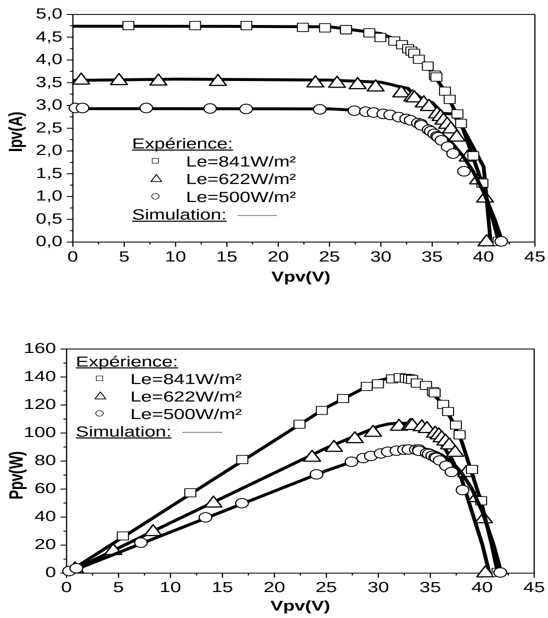

Fig .5 Experimental and simulated Current-Voltage and Power-Voltage characteristics

B. Electrical characteristics of photovoltaic panels

The researchers have characterized the PV panel used for a whole day where the intensity of irradiance varies between 400 W/m to 900 W/m² and the temperature 26 °C - 30 °C. In Figure 5, the researchers present the typical characteristics of the current-voltage and the power voltage obtained. On the same figures, they present the simulated characteristics in Pspice by setting the parameters of the diode (saturation current, ideality factor, ...), which allow them to obtain the experimental results. The results show good agreement between experiment and simulation throughout the range of the intensity of the illumination.

In the validation part of the operation of the tracker, the researchers use the parameters fixed in the simulations.

C. Functioning of the LDR sensors

Furthermore, the researchers have tested the operation of the LDR sensors during a day when the intensity of irradiance reached 1000 W/m2. In figure 6, the researchers represent the typical evolution of the voltage at the terminals of the sensors with the intensity of the illumination. In the same figure 5, they have deferred the results of simulation got in ISIS Proteus [19]. These results show on the one hand a very good agreement between the experiment and the simulation, and on the other, that when illumination varies from 200 W/m2 to 1000W/m2, the voltage at the terminals of the LDR varies from 300 mV to 60 mV (decrease of the voltage of 20 % when the illumination increases of 200 W/m2).

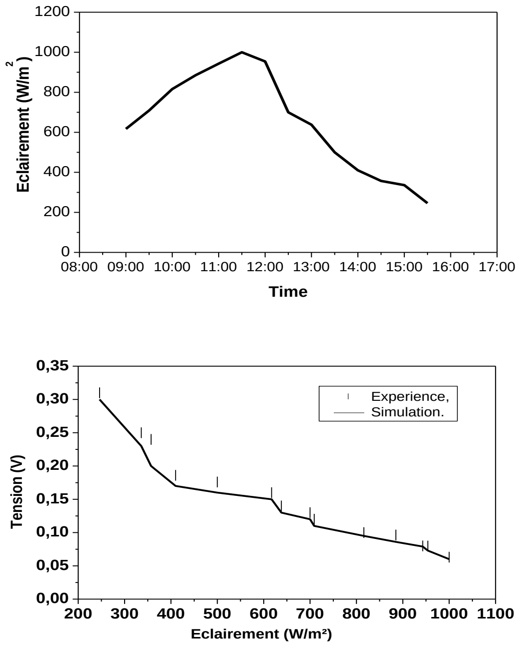

Fig .6 Variation of the irradiance and the voltage in function of the illumination during a day.

D. Functioning of the tracker

The typical function of the tracker bloc is presented in figures 7 to 11, when the maximum intensity of illumination on sensors C1 and C2 is detected. The same function is obtained on the C3 and C4 sensors. The results show:

- The PIC detects the imbalance between sensors C1 and C2 (Figure 7) and generates PWM signals of amplitude 4 V, frequency 1500 Hz and duty cycle α = 0.75 (Figure 8). Under these signals, engine 1 rotates with a very satisfactory speed and a 0.19A current (Figure 9) to achieve the equilibrium position of the LDR sensor and hence the maximum illumination intensity.

- C1 sensor senses high intensity light from sensor 2 (V1 <V2) (Figure 7), the control system of the tracker supplies motor 1 with activating Input1 = 1, Input2 = 0 of the power circuit (Figure 10). The PV panel moves from west to east under motor1 0.19A current (Figure 9). Since the panel is close to the optimal position, the light intensities received by the LDR C1 and C2 increase and the two voltages V1 and V2 decrease (Figure 7). When these two LDR sensors receive almost the same intensities (V2»V1) (Figure 7), the tracker control system detects the optimal position of the lighting, following the direction WEST / EAST and generates a zero current (Input 1 = Input 2 = 0) to stop the engine displacement 1 (Figures 9 and 11).

All the results obtained in this paragraph show the good functioning of the circuits and blocs of the tracker, conceived and realized in this work: good detection of the light intensity and displacement the PV panel to the optimal position illumination.

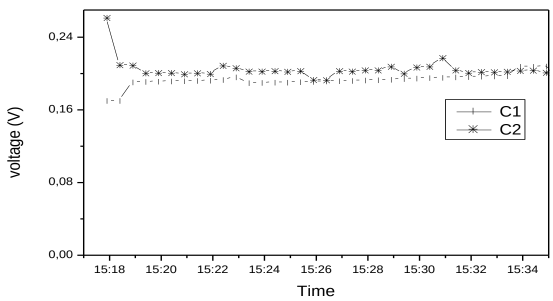

Fig .7 Variation of the voltage LDR C1 and C2 sensors.

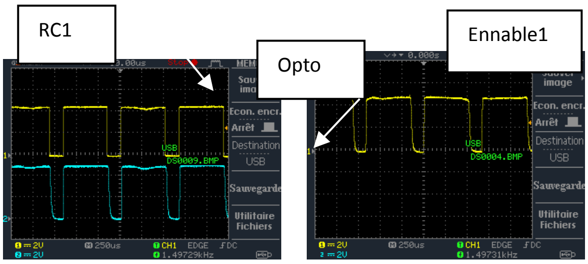

Fig .8 PWM1 signal at the outputs of the PIC (Pin: RC1) of the Optocoupleur, and at the input (Ennable1) of the power circuit (scales: 2 V / Div, 25 microseconds / Div).

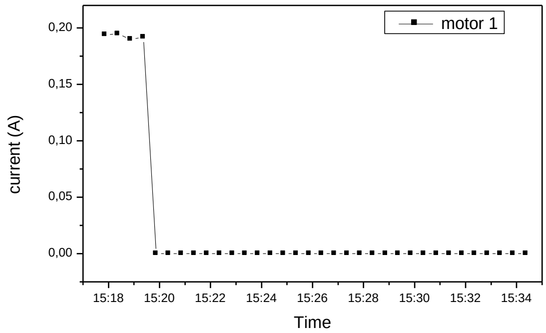

Fig .9 Supply current of motor 1 during the equilibrium of the LDR C1 and C2 sensors.

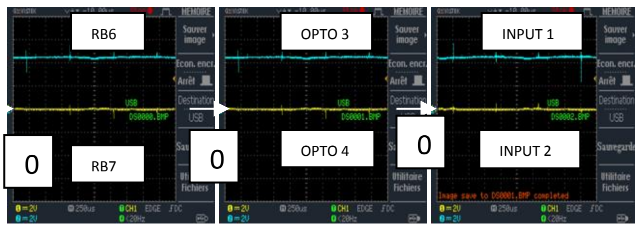

Fig .10 States of the Pins RB6 et RB7 of PIC ,the outputs of the Optocoupleurs and the input of the power circuit upon the rotation of the during the rotation of the motor the WEST to the EAST (scale: 2 V / Div, 25 microseconds / Div).

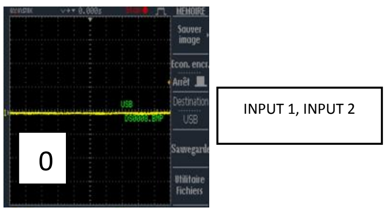

Fig.11. States of INPUT 1 and 2 of the power circuit during detection of the equilibrium LDR C1 and C2 sensors following a displacement of the WEST to the EAST (scale: 2 V / Div, 25 microseconds / Div).

E. *Functioning of the DC / DC converter*

In Figure 11, the researchers present the typical wave forms of the PWM signals generated by the MPPT control, the terminals of the inductor, the diode and the output of the power switch. These results show:

- The MPPT command generates a signal of frequency 10 kHz and a duty cycle of 0.63. The comparison of this value and the optimal [12] shows that the converter is controlled under the optimum conditions and the PV panel runs around the PPM [13-20].

- When the switch is closed:

The output voltage of each switch is :(Vds =0V),

The voltage across the inductance is:

$$VL1 = Vpv1 = 36.3V$$

The diode is blocked and its voltage is equal to:

$$Vs = -74V \text{ (fig. 12.D)}$$

When the switch is opened :

The output voltage of the switch is equal to the output because the diode conducts (fig 12.B) :

$$Vds = Vs = 74V,$$

The potential difference to the terminal of the inductor is (fig 12.C) :

$$VL = Vpv - Vs = -37.7\ V$$

All the results obtained in this section show the good functioning of each active component and liabilities of the DC/DC converter in optimal conditions.

http://dx.doi.org/10.21622/RESD.2016.02.1.020

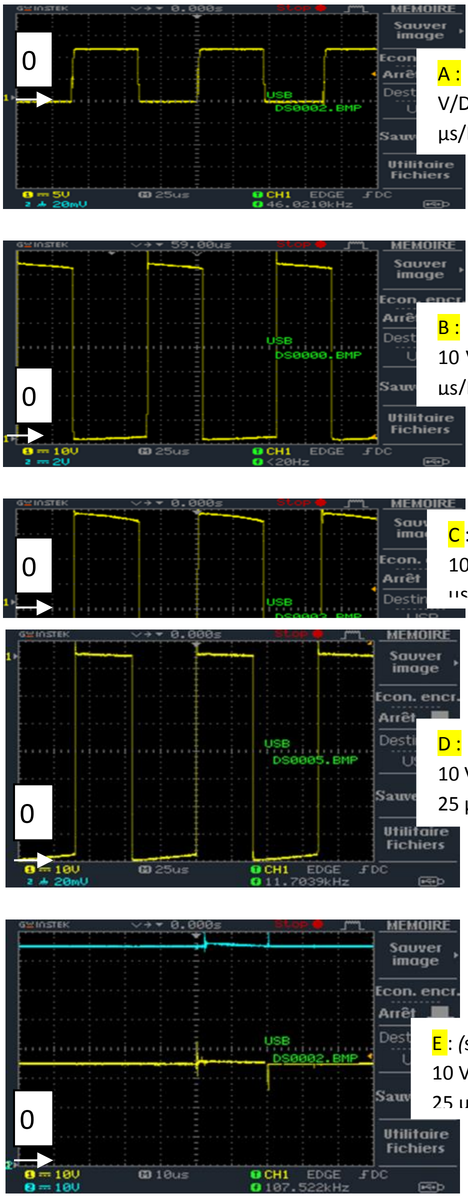

A : (scale: 2 V/Div, 25 µs/Div).

B : (scale: 10 V/Div, 25 µs/Div).

C : (scale: 10 V/Div, 25 µs/Div)

D : (scale: 10 V/Div, 25 µs/Div).

E : (scale: 10 V/Div, 25 µs/Div).

Fig.12. - Wave form:
A : PWM generated by the MPPT control.
B : The output voltage of the power switch.
C : Voltage across the inductor.
D : Voltage across the diode.
E : Voltage at the input (Vpv) and to the output of the DC-DC.

F. Functioning of the DC / DC converter

The researchers have analyzed the functioning of the PV system provided with the sun tracker (Figure 4) during a whole day of operation. In order to validate the obtained results, they have carried out a comparative study compared to the classic installation by experimenting the same PV system when the panel PV is fixed and oriented southward of an inclination of 45 °.

In Figure 13, they show the results obtained: irradiance, duty cycle of the command MPPT, the electric greatnesses (voltage, current and power) at the input and output of the DC/DC converter and the efficiencies of the DC/DC converter and the complete system. In the same figures 13.B to D, they represent the optimal simulation results. From the obtained results, they have deducted the energy produced by the panel PV, in the case of both installations (system PV with and without tracker) so there is a loss of energy in the case of the classic installation. All results show:

- A very good agreement between experiment and the simulation.
- The electric greatnesses are improved remarkably with the tracker. The energy produced by the PV panel on the order of 820.47 Wh (628.46Wh) in the presence (absence) of the tracker (an improvement of 23.4%). Power losses are very important and can reach 8% (with tracker) (41% - without tracker) at noon (beginning and end of the day).
- The efficiencies of the converter (superior to 90 %) and the global system (of the order of 13.87 %) are very satisfactory. They are considered among the best in the literature.
- The energy consumed by the tracking system of the sun for a whole day of operation does not exceed 4.55 Wh, This value is significantly better compared to that of the literature which is 6 to 9 Wh [21].

All the obtained results show the good functioning and very interesting performances of the PV system provided with the tracker conceived and realized during this work.

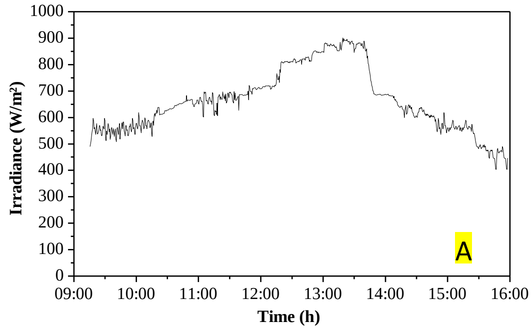

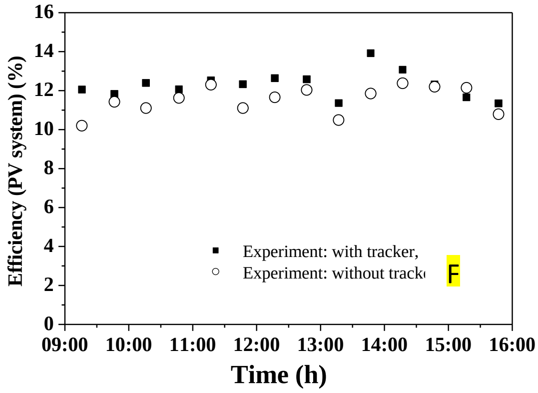

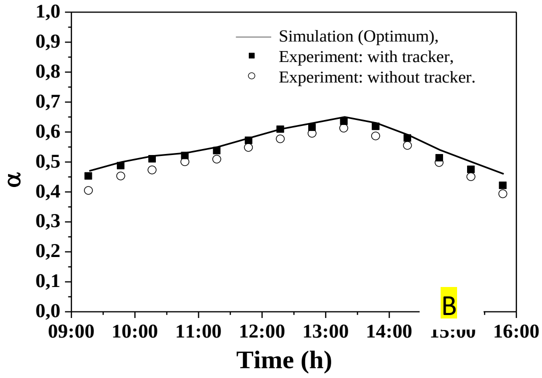

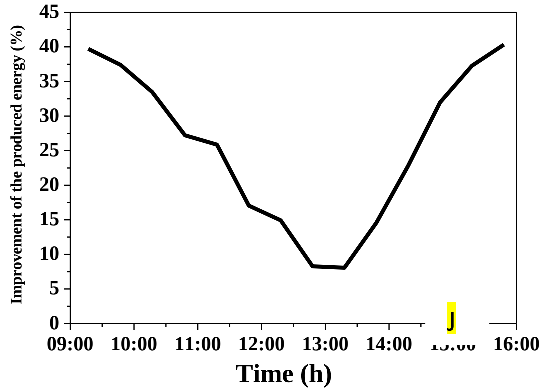

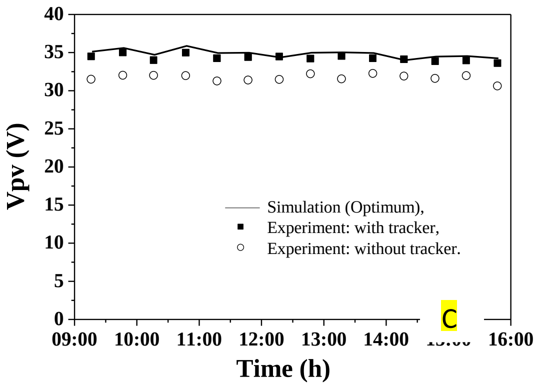

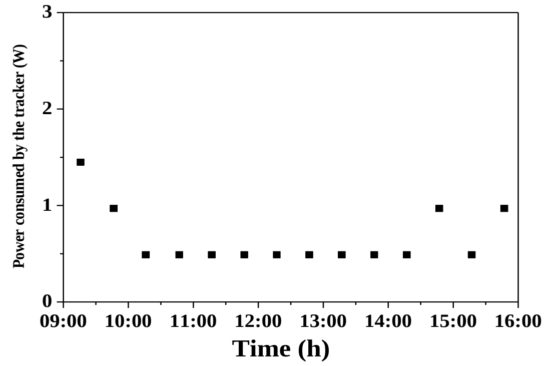

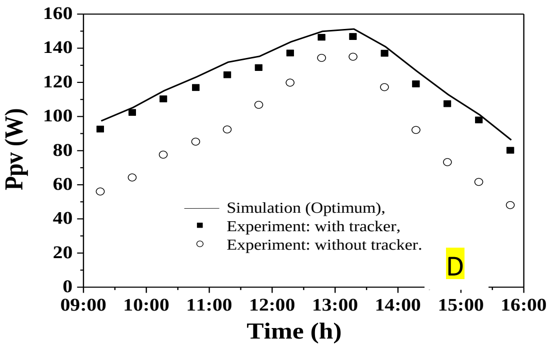

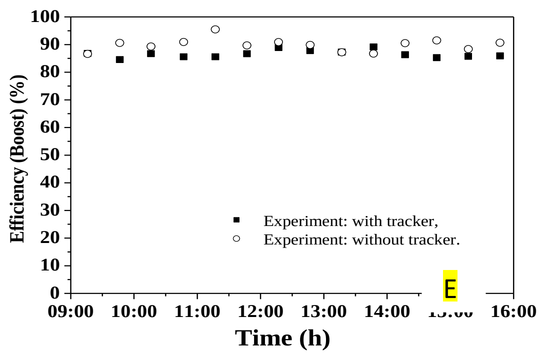

Fig.13. Electrical quantities, experimental and simulated (Optimal) a PV system with a follower system of the sun and a PV system facing south with a 45 ° inc H
- Variation of the irradiance (A),Variation of uty cycle (B).,
- the voltage Vpv (C) , the power Ppv (D) .
- Power losses to the level of the DC-DC converter (E).
- The efficiency of the global system (F).
- The losses of a PV system with a tracking system of the sun relative to a fixed system (J).
- Consumption of a tracker system of the sun (H).

IV. CONCLUSION

The PV system provided with a sun tracker operating at dual axis, conceived and realized in this work, shows on the one hand the good functioning of the tracker and on the other , the very satisfactory performances. By comparing with the PV systems provided with the classic trackers or fixed PV generators, the researchers have shown improvements of the produced energy which could reach 41%, weak consumption of the tracker (< 0.55% of the product energy, either improvement of 5% with respect to currents trackers) and very interesting costs.

In perspective, the tracker conceived in this work will be used in PV installations (2-3 kW) realized in the isolated site of Douar Zragta, Rural District of Oujda-Angad Prefecture (Pumping and lighting). These installations are carried out by the concerned research team with support from United Nations Projects Art Gold Morocco and Belgian Development Agency in Morocco CTB (Project MIP 10/12).

V. ACKNOWLEDGEMENTS

This work is realized in the frame:

- Belgian Development Agency BTC (Project MIP/012/010).
- PNUD Art Gold Marocco Program, 2008 2 ENV OO.
- Cooperation Morocco-Belgian "Institutional University Commission" IUC-Oujda 2008-2012 (Water and Environment Activity/Sub-Activity Renewable Energy).
- Moroccan-Tunisian Cooperation SCIENTIFIC RESEARCHAND TECHNOLOGY project (11/MT/38).

REFERENCES

[1] B. Pandey1, A. Agrawal2"Automatic sun tracking system using PSoC", International Journal of Innovative Research in Science, Engineering and Technology, Vol. 1, Issue 1, November 2012.

[2] A. Ponniran, A. Hashim, A. Joret "A design of low power single axis solar tracking system regardless of motor speed ", International Journal of Integrated Engineering, Vol. 3 No. 3 (2011) .

[3] B. S. K. Ray, M. Abul Bashar, A.Maruf,F. Bin Sayed "Two

[4] ways of rotating freedom solar tracker by using ADC of microcontroller " ,Global Journal of Researches in Engineering, Vol. 12 Issue 4 Version 1.0, 2012,ISSN: 0975-5861

[5] J. Axaopoulos, P. Emmanouil .M. Fylladitakis, "Energy and economic comparative study of a tracking vs a fixed photovoltaic system", European Scientific Journal April 2013 edition vol.9, No.12 ISSN: 1857 – 7881 (Print) e – ISSN, pp. 1857- 7431.

[6] H. Mousazadeh, A. Keyhani , A. Javadi , H. Mobli ,K. Abrinia , A. Sharifi, "A review of principle and sun-tracking methods for maximizing solar systems output," Renewable and Sustainable Energy Reviews, vol. 13, January 2009, pp. 1800–1818.

[7] L .Alboteanu, G. Manolea, F. Ravigan, "Positioning systems for solar panels placed in isolated areas," Annals of the University of Craiova, Electrical Engineering.

[8] O. Bingol, A. Altintas, Y. Öner, "Microcontroller based solar-tracking system and its implementation," Journal of Engineering Sciences , 12, 2, 2006, pp. 243-248

[9] M. Rebhi, M. Sellam, A. Belghachi, B. Kadri, " Conception and realization of sun tracking system in the south-west of Algeria, " Applied Physics Research ISSN: 1916-9639 Vol. 2, No. 1, May 2010. pp. 66-75

[10] S. Zubair, A. Suleiman, H. T. Abdulazzez, B. A. Salihu, "Design and construction of a microcontroller based single axis solar tracker, " al / Innovations in Science and Engineering 1 (2011).

[11] http://www.solarkit.com/epages/62035995.sf/fr_BE/?ObjectPath=/Shops/62035995/Categories/-traceur-solaire-suntracer-

[12] Bhavesh Pandey, Anita Agrawal, "Automatic sun tracking system using PSoC, " International Journal of Innovative Research in Science, Engineering and Technology, Vol. 1, Issue 1, , pp. November 2012, pp. 66-70.

[13] Kais I. Abdul-lateef, “A low cost sin gle-axis sun tracker system using pic microcontroller,” Diyala Journal of Engineering Sciences Vol. 05, No. 01, June 2012, pp.65-78,.

[14] http://greenforcesolar.com.au/wordpress/wpcontent/uploads/2011/04/BP_4180T_solar_panel.pdf .

[15] M. El Ouariachi, T. Mrabti, Ka. Kassmi and K. Kassmi, “Regulation of the electric power provided by the panels of the photovoltaic System,” International Journal of Physical Sciences, Vol. 4, No5, May 2009, pp. 294 – 309,.

[16] M. Melhaoui, E. Baghaz, K. Hirech, M. F. Yaden and K. Kassmi, “ Contribution to the improvement of the MPPT control functioning of Photovoltaic systems,” International Review of Electrical Engineering (I.R.E.E.), v. 9, n. 2, pp. 393-400, apr. 2014. ISSN 1827-6679.

[17] F.Pinhelli,G. C. Neto, S. L.Stevan, “ Automation For solar tracker for panel photovoltaique – efficiency analysis”, Iberoamerican Journal of Applied Computing, Vol. 2, No. 2, Aug.2012, ISSN pp. 2237-4523

[18] S. Zubair, A. Suleiman, H. T. Abdulazzez, B. A. Salihu, “Design and construction of a microcontroller based single axis solar tracker, ” al / Innovations in Science and Engineering 1 (2011).

[19] M. F. Yaden, M. Melhaoui, R. Gaamouche, K. Hirech, E. Baghaz, K. Kassmi, “Photovoltaic system equipped with digital command control and acquisition,” Electronics.; 2(3) 2013, pp. 192-211.

[20] P. S. Pandiarajan, C. Mukuntharaj, “Effective power generation system for day and night using solar power with tracking a molten salt techniques,” International Journal of Engineering Research &Technology (IJERT), Vol. 1 Issue 6, August – 2012, ISSN: pp. 2278-0181 .

[21] N. W. Gosim, T. Faisal, H. Al-Assadi, and M. Iwan, “Pick and place ABB working with a liner follower robot,” Procedia Engineering 41 2012), p. 1336.

[22] http://www.labcenter.com/index.cfm

[23] A. Salsabila ,S. Suhaidi ,Z.A.A.K Mohd , “Power feasibility of a low power consumption solar tracker,” Procedia Environmental Sciences, 17 (2013),pp. 494 – 502.

http://dx.doi.org/10.21622/RESD.2016.02.1.030

Soil Inertia and Shallow Basement Envelope Impact on Cellar Internal Temperature

Naima Sakami[1], Lahcen Boukhattem[1], Hassan Hamdi[2]
[1] EnR2E, CNEREE, Cady Ayyad University, Marrakech, Morocco
[2] LMFE URAC27-CNRST, FS, Cady Ayyad University, Marrakech, Morocco
sakami.na3@gmail.com

Abstract - This study deals with a three dimensional numerical study of heat transfer by conduction between the soil and the shallow basement in the city of Marrakech (Morocco). The heat transfer equation is solved by the finite difference method using the implicit alternative direction (ADI). The internal temperature of the cellar is computed by using energy balance equation in the cellar. The objective of the study is to evaluate the effects of the nature of the soil, the nature of the walls, the thickness of the walls of the cellar, the distance L far from the cellar on the internal temperature, and the heat exchanged between the soil and the shallow basement.

Keywords - ADI Scheme; Internal temperature; Nature of soil; Basement; Heat flow.

Nomenclature -

L	Distance delimiting the disrupted area along x axis, m
D	Distance delimiting the disrupted area along y axis, m
H	Depth of the water table, m
E	Thickness, m
T	temperature, °C
Cp	Specific heat, J kg^{-1} K^{-1}
ρ	Density, kg/m^3
λ	Thermal conductivity , W/mK
dS	Internal elementary surface of the wall, m^2
t	Time, s
h_c	The overall exchange coefficient, Wm^{-2}K^{-1}
V	Volume of shallow basement, m^3
α	Thermal diffusivity , m^2/s
q	Mass flow rate of fresh air, kg/s

SUBSCRIPTS –

a	Air
amb	Ambient
m	Wall
p	Floor
s	Soil
w	Water table
wall	Wall surface
int	Inside shallow basement

I. INTRODUCTION

The interest of the study of the heat transfer in the basement is to show the importance of the soil inertia in the hot regions such as Marrakech. Owing to the very high thermal capacity of the soil, the temperature of the ground is lower than that of the outdoor air in the summer and higher in the winter. Consequently, the heating and cooling energy of a building considerably sunk into ground is lower than that one above the ground.

Thus, accurate estimation of loads and energy consumption due to thermal interactions between a building and the ground is needed. This is a difficult task since this analysis needs to include the multi-dimensional nature of most earth-coupled heat transfer processes, large phase lags caused by soil thermal mass, limited practical ability to model soil thermal proprieties and the variability of soil temperature with ground surface conditions [1]. It is difficult to derive analytical solutions for 3D transient ground-coupled heat transfer even for the simple rectangular slab-on-ground problem. The only available 3D analytical expression is the steady-state solution derived by Delsante et al. [2] for a rectangular slab-on-ground with the assumption of a linear temperature distribution along the base (wall/ground interface) of the external walls. A semi-analytical method inter-zones temperature profile estimation (ITPE) has been developed by Krarti et al. [3]. It combines analytical solutions for regular-shaped components and numerical techniques to connect these components to construct the ground model. The ITPE method is used to calculate the approximate analytical solutions for the three-dimension heat transfer between slab-on-grade floors and rectangular basements under steady-periodic conditions. W.R. Bahnfleth developed a detailed three-dimensional finite difference model for heat conduction from slab-on-grade floors and basements, including a detailed ground surface energy balance. [4]. M. P. Deru [5] used the two dimensional finite element to study the effects of moisture on the heat transfer from two basic types of building foundations, a slab-on-grade and a basement. A two-dimensional finite element heat and moisture transfer program is used to show the effects of precipitation, soil type, foundation insulation, water table depth, and freezing on the heat transfer from the building foundation. Recently M. Staniec and H. Nowak [6] determined the earth sheltered building's heating and air-conditioning energy demand depending on the type of soil in which it is founded. For comparison, the corresponding results for the above ground building are presented.

In Marrakech, several studies have been made to analyze the heat exchange between the ground and a building. A. Abdelbaki generated a two-dimensional transfer function coefficients (TFC) for a slab-on-grade floor [7]. Later, TFC have been derived successfully for shallow basement [8, 9] and earth-sheltered building [10]. It has been shown [7, 9] that the results obtained using the transfer functions method fully agree with those obtained using the ITPE technique and the ADI technique. Recently L. Boukhattem [11, 12] used the ADI method to study the effects of the parameters of mortar on the heat exchange between the soil and the two buildings: buried building and semi-buried building.

In this work, the researchers have developed a computer code that allows them to study the effect of the nature of the soil, the nature of the walls of the underground building, the thickness of the walls, the distance L of the disrupted area on the internal temperature, and the heat exchanged between the soil and the shallow basement.

II. MATHEMATICAL FORMULATIONS AND BOUNDARY CONDITIONS

A. Configuration of the studied Shallow basement

The configuration treated in this work is illustrated in Figure 1. The basement has a rectangular shape with a width of 2b, a length of 2a and a depth of c. The wall and the floor are assumed to have identical thermal conductivity and thermal diffusivity.

The results presented in this section are obtained for: a=2 m; b=2 m; c=2 m and e_m =0.26 m

The overall heat transfer coefficient [3, 8, 11] is: h_c=8.30 $Wm^{-2}K^{-1}$.

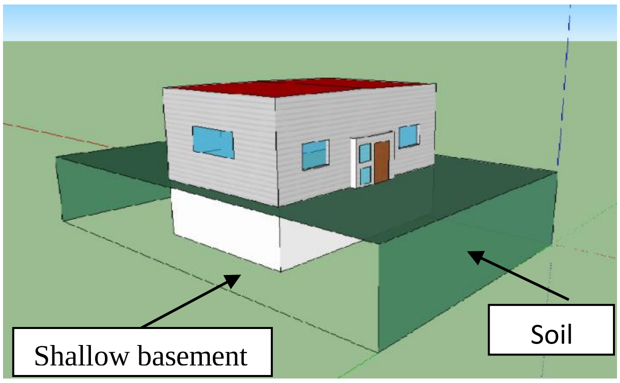

Fig .1. Building with a shallow basement

Because of the symmetry of the studied configuration, the study is reduced to a quarter of the shallow basement (Figure 2)

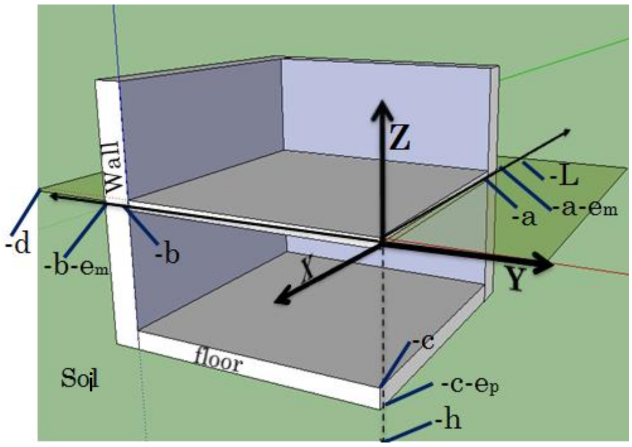

Fig .2. Shallow basement configuration

B. Mathematical model

The unsteady three-dimensional heat transfer equation can be written as follows:

$$\rho C_P \frac{\partial T}{\partial t} = \lambda \left(\frac{\partial^2 T}{\partial x^2} + \frac{\partial^2 T}{\partial y^2} + \frac{\partial^2 T}{\partial z^2} \right) \quad (1)$$

This equation was solved by an improved alternating-direction-implicit (ADI) finite-difference numerical method. A FORTRAN program was built for this analysis.

http://dx.doi.org/10.21622/RESD.2016.02.1.030

Minimum cell dimensions were established in accordance with the accuracy and stability criteria set forth by the numerical method employed in the study. Grid spacing in the present model in the vicinity of the building foundation ranged from 0.2 m to 0.3 m, while spacing at far-field and deep-ground boundaries was as large as 1.3 m.

C. Real climate of Marrakech

The simulation by the ADI method is made by considering the real ambient temperature of Marrakech. This temperature was measured by the weather station of AGDAL Marrakech. Figure 3 shows the variation of medium ambient temperature during one year (2008).
The water table at a depth of 13 m below the soil surface is maintained constant at 20 °C.

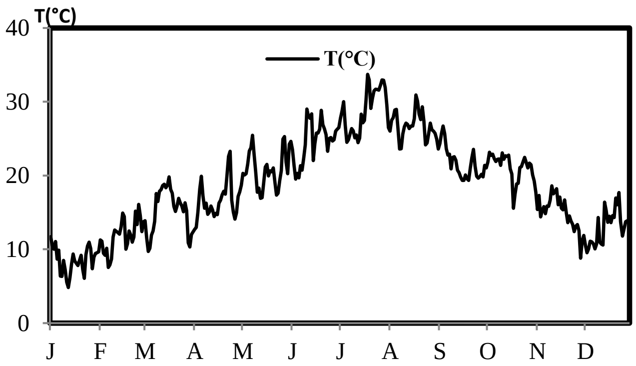

Fig .3. External air temperature

The Boundary conditions of the studied problem are:

- In the two planes of symmetry:

$$\left.\frac{\partial T_{\text{int}}}{\partial x}(x,y,z,t)\right|_{x=0}=0 \tag{2}$$

For $-d \le y \le 0$ and $-h \le z \le 0$

$$\left.\frac{\partial T_{\text{int}}}{\partial x}(x,y,z,t)\right|_{y=0}=0 \tag{3}$$

For $-L \le x \le 0$ and $-h \le z \le 0$

- Far from building:

$$\left.\frac{\partial T_s}{\partial x}(x,y,z,t)\right|_{x=-L}=0 \tag{4}$$

For $-d \le y \le 0$ and $-h \le z \le 0$

$$\left.\frac{\partial T_s}{\partial y}(x,y,z,t)\right|_{y=-d}=0 \tag{5}$$

For $-L \le x \le 0$ and $-h \le z \le 0$

- Interfaces internal air-side of the building :

$$-\lambda_s\left.\frac{\partial T_s}{\partial x}(x,y,z,t)\right|_{x=-a}=h_c(T_s(-a,y,z,t)-T_{\text{int}}) \tag{6}$$

For $-b \le y \le 0$ and $-c \le z \le 0$

$$-\lambda_s\left.\frac{\partial T_s}{\partial y}(x,y,z,t)\right|_{y=-b}=h_c(T_s(x,-b,z,t)-T_{\text{int}}) \tag{7}$$

For $-a \le x \le 0$ and $-c \le z \le 0$

$$-\lambda_s\left.\frac{\partial T_s}{\partial z}(x,y,z,t)\right|_{z=-c}=h_c(T_s(x,y,-c,t)-T_{\text{int}}) \tag{8}$$

For $-a \le x \le 0$ and $-b \le y \le 0$

- Interfaces soil-external walls of building :

$$\lambda_m\left.\frac{\partial T_m}{\partial x}(x,y,z,t)\right|_{x=-(a+em)}=-\lambda_s\left.\frac{\partial T_s}{\partial x}(x,y,z,t)\right|_{x=-(a+em)} \tag{9}$$

For $-b-e_m \le y \le 0$ and $-c-e_m \le z \le 0$

$$\lambda_m\left.\frac{\partial T_m}{\partial x}(x,y,z,t)\right|_{y=-(b+em)}=-\lambda_s\left.\frac{\partial T_s}{\partial x}(x,y,z,t)\right|_{y=-(b+em)} \tag{10}$$

For $-a-e_m \le x \le 0$ and $-c-e_m \le z \le 0$

$$\lambda_m\left.\frac{\partial T_m}{\partial x}(x,y,z,t)\right|_{z=-(c+em)}=-\lambda_s\left.\frac{\partial T_s}{\partial x}(x,y,z,t)\right|_{z=-(c+em)} \tag{11}$$

For $-a-e_m \le x \le 0$ and $-b-e_m \le y \le 0$

- Air temperature and water table temperature:

$$T(x,y,0)=T_{amb} \text{ and } T(x,y,-h)=T_w \tag{12}$$

For $-L \le x \le 0$ and $-d \le y \le 0$

The heat flow is calculated by the following equation:

$$Heat\ flow = \sum h_c dS\left(T_{\text{int}} - T_{wall}\right) \quad (13)$$

D. The local heat balance

The energy conservation law for the internal medium of the shallow basement, which is considered as an open system is:

$$\frac{dE}{dt} = \frac{\delta Q}{\delta t} + \frac{\delta W}{\delta t} \quad (14)$$

E is the total internal energy of the medium;

Q is the heat crossing the system boundary;

W is the total work that is a sum of the work done by the pressure forces on the control surface and the flow work.

Thus, the volume V of the control volume remain constant, and as a result, the boundary work is zero. The kinetic and potential energies of air in the cellar are neglected.

The air is considered as an ideal gas and the temperature of this one is uniform in the studied cellar, From the above assumptions, the equation 14 reduces to:

$$\rho_a C_{p_a} V \frac{\partial T_{\text{int}}}{\partial t} = qC_{p_a}(T_{amb} - T_{\text{int}}) + \sum_{i=1}^{3} h_c ds(T_{\text{int}} - T_{wall}) \quad (15)$$

III. RESULTS AND INTERPRETATION

A. Code validation

The researchers have elaborated a code that calculates the exchanged heat flow between a soil and shallow basement in 2D and 3D configurations. For computer code validation, they compared the results obtained by the present code and those of M. Krarti [10] carried out for the same geometric which is characterized by depth b=3 m, width a=2 m, total width L=9 m and for thick walls e=0.4 m in 3D configuration.

A non-uniform mesh in both directions, constructed using a geometric progression, was adopted with 36×38 grid dimension. Figure 4 shows good agreement between the results obtained by the proposed code and those of S. Amjad.

The heat flow is calculated by the following equation:

$$Heat\ flow = \sum h_c dS\left(T_{\text{int}} - T_{wall}\right)$$

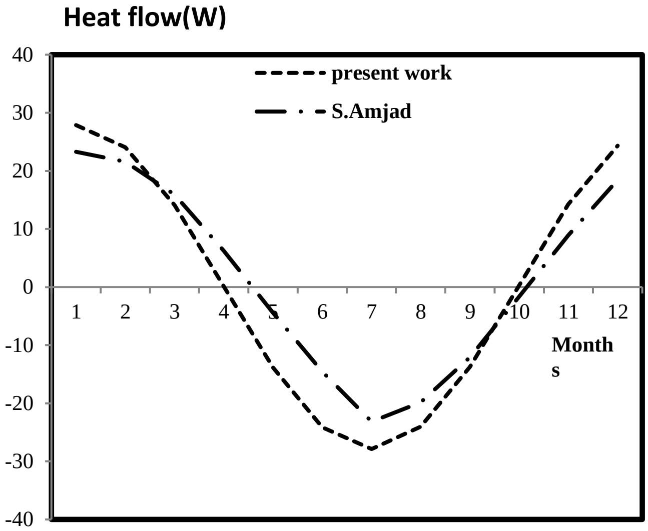

Fig .4. Variation of the monthly heat flux.

B. Effect of the distance L

At a large distance from the foundation, the effect of the shallow basement on the ground becomes negligible. To determine this distance, the researchers recognized several simulations by varying the distances L each time. Table 1 shows the monthly heat flows for each distance. This result indicated that little or no change in predicted heat flow occurs when the far-field boundary is at 8 m or more away from the building.

Table 1. Heat flow for different distances L.

Months	*heat flow L=2 m*	*heat flow L=4 m*	*heat flow L=6 m*	*heat flow L=8 m*
J	297.18	312.74	317.30	315.86
F	214.30	225.51	228.80	227.76
M	129.04	135.79	137.77	137.15
A	100.70	105.97	107.51	107.03
M	-7.49	-7.89	-8.00	-7.97
J	-1.00E+02	-1.06E+02	-1.07E+02	-1.07E+02
JU	-205.34	-216.10	-219.24	-218.24
A	-163.57	-172.14	-174.65	-173.85
S	-31.26	-32.90	-33.38	-33.22
O	-19.81	-20.85	-21.15	-21.06
N	118.40	124.60	126.41	125.84
D	193.23	203.34	206.31	205.37

C. *Effect of soil types*

To evaluate the soil type effect on the cellar internal temperature sensitivity to changes in the external environment, the researchers have performed simulations for three different soil types whose characteristics are presented in Table II.

Table 2. Characteristics of the studied soils.

Types of soil	Type 1	Type 2	Type 3
Thermal conductivity W/mK	2.00	1.15	0.32
Thermal diffusivity (10^{-7}) m^2/s	1.100	0.613	0.267

Figure 5 shows the change in the internal temperature of the cellar for three types of studied soil. The thermal conductivity and thermal diffusivity of wall and floor are λ_m=1.73 W/mK, and α_m=9.3.10^{-7} m^2/s, respectively.

In general, it is observed that there is stability in the internal temperature of the cellar throughout the year that can be explained by the considerable effect of inertia of the soil. This stability is even more important for soil 3 which is characterized by low conductivity and low thermal diffusivity.

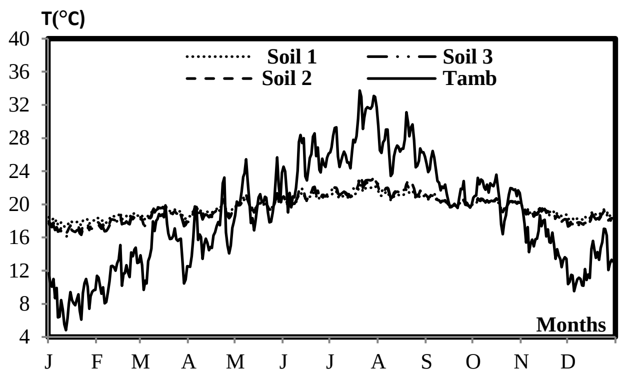

Fig .5. Daily variation of the external temperature and the internal temperature for three types of soil during a year.

In summer time, the outside temperature increases to 45 °C while that of the interior does not exceed 25 °C for sand and 23 °C for clay with 0.27% moisture content.

One can see a difference in indoor temperature between soil 2 and soil 3. This is due to the moisture content that influences the internal temperature of the shallow basement (Figure 6).

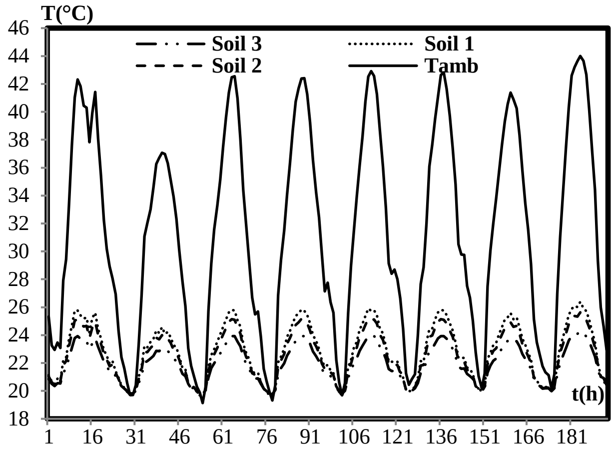

Fig .6. Hourly variation of indoor and outdoor temperature for one week of the summer period for three soil types.

During the winter period, the researchers found out that the cellar temperature does not descent below 16 °C for the three soil types, while the outer temperature recorded negative values in the range of -1 °C. They also found out that the internal temperature provides stability throughout the day with a small amplitude of 2 °C for soil type 1(clay) and 3 °C for soil type 3 (sand) for a weather temperature that have an amplitude of 12 °C (Figure 7).

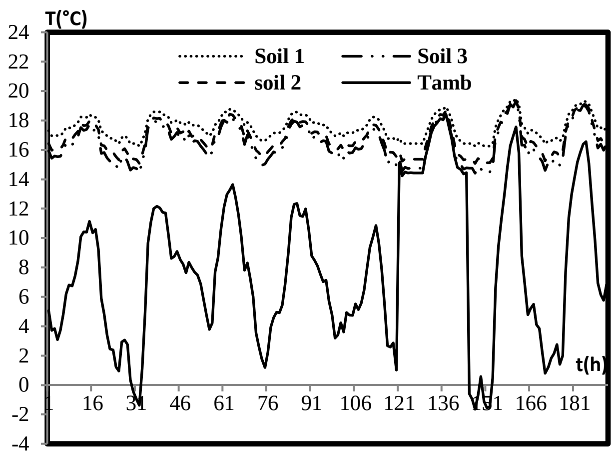

Fig .7. Hourly variation of indoor and outdoor temperature for one week of the winter period for three soil types.

Therefore, when analyzing the type of soil surrounding the building one should use accurate measurements of soil thermal proprieties (conductivity and diffusivity).

D. *Effect of the material type of the walls*

The determination of effect of construction materials on the internal temperature simulations was made for soil type 2 and for two building materials: reinforced concrete and hollow brick (Table III). The researchers observed that there is no significant difference between estimated temperatures for both materials. It can be deduced later that there is no effect on the nature of the walls of the internal temperature of the cellar for the studied cases (Figure 8).

Table 3. Characteristics of the studied walls.

Material type of the walls	*Hollow brick*	*Reinforced concrete*
Thermal conductivity W/mK	0.35	2.30
Thermal diffusivity (10^{-7}) m^2/s	3.90	9.58

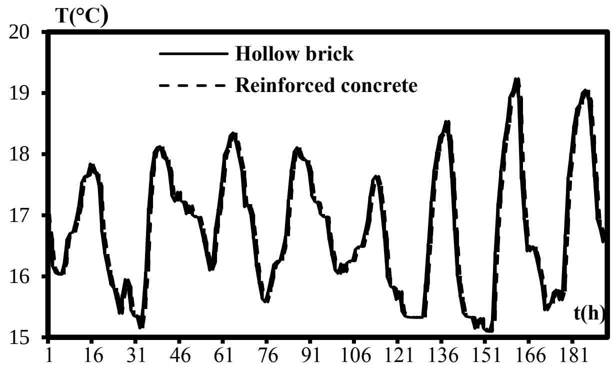

Fig .8. Hourly variation of indoor and outdoor temperature for one week of the summer period for two wall types.

E. Effect of the thickness of the walls

Figure 9 and Figure 10 are obtained for a soil type 2, reinforced concrete wall and for different wall thicknesses in the real climate of Marrakech. These results show that the influence of the wall thickness is not important; this is mainly due to the predominance of the thermal inertia of the soil compared to the walls cavity.

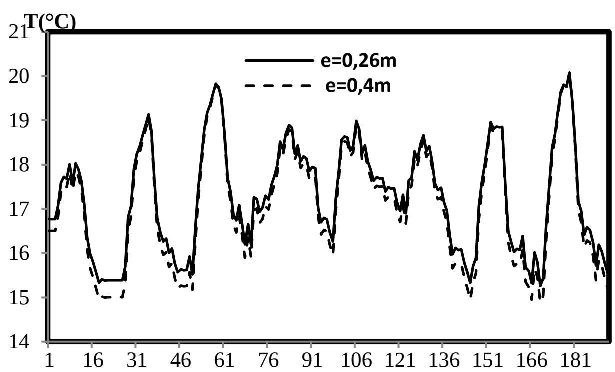

Fig .9. Hourly variation of the internal temperature for two thicknesses of the wall for a week during the winter period.

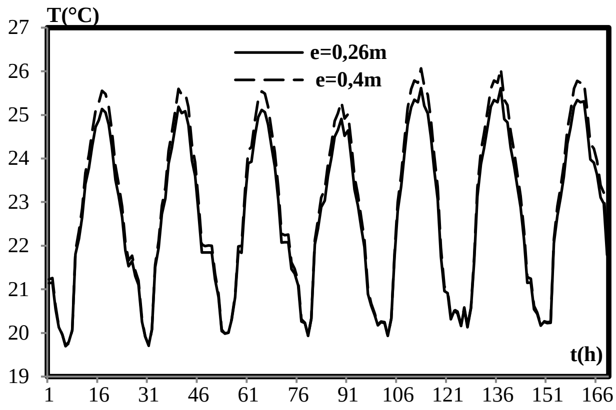

Fig .10. Hourly variation of the internal temperature for two thicknesses of wall for a week during the summer period

IV. CONCLUSION

In this study, the researchers have developed a detailed FORTRAN code to calculate three dimensional heat transfers for an envelope in contact with the ground. It allowed them to calculate the exchange of heat between the soil and the basement through the use of finite difference method in three dimensions and also calculate the internal temperature of the cellar, in the real climate of Marrakech.

We demonstrated the significant effect of the inertia of the soil on the stabilization of the internal temperature of the cellar. Indeed, the average temperature inside the shallow basement varies between 16°C and 24°C throughout the year, with a magnitude of 8°C. On the other hand, the ambient temperature is between 4°C and 34°C with the amplitude of 30°C.

This inertia is largely influenced by the thermal characteristics of the soil. In fact; the internal temperature is more stable with the ground having a low thermal conductivity and thermal diffusivity. During the summer season, the internal temperature does not exceed 24°C (Soil 1) and 25°C (soil 3) when the ambient temperature reaches 44°C. During the winter season, the ambient temperature descend down to -2°C, while the internal temperature did not descend below 15°C (soil 1) and 16°C (soil 3).

The study of the effect of the thickness of the wall and the wall-type shows that there is a difference of less than 1°C between the different studied situations (thickness and type of wall). So we can conclude that the type of wall and its thickness has little influence on the internal temperature of the cellar.

In conclusion, we deduce that the semi-buried building reduces the cooling and the heating loads through the stabilization of the internal temperature. On the other hand, the thermal characteristics of the ground are a great influence on the temperature inside the building in comparison to the type and thickness of the walls.

V. ACKNOWLEDGEMENTS

This study is a part of the RafriBAT project financially supported by a grant from the Hassan II Royal Academy of Sciences and Techniques, Morocco.

REFERENCES

[1] D. Chen, “Dynamic three-dimensional heat transfer calculation for uninsulated slab-on-ground constructions”, Energy and Buildings, No 60, pp. 420–428, 2013.

[2] A.E. Delsante, A.N. Stokes, and P.J. Walsh, “Application of Fourier transforms to periodic heat flow into the ground under a building“, International Journal of Heat Mass Transfer, Vol. 26, No.1, pp.121–132, 1983.

[3] S. Choi, M. Krarti, “Thermally optimal insulation distribution for underground structures”, Energy and buildings, No.32, pp. 251-265, 2000.

[4] W.P. Bahnfleth, “A three-dimensional numerical study of slab-on-grade heat transfer”, ASHRAE Transactions, No. 96, pp. 61–72, 1990.

[5] M.P. Deru, “Ground-coupled heat and moisture transfer from buildings”, National Renewable Energy Laboratory. NREL/CP-550-29694, February 2001.

[6] M. Staniec and H. Nowak, “Analysis of the energy performance of earth-sheltered houses with southern elevation exposed”, Eleventh International IBPSA Conference Glasgow, Scotland July 27-30, 2009.

[7] A. Abdelbaki, “Contribution à la modélisation des transferts thermiques à travers le plancher d’un habitat sur terre-plein” , DES thesis, Faculty of Sciences Semlalia, Marrakech, Morocco, 1993.

[8] A. Abdelbaki, S. Amjad, and Z. Zrikem, “Prediction of heat transfer from shallow basements to the soil by the two-dimensional transfer functions method”, in: Proceedings of the 3rd Renewable Energy Congress, Reading, UK, 1994.

[9] S. Amjad, “Contribution à l’étude du comportement thermique des bâtiments semi-enterrés”, DES thesis, Faculty of Sciences Semlalia, Marrakech, Morocco, 1997.

[10] S. Amjad, A. Abdelbaki, and Z. Zrikem, “Adaptation de la méthode des fonctions de transfert à une cavité enterrée”, in: Proceedings of the 3rd Mechanical Congress, Tétouan, Morocco, pp. 497–502,1997.

[11] L. Boukhattem, A. Bendou, R. Mir, and M. Kourchi, “Simulation et optimisation des transferts de chaleur entre un bâtiment complètement enterré et le sol”, Revue Internationale d'Héliotechnique, Energie – Environnement, No 36, pp. 27-35, 2007.

[12] L. Boukhattem, A. Bendou, H. Hamdi, and D.R. Rousse, “Simulation bidimensionnelle du transfert d’énergie entre un bâtiment semi-enterré et le sol en régime variable”, Revue internationale d'héliotechnique, N°.44, pp. 23-29, 2012.

Journal of Renewable Energy and Sustainable Development (RESD) Volume 2, Issue 1, June 2016 - ISSN 2356-8569
http://dx.doi.org/10.21622/RESD.2016.02.1.037

Lithium-ion Battery Degradation Assessment and Remaining Useful Life Prediction in Hybrid Electric Vehicle

Nabil LAAYOUJ [*], Hicham JAMOULI [*]
[*] LGII Laboratory, National School of Applied Sciences, Ibn Zohr University,
Agadir, Morocco
E-mail: nabil.laayouj@gmail.com

Abstract - Prognostic activity deals with prediction of the remaining useful life (RUL) of physical systems, based on their actual health state and their usage conditions. RUL prediction gives operators a potent tool in decision making by quantifying how much time is left until functionality is lost. In addition, it can be used to improve the characterization of the material properties, that govern damage propagation for the monitored structure. RUL can be predicted by using three main approaches, namely model-based, data-driven and hybrid approaches. Prognostic methods used later in this paper are hybrid and data-driven approaches, which employ the Particle Filter in the first one and the autoregressive integrated moving average in the second. The performance of the suggested approaches is evaluated in a comparative study on data collected from lithium-ion battery of hybrid electric vehicle.

Keywords - Remaining useful life; Prognosis; Particle Filter; ARIMA.

I. INTRODUCTION

Prognosis and health management (PHM) [1] will have significant impact on increasing safety as well as reducing operating and maintenance costs. This can be achieved by providing an accurate quantification of degradation and damage at an early stage to reduce or eliminate malfunctions. Furthermore, PHM consists of three main routines: fault detection, diagnosis and prognosis. A prognosis has recently attracted a lot of research interest due to the need of models for accurate RUL prediction [2].

Numerous methods and tools can be employed to evaluate the size of damage by predicting the RUL value. Prognosis techniques can be categorized under three approaches based on the usage of information: model-based, data-driven and hybrid approaches. The model based approach [3], assumes that a model of system behavior is available and uses this model to predict the future of the system behavior. Some recent developments in the model-based approach have been reported in the literature. Such as lumped parameter model [4], functional models [5] and first principal models [6].
The data-driven approach [7] aims at transforming the data provided by sensors into relevant models. In the literature, there are the following works: relevance vector machine [8] and neural network [9]. The hybrid approach [10] combines the two approaches cited earlier and includes Bayesian techniques [11][12].

In this work, the researchers will study two main approaches to predict RUL. The first approach is a hybrid prognosis using a Particle Filter method, which employs both, state dynamic model and a measurement data. The second approach is a data-driven prognosis based on routinely collected data, using autoregressive integrated moving average (ARIMA) model to estimate the system degradation.

The application of Particle Filters to prognosis has been reported in the literature. For example, prediction of lithium-ion battery capacity depletion [13], degradation prediction of a thermal processing unit in semiconductor manufacturing [14], and remaining useful life prediction of a mechanical component subject to fatigue crack growth [15]. The reported application results have shown that Particle Filters represent a potentially powerful prognosis tool due to its capability in handling non-linear dynamic systems and non-Gaussian noises, using efficient sequential importance sampling [16][17] to approximate the future state probability distributions.

Many works around ARIMA model have been developed. Among these are mechanical deterioration prognosis [18] [19] and economic forecasts [20][21]. In the present study, the researchers will use the ARIMA model to predict degradation by computing RUL.

This paper is organized as follows: section 2 contains the descriptions of the approaches at the basis of RUL prediction; in section 3, the results of the application of the methods are presented, and an evaluation of their performance is given; and finally, some conclusions on the advantages and limitations of the approaches are given in section 4.

II. SUGGESTED APPROACHES BASED ON THE RUL PREDICTION

A. Prognosis of degradation and remaining useful life

The term prognosis is originally used in medicine for the prediction of a course of an illness. But, later on it has been introduced to industry to predict the future operating status of equipments, and to set an efficient treatment.

The practitioner uses the results of the forecast models to determine the most appropriate treatment. These forecast models based on simple mathematical tools (e.g. decision tree, conditional probability) [22], or on more sophisticated (e.g. Markov processes, neural networks, and genetic algorithms) [23].

As mentioned earlier, the main objective of prognosis is to determine the time before failure. Note that the data prognosis is important information that may be used in the decision process. For example, this data prognosis can be used to delay the maintenance interventions, or stop a machine before its future maintenance due to earlier default.

B. Methods of prognosis

1. Particle filter for prognosis

The Particle Filter method [24] is a Monte Carlo technique for the solution of the state estimation problem. The key idea is to represent the required posterior density function by a set of random samples (particles) with associated weights, and to compute the estimations based on these samples and weights. As the number of samples becomes very large, this Monte Carlo characterization becomes an equivalent representation of the posterior probability function, and the solution approaches the optimal Bayesian estimation.

2. Particle filter model

Consider the dynamic system described by the following discrete time model [15]:

$$x_k = f_k(x_{k-1}, v_k) \quad (1)$$

$$z_k = h_k(x_k, \omega_k) \quad (2)$$

Where:

f_k : is the state transition function (damage model)

v_k : is state noise vector of known distribution

h_k : is the measurement function

ω_k : is the measurement noise vector

The goal of tracking is to recursively estimate x_k by using the set of all available measurements $z_{1:k} = (z_1, ..., z_k)$ up to time k, and to create a conditional state PDF (probability density function). Like any Bayesian estimation, two steps are employed: prediction and update.

In the prediction step, the researchers consider that the PDF $p\langle x_{k-1} | z_{1:k-1} \rangle$ previous state estimate at time $k-1$ and the process model (1), both are used to obtain the prior PDF of the state at time k as shown in Chapman-Kolmogorov equation.

$$p\langle x_k | z_{1:k-1} \rangle = \int p\langle x_k | x_{k-1} \rangle p\langle x_{k-1} | z_{1:k-1} \rangle dx_{k-1} \quad (3)$$

In the update step, at time , a measurement becomes available (from the likelihood function defined by the measurement model (2)), and this may be used to update the prior distribution to generate the posterior state PDF via Bayes rule (4).

$$p\langle x_k | z_{1:k} \rangle = \frac{p\langle z_k | x_k \rangle p\langle x_k | z_{1:k-1} \rangle}{p\langle z_k | z_{1:k-1} \rangle} \quad (4)$$

In order to obtain exact state estimation solutions for Equations (3) and (4), the actual distributions are approximated by a set of samples and their normalized weights. Consider $\{x_{0:k}^i, w_k^i\}_{i=1}^{N_S}$ a random measure that characterizes the posterior PDF

http://dx.doi.org/10.21622/RESD.2016.02.1.037

$p\langle x_k | z_{1:k}\rangle$, where $x_{0:k}^i$ and w_k^i are, respectively a set of support points and associated weights. The weights are normalized such that $\sum_i w_k^i = 1$. Then, the posterior density at time k is approximated [24] as

$$p\langle x_k | z_{1:k}\rangle \approx \sum_{i=1}^{N_S} w_k^i \delta(x_{0:k} - x_{0:k}^i) \tag{5}$$

The weight process based on importance sampling [24], such that the weight update equation is given by

$$w_k^i \propto w_{k-1}^i \frac{p\langle z_k | x_k^i\rangle p\langle x_k^i | x_{k-1}^i\rangle}{\pi\langle x_k^i | x_{0:k-1}^i z_{1:k}\rangle} \tag{6}$$

When $N_S \rightarrow \infty$ the importance density function $\pi\langle x_k | x_{0:k-1} z_{1:k}\rangle$ can be approximated by the prior PDF $p\langle x_k | x_{k-1}\rangle$, and weight becomes [16]

$$w_k^i \propto w_{k-1}^i p\langle z_k | x_k^i\rangle \tag{7}$$

Another problem arises is the Degeneracy phenomenon, where after a few iterations, all but one particle will have negligible weight. This degeneracy explains that a large number of updating particles is around zero. To overcome this problem, considering resampling procedure [25] at each step, the researchers assign $w_{k-1} = \frac{1}{N_S}$ for all the particle weights so they have

$$w_k^i \propto p\langle z_k | x_k^i\rangle \tag{8}$$

To implement SIR (sequential importance resampling) filter, as in (7) and (8), the researchers need to know process model, measurement model and likelihood function $p\langle z_k | x_k\rangle$

3. RUL Prediction using Particle Filter

Once the estimated parameter is obtained, the future damage state and RUL can be predicted by progressing the damage state until it reaches the threshold (Fig. 1). The PDF curve represents the progress of damage state until it reaches the threshold. The distribution of RUL can be obtained by subtracting this PDF from the threshold

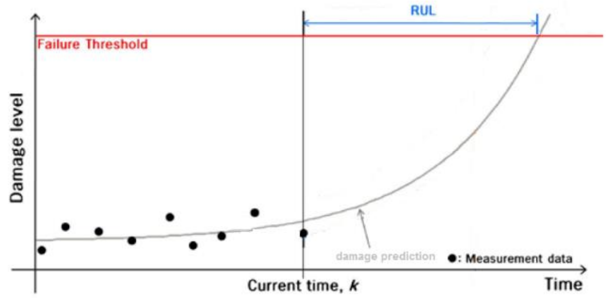

Fig .1. Illustration of RUL calculation

4. ARIMA model for prognosis

One of the important and widely used time series model is the autoregressive integrated moving average (ARIMA) model, which is a generalization of ARMA model. It requires only the historical time series data. These models are fitted to time series data to predict future points in the series (forecasting).

5. ARIMA forecasting method

ARIMA is a forecasting technique, noted as ARIMA (p,d,q), the general model was introduced by Box and Jenkins [26]. It is a method which allows both autoregressive (AR) and moving average (MA). It explicitly includes differencing in the formulation of the model. Where, p and q are, respectively, autoregressive parameter and moving average parameter, while d is the number of non-seasonal differences. The autoregressive part of the model of order p is written:

$$x_t = c + \sum_{i=1}^{p} \phi_i x_{t-i} + \varepsilon_t \tag{9}$$

Where x_t is a stationary series, x_{t-i} represents lag i of x_t, the ϕ_i, $i = 1,..., p$ are the parameters of the model, c is a constant and ε_t is a white noise. The moving average part of the model of order q is written:

$$x_t = \mu + \sum_{i=1}^{q} \theta_i \varepsilon_{t-i} + \varepsilon_t \tag{10}$$

Where the θ_i, $i = 1,...,q$ are the parameters of the model, μ is the expectation of x_t, which is often assumed to equal zero, and the $\varepsilon_t, \varepsilon_{t-1},..., \varepsilon_{t-q}$ are white noise error terms. After an initial differencing step (corresponding to the integrated part of the model), the researchers can present the ARIMA (p,d,q) as ARMA (p,q) process:

$$x_t = c + \varepsilon_t + \sum_{i=1}^{p} \phi_i x_{t-i} + \sum_{i=1}^{q} \theta_i \varepsilon_{t-i} \qquad (11)$$

The estimation of the ARIMA model corresponding to some learning data is done through Box and Jenkins methods [26]. A procedure of the forecasting can be summarized as:

- Check stationary: If the data are not stationary, they need to be transformed into stationary data using the differencing technique.
- Identification: to specify the appropriate number of autoregressive term p, and moving average term q from the autocorrelation function (acf) and partial autocorrelation function (pacf) correlograms.
- Forecasting: Based on the forecasting model, multi-step-ahead prediction is then conducted to forecast the final failure time.
- Verification: If the predictions result in an unexpected trend, repeat steps 2 and 3 until the model fits the historical data appropriately.

6. RUL prediction using ARIMA

Prediction of lifetime using ARIMA can be expressed in two parts: construction of model and prediction of state. In the first step, the researchers construct the corresponding coefficients (differencing, autoregressive and moving average terms) and they obtain an ARIMA model. Next step, when the model is built, a sample is selected to be estimated. Remaining Useful Life (RUL) is defined as the number of predictions from current state until the failure states reached the threshold. The following Fig. 2 shows the forecasting method for RUL prediction.

7. Hybrid electric vehicle (HEV)

An electric car is powered by an electric motor instead of a gasoline or diesel engine. The electric car (also known as electric vehicle EV) uses energy stored in its battery (or series of batteries), which are recharged by different sources. There is a variety of electric vehicles available in the world, among these HEV (hybrid electric vehicle), the PHEV (plug-in hybrid electric vehicle) and BEV (battery electric vehicle).

The researchers have oriented their work towards the HEV (Fig. 3), where a small battery is placed on board, and when the vehicle brakes, the energy is stored in the battery and it can later be used to power the electric motor which assists the gasoline engine. HEV typically provides better fuel economy than similar conventional vehicles. This is why it is necessary to develop a prognosis of battery degradation, in order to ensure a proper functionality.

The cell (or battery) studied in this work [27] is a lithium-ion with 1Ah capacity and 3.75 V. The cell is part of a battery pack (Battery pack= 15 cells) which is used to collect and distribute electric power (direct current power), mainly to the electrical drive. The researchers use the 25°C as the baseline for measurement. A simple form of the empirical degradation model is expressed by an exponential growth model as follows [28]

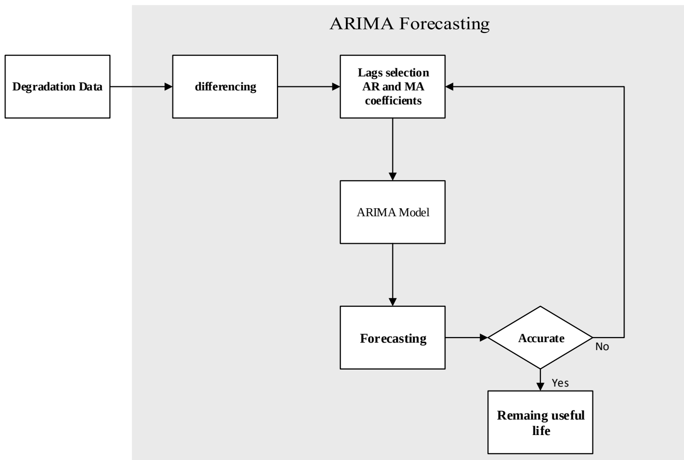

Fig .2. ARIMA prediction Algorithm

$$\lambda = a \exp(-bt) \qquad (12)$$

Where a, b are model parameters, t is the time, and λ is internal cell performance. The equivalent electrical model is introduced as shown in Fig. 4. where, C_{DL} is the double layer capacitance, R_{CT} is the charge transfer resistance, R_W is the Warburg impedance and R_E is the electrolyte resistance. The internal cell performance is observed instead of the capacity. Additionally, there is a relationship between $R_E + R_{CT}$ and $C/1$ capacity; $R_E + R_{CT}$ is inversely proportional to the $C/1$[28]. Also, the observed data are assumed to be given as a $C/1$ capacity. R_W and C_{DL} showed negligible change over the ageing process and are excluded from further analysis. The threshold for fault declaration has arbitrarily been chosen.

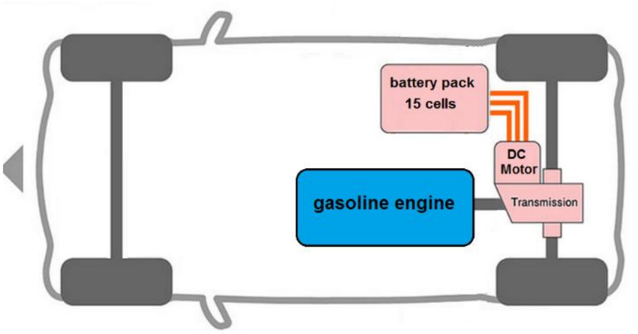

Fig .3. Plan of hybrid electric vehicle

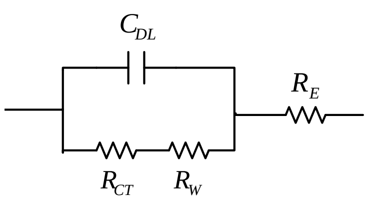

Fig .4. Equivalent circuit diagram of a Li-ion Cell

Table 1. Data of Degradation

Time (T)	Intial,1	2	3	4	5
C/1 (Ah)	1,000	0.981	0.859	0.811	0.788
Time(T)	6	7	8	9	10
C/1 (Ah)	0.714	0.680	0.612	0.56	0.568

8. RUL prediction and results

The Particle Filter uses the exponential growth model (12) to obtain the prior PDF (1). The measurement and process noise variance ω_k and v_k respectively were modeled as Gaussian densities. In the Particle Filter, a and b are incorporated as internal cell parameters R_E and R_{CT}. The values of a and b in the actual state are used as initial estimations. Then, the resampling of particles is applied to each iteration to solve the degeneracy problem. The predictions are progressed until they reach the threshold to get the RUL. The failure threshold is defined when the capacity fades by 35%.

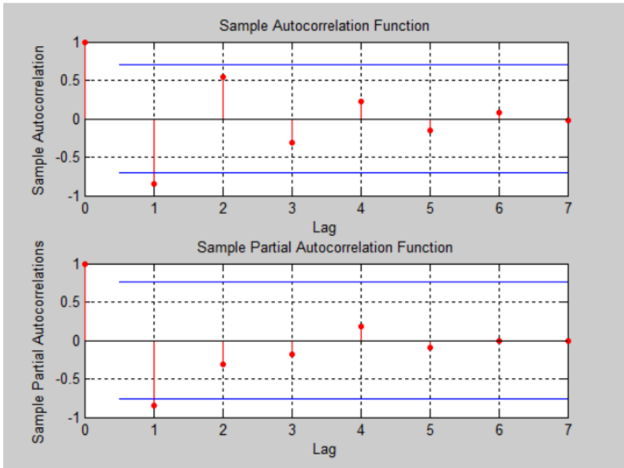

Fig .5. Autocorrelation and partial autocorrelation plots for ARIMA model

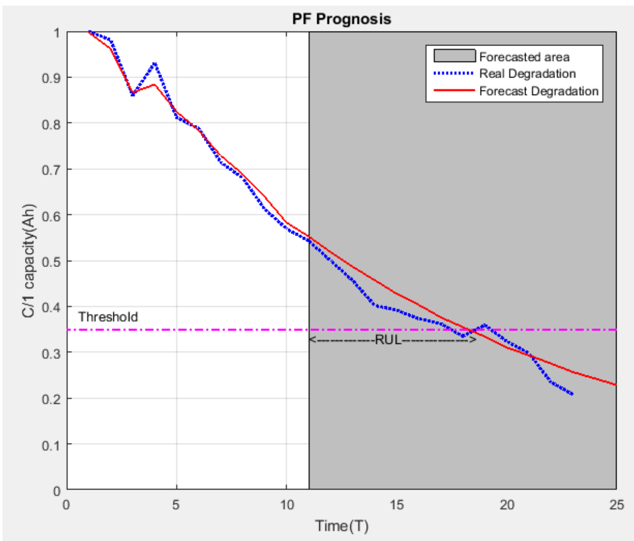

Fig .6. Trajectory of degradation for the cell of battery pack using Particle Filter

ARIMA (p,d,q) model uses simply the capacity data measurement to predict the future degradation. In our case, the data are roughly exponential in nature; d is chosen to be 2 in order to remove the non-stationarity, both p and q are chosen to be 1 (Fig. 5). The capacity data measurement at every 100 charge/discharge cycles are given in Table 1, where 1T=100 charge/discharge cycles.

Fig. 6 shows the real and the estimated values of the cell degradation using Particle Filter. Although the predicted results are close to the real values throughout the prediction area. In Fig. 7, the estimated data of the cell degradation obtained by ARIMA model are far off the real values after T=15.

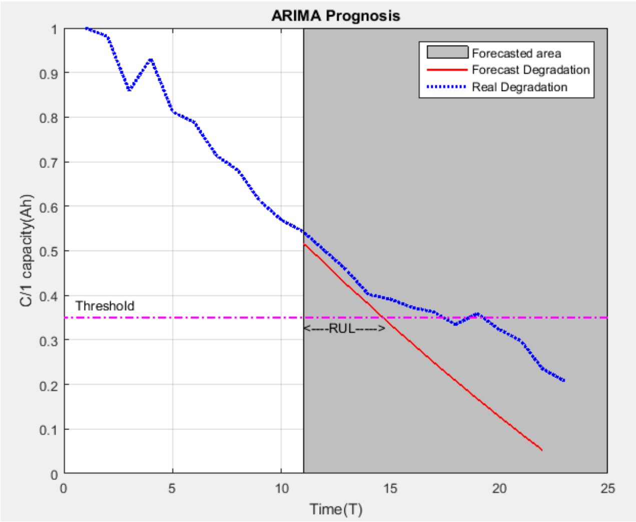

Fig .7. Trajectory of degradation for the cell of battery pack using ARIMA model

The performance of both methods has been evaluated by the Mean Absolute Scaled Error (MASE) [29] and Root Mean Square Error (RMSE).

Definition of MASE:

A scaled error is defined as

$$q_k = \frac{Y_k - \hat{Y}_k}{\frac{1}{N-1}\sum_{i=2}^{N}|Y_i - Y_{i-1}|} \qquad (13)$$

Where Y is the real value of testing cell, $\hat{Y}$ is the prediction value and N is the number of prediction data set. The MASE is simply

$$MASE = mean(|q_k|) \qquad (14)$$

Definition of RMSE:

$$RMSE = \sqrt{\frac{1}{N}\sum_{t=1}^{N}[Y - \hat{Y}]^2} \qquad (15)$$

The detail results are shown in Table 2.

Table 2. MASE and RMSE measurement of the cell prognosis

predictive approach	Particle Filter	ARIMA model
MASE	0,7345	2,6163
RMSE	0,0253	0,0719

From Table 2, one can find that the calculation of MASE and RMSE for ARIMA model is superior to the Particle Filter. Consequently, the Particle Filter is more accurate than the ARIMA model. In this study, the researchers have illustrated how the Particle Filter method can provide accurate predictions of the RUL, as presented in [28][30] over conventional data-driven methods without physical model.

III. CONCLUSION

In this study, the researchers interested here in two approaches for health prognostics using Particle Filter and ARIMA model. The goal in applying these methods is to calculate RUL. In addition, the RUL gives the best idea about the degradation of each system. The results showed that the Particle Filter was more faithful to the simulated data. The researchers considered different frequencies of inspection for the measurement.

This study highlights the value of having a physical failure model to improve the accuracy of results. In contrast, the ARIMA needs great possible historical data in order to give proper results without the need for physical model. However, the disadvantage of the Particle Filter compared to ARIMA model is the degradation model requirement, which is not always easy in the case of a large-scale system. Remember that both approaches require a knowledge of a threshold corresponding to the physical system failure to plan the actions of preventive maintenance, and expect to benefit from the opportunistic maintenance. Finally, the obtained results in this paper show that the Particle Filter is more efficient than the ARIMA model.

REFERENCES

[1] K. Medjaher, Tobon-Mejia and N. Zerhouni, "Remaining useful life estimation of ceritical components with application to bearings beliability", IEEE Transactions on, vol.61, no.2, 2012, pp.292-302.

[2] A. Mosallam, K. Medjaher and N. Zerhouni, "Bayesian approach for remaining useful life prediction", chemical engineering transactions, vol. 33, 2013, pp. 139-144.

[3] A. Heng, A. C. Tan, J. Mathew, N. Montgomery, D. Banjevic, and A. K. Jardine, "Intelligent condition-based prediction of machinery reliability", Mechanical Systems and Signal Processing, vol. 23, no. 5, 2009, pp. 1600–1614.

[4] C. J. and H. Lee, "Gear fatigue crack prognosis using embedded model, gear dynamic model and fracture mechanics", Mechanical systems and signal processing, vol. 19, 2005, pp. 836-846.

[5] P. Toguyeni, A. K. A and E. Craye "Structural and functional approach for dependability in FMS", IEEE International Conference on Systems, Man, and Cybernetics, 1999.

[6] Jaw, J.C, Inc, S. M. and Tempe, A. Z., "Neural networks for model-based prognostics", IEEE Aerospace Conference, 1999.

[7] M. Dong and D. He, "A Segmental Hidden Semi-Markov Model (HSMM)-based diagnostics and prognostics framework and methodology", Mechanical Systems and Signal Processing, vol. 21, no. 5, 2007, pp. 2248–2266.

[8] M. Tipping, the Relevance Vector Machine. In Advances in Neural Information Processing Systems, MIT Press, Cambridge, 2000.

[9] A.N. Srivastava and S. Das, "Detection and prognostics on low dimensional systems", IEEE Transactions on Systems, Man, and Cybernetics, Part C: Applications and Reviews, vol. 39, 2009, pp. 44-54.

[10] J. Yan and J. Lee, "A hybrid method for on-line performance assessment and life prediction in drilling operations", IEEE International Conference on Automation and Logistics, 2007.

[11] J. W .Sheppard, M. A. Kaufman, A. Inc and M. D. Annapolis, "Bayesian diagnosis and prognosis using instrument uncertainty", IEEE Autotestcon, 2005, pp. 417 423.

[12] B. Saha and K. Goebel, "Uncertainty management for diagnostics and prognostics of batteries using Bayesian techniques", IEEE Aerospace Conference, 2008.

[13] B. Saha, K. Goebel, S. Poll, and J. Christophersen, "Prognostics methods for battery health monitoring using a Bayesian framework", IEEE Transactions on Instrumentation and Measurement, vol. 58, no. 2, 2009, pp. 291-296.

[14] S. Butler and J. Ringwood, "Particle Filters for remaining useful life estimation of abatement equipment used in semiconductor manufacturing", Proceedings of the First Conference on Control and Fault-Tolerant Systems, Nice, France, 2010, pp. 436 - 441.

[15] E. Zio and G. Peloni, "Particle filtering prognostic estimation of the remaining useful life of nonlinear Components", Reliability Engineering and System Safety, vol.96, 2011, pp. 403- 409.

[16] B. Ristic, S. Arulampalam, N. Gordon, Beyond the Kalman Filter, Artech House, Boston, 2004.

[17] A. Kong, J.S. Liu and W.H. Wong, "Sequential imputations and Bayesian missing data problems", Journal of the American Statistical Association, vol. 89, no. 425, 1993, pp. 278-288.

[18] P. Kosasih, W. Caesarendra, A. K.Tieu, A. Widodo & Moodie, C. A. S, "Degradation trend estimation and prognosis of large low speed slewing bearing lifetime", Applied Mechanics and Materials, 493, 2014, pp. 343-348.

[19] A. Guclu1, H. Yılboga1, O. F. Eker, F. Camci, I. Jennions, "Prognostics with autoregressive moving average for railway turnouts", Annual Conference of the Prognostics and Health Management Society, 2010.

[20] G. Peter Zhang, “Time series forecasting using a hybrid ARIMA and neural network model”, Neurocomputing 50, 2003, pp. 159 – 175.

[21] M. E. Andreica, N. Cataniciu, M. I. Andreica. “Econometric and neural network analysis of the labor productivity and average gross earnings indices in the romanian industry”, Proceedings of the 10thWSEAS International Conference on Mathematics and Computers in Business and Economics, Mar 2009, pp.106-111.

[22] V. Tran, B. Yang, O. MS, A. Tan, “Machine condition prognosis based on decision trees and one-step-ahead prediction”, Mechanical System and Signal Processing, vol. 22, 2008, pp. 1179-1193.

[23] P.J.F. Lucas and A. Abu-Hanna, “Prognostic methods in medicine”, Artificial Intelligence in Medicine, vol. 15, 1999, pp.105-119.

[24] S. Arulampalam, S. Maskell, N. Gordon and T. Clapp, “A tutorial on Particle Filters for on-line non-linear/non-Gaussian Bayesian tracking”, IEEE Trans. Signal Processing, vol. 50, 2001, pp. 174-188.

[25] N. J. Gordon, D. J. Salmond, A. F. Smith, “Novel approach to nonlinear/non-Gaussian Bayesian state estimation”. IEEE Proceedings F (Radar and Signal Pro-cessing) (vol. 140, no. 2), 1993, pp. 107-113.

[26] G.B.P. Box, G.M. Jenkins, G.C. Reinsel, “Time series analysis, forecasting and control”, 3rd ed., Prentice Hall,Englewood Cliffs, NJ, 1994.

[27] K. Smith, M. Earleywine, E. Wood, J. Neubauer and A. Pesaran, “Comparison of plug-in hybrid electric vehicle battery life across geographies and drive”, SAE international, 2012.

[28] B. Saha1, K. Goebel and J. Christophersen, “Comparison of prognostic algorithms for estimating remaining useful life of batteries”, Transactions of the Institute of Measurement & Control, vol. 31, no. 3-4, 2009, pp. 293-308.

[29] R. J. Hyndman et A. B. Koehler, “Another look at measures of forecast accuracy”, International Journal of Forecasting, 22, 2006, pp. 679-688.

[30] D. An, J. Choi and N. Ho Kim, “A tutorial for model-based prognostics algorithms based on matlab code”, Annual Conference of Prognostics and Health Management Society, 2012.

Journal of Renewable Energy and Sustainable Development (RESD) Volume 2, Issue 1, June 2016 - ISSN 2356-8569
http://dx.doi.org/10.21622/RESD.2016.02.1.045

Urban Temperature Analysis and Impact on the Building Cooling Energy Performances: An Italian Case Study

Michele Zinzi [1], Carlo Romeo [1], Emiliano Carnielo [2], Alessandro Mangione [3]
[1] Energy Efficiency in Buildings Unit, ENEA, Rome, Italy
[2] Department of Engineering, University of Rome Tre, Rome, Italy
[3] Architect, Rome, Italy.
michele.zinzi@enea.it

Abstract **-** The heat island effect in urban environments, (whatever the size and the latitude determining the effect intensity) is dramatically increasing due to climate changes and urban sprawl. The urban heat island is a phenomenon observed since the last decades of the XIX century, but diffused to a large scale only one century later. It is characterised by the increase of air temperature in densely built urban environments with respect to nearby natural landscape areas. Many available studies show urban heat island intensities up to 12°C. This thermal stress causes social, health and environmental hazards, with major impacts on weak social classes, such as elderly and low income people. This study presents first results of air temperature monitoring campaigns in different neighbourhoods of Rome, a metropolitan area characterised by a typical Mediterranean climate and by a complex urban texture, in which densely built areas and green or not-built zones border one another. Six spots were monitored since June 2014; they include: historical city centre, semi-central zones with different construction typologies, and surrounding areas with various urban and building contexts. This paper explores the summer temperature profiles within the city and their increase respect to suburban areas' values. UHI intensities up to 10°C were monitored as well as monthly UHI up to 3.4°C in the hottest area of the city. The impact on the cooling performance and the thermal response of reference buildings were also assessed. Temperature datasets and the reference building model were inputted into adynamic calibrated calculation software. In addition, cooling net energy demand of the reference building as well as operative temperature fluctuation in the not cooled building configuration were calculated. The results of calculation allow to compare the energy and thermal performances in the urban environment with respect to the reference conditions, being the latter typically adopted by national building codes. 50 and 100% relative increasing of cooling demand were calculated, respectively, for insulated and not insulated buildings.

Keywords **-** Urban temperature; building cooling energy performances; thermal comfort.

I. INTRODUCTION

Climate change is probably the most relevant challenge at planetary level in the coming years. Climate change is proved by scientific observations and predictions since years [1]. The global warming is strictly linked to climate change, which is occurring at all latitudes, although in different modes and intensities. The Mediterranean area is deeply interested in this phenomenon and several studies predict air temperature rise above 2°C in absence of adequate mitigation policies. It isimportant noting that the increase of average temperatures is not the only effect since the increase of extreme phenomena as heat waves and hot spells is also documented [2].

This area is also undergoing an urbanisation process since decades. This is again a global process, but particularly critical for Europe and the Mediterranean area, where the urbanisation increased from 54 to 66% during the years between 1970 and 2010. More than 300 million inhabitants lived in urban areas in 2010, while the figure was 150 million in 1970 [3].

The combined effect of global warming and urban sprawl is the cause of the Urban Heat Island (UHI) effect, which is defined as the increase of the air temperature in urban areas compared to that in the countryside, adjacent to the city. It can be referred to instantaneous values (UHI intensity) or to average values related to different time steps (from hourly to seasonal).

The phenomenon is physically observed since the 19th century [4], but it has been extensively studied only since few decades, when the above illustrated causes made it clearly evident [5, 6, 7, 8]. Many studies are now available showing the UHI is observed at every latitude and the main factors are: green permeable areas reduction; the decrease of radiative heat loss due to the canyon effect; increase of thermal storage in buildings; anthropogenic heat released by buildings and transport systems; evaporative cooling reduction; high shortwave absorption due to low albedo materials used for buildings and pavements; solar radiation trapped under the canopy, favoured by masking and shadowing.

The UHI has several implications at environmental, social, economic and energy levels. This paper deals with the last mentioned topic, being the relation between urban heat island and energy issues the most relevant among those investigated in several studies [9, 10, 11, 12]. The study discusses several themes, namely the impact of urban temperatures on the building energy and peak demands for cooling; the impact on thermal comfort and potential passive cooling technique such as the use of materials, technologies and strategies to mitigate the urban heat island and to improve the thermal response of buildings.

II. OBJECTIVE AND METHOD

This paper analyses the air temperature distribution within the city of Rome (Italy) and provides first data about its impact on the energy and thermal response of residential buildings. The main objective of the present study is to provide an initial assessment of urban temperatures' impact on summer energy performance of buildings highlighting the potential discrepancies between the official weather data set, generally derived from measurements taken outside the city, and the effective thermal conditions registered in urban areas.

The extension of the urban area of Rome is about 1,287 km2 with 2.87 million of inhabitants which could reach nearly 4 million considering the whole metropolitan area. This urban pattern is very articulated: densely built zones alternate to un-built and green areas. Furthermore, building stock's characteristics are extremely variegated in terms of urban lay-out; geometry, size, construction technologies and more.

For this study six zones are selected and their thermal response is compared to an undisturbed reference station (the ENEA research centre) located in the countryside, 25 km north of the city centre. The selected zones are the following:

- Z1 Historical city centre. A densely built area with Middle Ages massive buildings (height between 12-20 meters) characterised by mainly narrow streets (up to 10 meters), no vegetation, except few gardens belonging to historical mansions, and dark stone urban paving.
- Z2 Prati district. A central area, built in the late 19th century. It is characterised by massive courtyard buildings, 25 meters high on large tree-lined streets in asphalt, which creates a regular grid. The area is close to the Tevere river.
- Z3 Monteverde district. Dates back to the early 20th century. This area is densely built and characterised by small apartment blocks and narrow asphalt streets (8-10 meters), few green areas, mainly private gardens adjacent to the buildings.
- Z4 Ostiense district. Built in different periods, it is characterised by high buildings (30 meters) along a 60 meter wide boulevard with trees in the middle. The area is also characterised by large empty urban spaces, mainly covered with asphalt (e.g. parking lots).
- Z5 Tuscolana district. A semi-peripheral area developed in the '50s and '60s with linear and tower buildings between 20 and 30 meters high. It presents a wide main street and 10-12 wide lateral roads. The neighbourhood is surrounded by some green areas, but the district itself has negligible vegetation inside.
- Z6 Torrevecchia district. A peripheral area built in the '40s which mainly consists of small apartment blocks (3-5 floors). It is an articulated neighbourhood, with asphalted streets of different width and characterised by extensive green areas.
- Different urban textures of the city can be inferred by the aerial views of Zone 1 and 6 reported in Figures 1 and 2.

Air temperature and relative humidity have been continuously measured in the seven stations in order to identify the thermal stress within the selected zones respect to the undisturbed station allowing to quantify the impact of the city in term of temperature rise.

Journal of Renewable Energy and Sustainable Development (RESD) Volume 2, Issue 1, June 2016 - ISSN 2356-8569
http://dx.doi.org/10.21622/RESD.2016.02.1.045

Fig .1. Aerial view of Zone 1

Fig .2. Aerial view of Zone 6

In the next step the measured climatic data are used as input to calculate the thermal response of a reference residential building under two operative conditions:

- Energy performance of the building equipped with a mechanical cooling system. The net energy demand is calculated, assuming an ideal energy system characterised by unlimited power, in order to focus the performance on the building structure response;
- Thermal comfort of the building in free-floating conditions, meaning that no mechanical cooling system is installed. The results allow quantifying the impact of urban heat island and associated temperature profile on the building thermal response.

III. MONITORING CAMPAIGN

The monitoring campaign started in June 2014 and it is still going on, since the objective is to have robust data files, able to describe the thermal response of the city across a significant period (e.g. 2 years). The seven stations are installed at 4-6 meters high from the ground level and under the canopy. They consist of a self-standing data logger and a sensor set exposed to solar radiation. The relevant sensor data are:

- °C temperature resolution in the 40-82 °C range;
- ±0.5 °C maximum temperature error in the -5-60 °C range;
- 0.1% humidity resolution in the 0-100% range;
- ±5% maximum humidity error in the 10-100% range.

Data are acquired every 10 minutes and averaged on 1 hour time steps for evaluations and calculations. This study is based on the data collected from July 1st to September 20th, covering most of the 2014 cooling season.

IV. CALCULATION

The numerical analysis was carried out using TRNSYS, a well-known and calibrated tool, able to dynamically model the thermal behaviour of buildings [15]. The software operates by means of hourly energy balance of the thermal zones. The TRNSYS model implemented for this analysis consists of sub-routines, called types, to which the whole calculation phase is assigned. The reference building used for the study purpose is a three storeys block with two apartments on each floor. Each apartment has three external façades and the main geometric characteristics are the following: net floor area 89 m2, net volume 240 m3, and windows area 10.5 m2.

Two configurations are investigated with and without thermal insulation. U-values of the building components are summarised in Table I; internal gains are set to 5 W/m2. For the energy assessment an external shading of 0.4 is assumed for windows and the air exchange rate is set to 0.3 ACH. The net cooling energy demand is calculated considering an ideal energy system working continuously. Set-points are 26 °C for the air temperature and 60% for the relative humidity. For the free floating analysis an external shading factor of 0.7 is assumed for windows and the air exchange is set to 0.5 ACH during daytime and 2 during night-time. These assumptions derive from conscious user behaviour in not cooled buildings.

Table 1. U-VALUES OF BUILDING COMPONENTS

Building configuration	U-roofs [W/m²K]	U-wall [W/m²K]	U-ground [W/m²K]	U-window [W/m²K]
Not insulated	1.1	1.1	1.2	5.8
Insulated	0.38	0.4	0.5	2.8

V. RESULTS

The results refer to the monitoring campaign of the urban temperature and to the simulations, carried out to estimate the impact of temperature increase on the energy and thermal performance of the reference building.

A. Urban temperature profiles

The results show that the temperatures in the cities are higher than in the reference station. Table II reports the UHI values monthly averaged throughout the whole period of investigation for the 6 monitored zones. The most affected districts by the phenomenon revealed not necessarily the most central ones. Z5 is a semi-peripheral but a heavily built area and this makes it the most UHI affected in the city, with 3.2 °C during the whole period. Z1 and Z4, similarly to Z5, but not with the same density, show UHI values of 2.4 °C and 2.2 °C respectively. Z2 and Z3 represent two heavily built central areas, where the presence of the river nearby (for Z2) and trees along the streets partially mitigate the climate: UHI is slightly lower than 2°C. Z6 is similar to Z3 as construction typology but, being more peripheral, is the least affected by UHI (1.5°C) among all the monitored zones. It is worth mentioning that the results are mitigated by the September climate during the peak month, namely August, the monthly UHI is between 0.1 and 0.2 °C higher than the UHI values averaged over the period.

Hourly data analysis provides even more detailed information. The UHI measured intensities for the six zones are in order: 7.9, 6.6, 6.5, 7.0, 9.9 and 6.0 °C. These data provide an impressive measure of the impact of the built urban environment on the thermal profiles of the city. It is also worth mentioning that cool island effects are measured in all the zones, even if they are limited in the number of hours (only few hours of the morning) and in intensity so as to be considered irrelevant. Typical variations of the UHI are plotted in figure 3, where the values refer to four days in August. Peak values reach 4 °C in all the zones and, in some cases, 5 °C can be observed. The data show a more intense UHI during night time. Table III shows an extended set of the cumulative distribution of the UHI exceeding some reference values (from 2 to 5 °C). In Z5 the UHI is higher than 3 and 5 °C respectively during the 50% and 15% of the monitoring period, confirming this area as the hottest of the city. Z1 and Z4 present similar results: the hourly UHI exceeding 2 and 3 °C for about the 60% and 30% of the total hours, respectively. For the remaining zones, a UHI above 3 °C is measured for 10% and 20% of the monitored period.

Table 2. MONTHLY AND PERIOD UHI VALUES IN MONITORED ZONES

Month	Z1 UHI [°C]	Z2 UHI [°C]	Z3 UHI [°C]	Z4 UHI [°C]	Z5 UHI [°C]	Z6 UHI [°C]
Jul.	2.5	1.6	2.0	2.2	3.1	1.5
Aug.	2.6	1.8	2.0	2.3	3.4	1.6
Sep.	1.9	1.5	1.5	2.0	2.8	1.3
Period	**2.4**	**1.7**	**1.9**	**2.2**	**3.2**	**1.5**

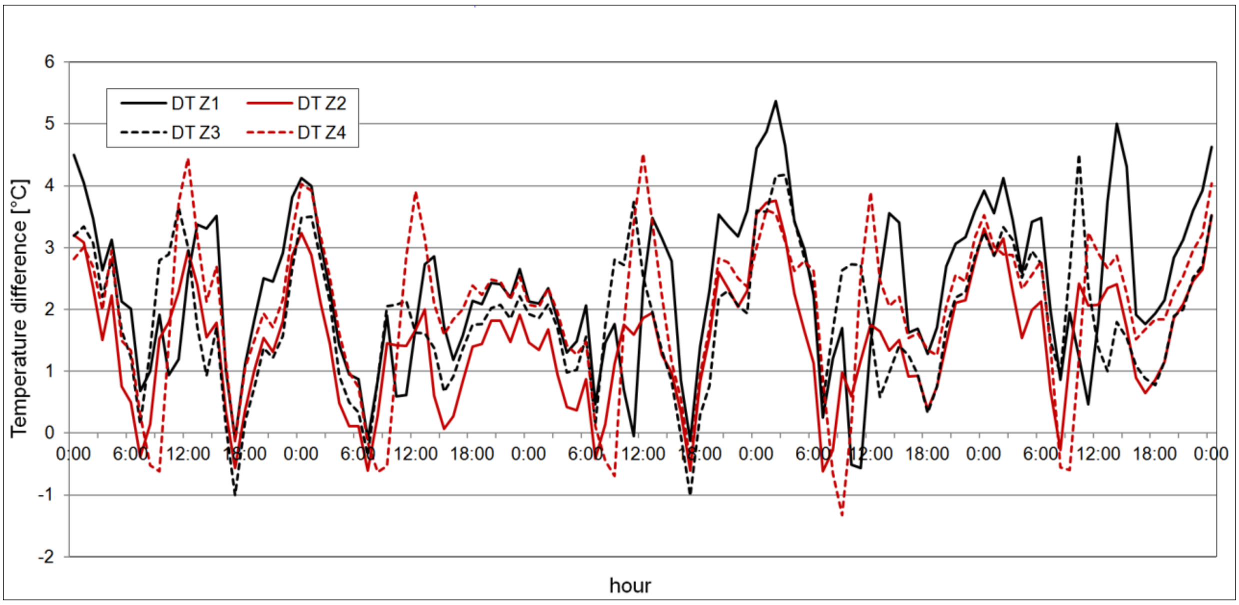

Fig .3. UHI for selected zones during 4 days in August

Journal of Renewable Energy and Sustainable Development (RESD) Volume 2, Issue 1, June 2016 - ISSN 2356-8569
http://dx.doi.org/10.21622/RESD.2016.02.1.045

Table 3. HOURS OCCURRENCE OF UHI FOR THE MONITORED ZONES

Temp. [°C]	Z1 UHI [°C]	Z2 UHI [°C]	Z3 UHI [°C]	Z4 UHI [°C]	Z5 UHI [°C]	Z6 UHI [°C]
>2	1194	674	827	1168	1508	571
>3	603	220	352	477	1011	202
>4	243	69	135	129	555	59
>5	85	14	41	20	290	8

Table 4. HOURS OCCURRENCE OF AIR TEMPERATURES FOR THE MONITORED ZONES

Temp. [°C]	Z1 hours	Z2 hours	Z3 hours	Z4 hours	Z5 hours	Z6 hours	Ref hours
<16	0	4	2	0	0	3	52
<18	18	50	23	15	6	31	205
<20	123	234	156	141	68	226	545

The results in Table IV present the hours during which temperatures fall below some reference values. It can be noted that practically the temperature never drops down 16°C in the city, while this is verified for more than 50 hours in the reference station. The number of hours in which temperature is below 18 °C ranges between 6 and 50 (average 23.8) within the city; this value exceeds 200 in the ENEA station. It is also worth noting that high variable results can be observed within the city stations; the differences are not directly connected to the distance from the city centre since a more complex mechanism emerges depending on the density of the built environment and the presence of green areas affecting the zone thermal conditions.

B. *Energy and thermal performance of the reference building*

Figure 4 presents the net energy cooling demand (in kWh) of the reference building, during the monitoring period and for the six zones plus the extra urban station. The figure reports the results for the insulated and not insulated configurations. As expected, the energy demands are in line with the data observed for the outdoor temperatures. It is also worth noting that for all the city zones the energy demand decreases as an effect of the thermal insulation, while the contrary applies to the reference station. The phenomenon mainly depends on the effect of the insulation which counters the thermal discharge of the building structure when the night temperatures significantly drop. It is calculated that the extra cooling demand normalised respect to the net floor area is about 10 kWh/m2, while in the city it ranges between 13 and 18 kWh/m2.The impact on the urban temperatures can be also inferred from figure 5, where the relative increase of the cooling demand respect to the reference station is depicted for the 6 city zones. The increase for the not insulated configurations ranges between 50% (Z2 and Z6) and 100% in Z5. The variations are smaller for the insulated configurations, since all the energy performances improve when considering the buildings within an urban context, while the reference station building shows an increase of the cooling demand. The curve, moreover, shows a more flat trend: the energy penalties are about 50% in Z5, which is confirmed to be the hottest zone, and the global variation is between 24 and 37% for the other five zones.

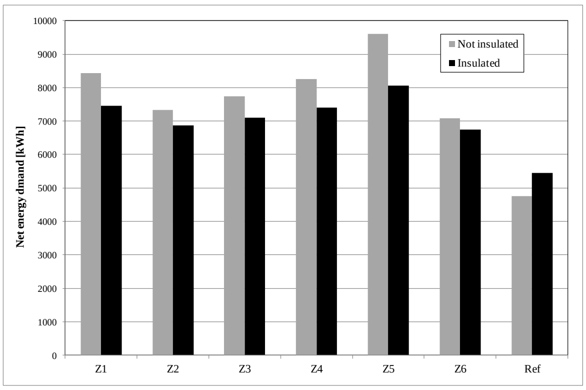

Fig .4. Net energy cooling demand of the reference building in the six monitored zones and for the reference station

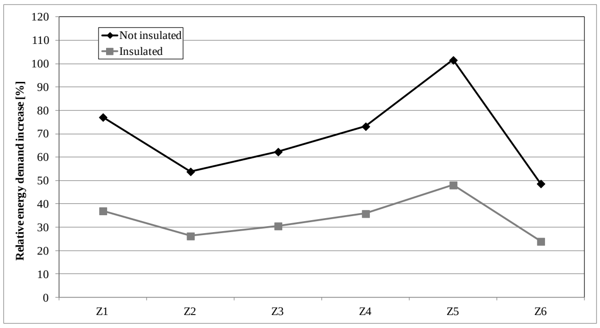

Fig .5. Relative increase of the net cooling energy demand of the building located in the six zones respect to the reference station cooling demand

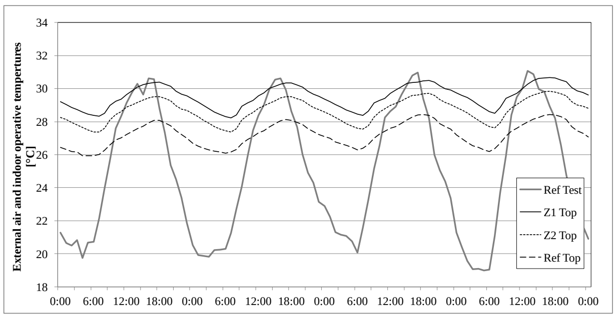

Fig .6. Evolution of ambient air and indoor operative temperature in selected zones

The calculation also allows highlighting the effect of the urban temperature on the not cooled building based on the fluctuation of the operative temperature in a selected apartment of the block. As an example, four typical August days results are shown in figure 6 where external air in the reference zone and the operative temperatures in Z1, Z2 and reference zone are plotted for the not insulated building. The operative temperature in the reference zone remains below 28 °C as a peak with the adopted building configuration, which is in line with the comfort expectations according to the adaptive methods. Z1 building is more critical since the operative temperature remains above 30 °C from 6 to 9 hours per day and it never goes below 28.2 °C. Z2 building shows a less intense thermal stress: the operative temperature remains always lower than 29.5 °C and drops below 28 °C at night-time.

Data in Table V provide aggregate information about the buildings thermal response during the whole period. The average temperature for the reference station is 25.6 °C, in line with thermal comfort expectations. Z1 and Z5 present average operative temperatures higher than 28 °C, while operative temperatures vary between 27.1 and 27.8 °C for the remaining four zones. Z5 building operative temperature is 3.2 °C higher with respect to the reference station building, while it varies between 2.2-2.4 °C for Z1 and Z4. It remains below 2 °C for the remaining zones. The thermal insulation causes an increase average temperature increasing of 0.8-0.9 °C for all the selected zones. This implies that difference regarding the reference station buildings remains basically equal to that found for the not insulated case.

Results can also be observed in terms of cumulative distribution of the operative temperatures in the buildings for the different city zones. Table VI shows these results for the not insulated configuration. The reference zone results are not reported since an operative temperature higher than 28 °C is reached only in 100 hours and it never reaches 29 °C, implying that thermal comfort conditions are assured in most of the monitored period. Different results are achieved for the other zones. The most critical one is Z5 where the temperature is higher than 30°C for the 20% of the period and in Z1 where this happens in the 10% of the calculated hours. Temperatures above 28°Care reached in a percentage of the period ranging between 28 and 68%, so the overheating risk applies to all the monitored zones. Anyway, extreme phenomena can be expected only for a short period (1 to 6% of the calculated hours) in zones Z2, Z3, Z4 and Z6.

Table 5. AVERAGE OPERATIVE TEMPERATURE AND DIFFERENCES VERSUS THE REFERENCE STATION BUILDING

Tm_op [°C]	Z1 hours	Z2 hours	Z3 hours	Z4 hours	Z5 hours	Z6 hours	Ref hours
NIns	28.0	27.2	27.5	27.8	28.8	27.1	25.6
ΔNIns	2.4	1.7	1.9	2.2	3.2	1.5	---
Ins	28.9	28.1	28.4	28.6	29.6	28.0	26.4
ΔIns	2.5	1.7	2.0	2.2	3.2	1.6	---

Table 6. HOURS OF OPERATIVE TEMPERATURE IN THE CITY BUILDINGS

Temp. [°C]	Z1 UHI [°C]	Z2 UHI [°C]	Z3 UHI [°C]	Z4 UHI [°C]	Z5 UHI [°C]	Z6 UHI [°C]
>28	1020	599	750	897	1331	546
>29	530	218	304	377	898	189
>30	193	30	76	119	412	25
>31	33	0	0	4	133	0

Results provided by the simulation carried out on the insulated building show an increase of overheating risk. Hours with operative temperature above 30°C double in Z1 and Z5. This threshold value is not completely negligible for the remaining monitored zones, since an occurrence between 10 and 18% of the period is calculated.

VI. DISCUSSION AND CONCLUSIONS

This paper presents preliminary results of a study aimed at assessing the impact of the urban thermal climate on the energy and thermal response of reference buildings during the cooling season in the city of Rome, Italy. The study is focused on a limited observation period, since the monitoring activity refers to the initial phase of the campaign that started in July 2014, and is still on-going. Air temperature and relative humidity were continuously measured in six districts, as well as in an extra urban reference station.

The results show that city of Rome is affected by a significant increase of the air temperature, namely Urban Heat Island phenomenon. UHI intensities range between 6 (Z6) and 9.9°C (Z5), while monthly UHI ranges between 1.3°C in Z6 in September and 3.4°C in Z5 in August. Referring to the whole period, UHI varies between 1.5°C (Z6) and 3.2°C (Z5). Energy analysis shows a significant increase of the cooling energy demand respect to the reference station out of the city. Relative increase of the demand ranges between 50 and 100% for the not insulated building, while the increase is almost reduced by half for the insulated configuration. In terms of averaged operative temperature values over the whole observation period, the increase for the reference station is between 1.5°C and 3.2 °C. The registered values also show an increase of 0.8-0.9°C for the insulated configuration with respect to the not insulated one.The study shows how severe the urban climate is in the city of Rome and how risky it could be for building occupants during hot periods in summer. City cooling strategies should be implemented to mitigate as much as possible the thermal conditions. Some areas could benefit of extended vegetation to take advantage of evaporative cooling (Z2, Z4, Z6); some other zones have an urban texture that does not allow significant modifications, in this case a conscious building design and urban materials with higher albedo values should be used to control temperatures. During night time, passive and ventilated cooling techniques should be implemented. The city monitoring campaign is still on-going. Next steps will include both winter and summer analyses with a more extended data set, based on the continuous monitoring of air temperature and relative humidity.

REFERENCES

[1] IPCC, Climate Change 2007: Synthesis Report. Contribution of Working Groups I, II and III to the Fourth Assessment Report of the Intergovernmental Panel on Climate Change [Core Writing Team, R. K. Pachauri, and A. Reisinger, (eds.)], IPCC, Geneva, Switzerland, 104 pp.

[2] IPCC, 2014: Summary for Policymakers. In: Climate Change 2014: Mitigation of Climate Change. Contribution of Working Group III to the Fifth Assessment Report of the Intergovernmental Panel on Climate Change [Edenhofer, O., R. Pichs-Madruga, Y. Sokona, E. Farahani, S. Kadner, K. Seyboth, A. Adler, I. Baum, S. Brunner, P. Eickemeier, B. Kriemann, J. Savolainen, S. Schlömer, C. von Stechow, T. Zwickel and J. C. Minx (eds.) Cambridge University Press, Cambridge, United Kingdom and New York, NY, USA.

[3] Plan Bleu, “Climate change and energy in the Mediterranean Plan Bleu - Regional Activity Center, Sophia Antipolis, July 2008.

[4] T. R. Oke, G. T. Johnson, D. G. Steyn, and I. D. Watson, “Simulation of surface urban heat islands under ‘’ ‘ideal’ conditions at night: Part 2. Diagnosis of causation, Boundary Layer Meteorol. 56, 1991,pp. 339–358.

[5] M. Santamouris (Ed.), Energy and Climate in the Urban Built Environment, London, James and James Science Publishers, 2001.

[6] D. Stewart, “A systematic review and scientific critique of methodology in modern urban heat island literature”, International Journal of Climatology, Special Issue: ICUC-7 Urban Climate Meeting 2011, 31(2), pp. 200–217.

[7] D. K. Papanastasiou, and C. Kittas, “Maximum urban heat island intensity in a medium-sized coastal Mediterranean city,” Theoretical and Applied Climatology, 107 (3–4) , 2012, pp. 407–416.

[8] P. Coseo, and L. Larsen, “How factors of land use/land cover, building configuration, and adjacent heat sources and sinks explain urban heat islands in Chicago”, Landscape and Urban Planning, Vol. 125, May 2014, pp. 117-129.

[9] M. Kolokotroni, X. Ren, M. Davies, and A. Mavrogianni, “London’s urban heat island: impact on current and future energy consumption in office buildings”, Energy and Buildings, 47, 2012, pp. 302–311.

[10] H. Akbari, and S. Konopacki, “Energy effects of heat-island reduction strategies in Toronto, Canada”, Energy and Buildings, 29, 2004, pp. 191–210.

[11] M. Santamouris, N. Papanikolaou, I. Livada, I. Koronakis, C. Georgakis, A. Argiriou, and D. N. Assimakopoulos, “On the impact of urban climate to the energy consumption of buildings”, Solar Energy, 70 (3), 2001, pp. 201–216.

[12] E. Carnielo, and M. Zinzi, “Optical and thermal characterisation of cool asphalts to mitigate urban temperatures and building cooling demand”, Building and Environment, 60, 2013, pp. 56–65.

[13] TRNSYS 16; www.trnsys.com.

Journal of Renewable Energy and Sustainable Development (RESD) Volume 2, Issue 1, June 2016 - ISSN 2356-8569
http://dx.doi.org/10.21622/RESD.2016.02.1.052

Asymmetric Fuzzy Logic Controlled DC-DC Converter for Solar Energy system

Mohamed Boutouba*, Abdelghani El Ougli*, Sabah Miqoi* And Belkassem Tidhaf*
* ENSA Oujda, Faculty of Science, UMP Oujda Morocco.
E-mail: btba.med@gmail.com

***Abstract* -** In this paper, a controlled voltage system for a solar energy source is presented by a new command called fuzzy logic controller (FLC) via a DC-DC converter. The fuzzy logic control is selected due its performance and efficiency even for nonlinear systems such as the DC-DC converters.

A simulation with MATLAB SIMULINK environment of the FL control system, compared with a classical PI controller, is presented at the end of the paper to illustrate the good behavior of the control.

***Keywords* -** Buck and Boost converter, PI Fuzzy logic controller (FLC), photovoltaic (PV), voltage regulation.

I. INTRODUCTION

Adaptation of the voltage and current between sources and loads is the main task of DC-DC converters. They are used in many different industry applications due to the advantage of low power loss and best yield; therefore their studies have become more interesting in recent years.

Because of nonlinearity of DC-DC converters, conventional techniques of linearization remain unable to describe and control the system, this results in reducing the system performance or instability. To solve this problem, an approach of a fuzzy logic control has been proposed as an alternative solution for non-linear system whose linearization is hard to find.

The studied system is powered by a photovoltaic voltage source along with using different kinds of loads, as shown in Fig. 1.

For photovoltaic source energy, the level of production energy is unstable and unpredictable because it depends on the level of irradiation and temperature.

This has the effect of changing the solar panel voltage and then the output voltage (at the load). To ensure the stability of the desired output voltage, a regulation block is needed as an intermediary between the panel and the load. The Fuzzy logic control for DC-DC converters, which is the goal of this work, will intervene to keep the output to the given value even if the load, the input voltage or the desired voltage change.

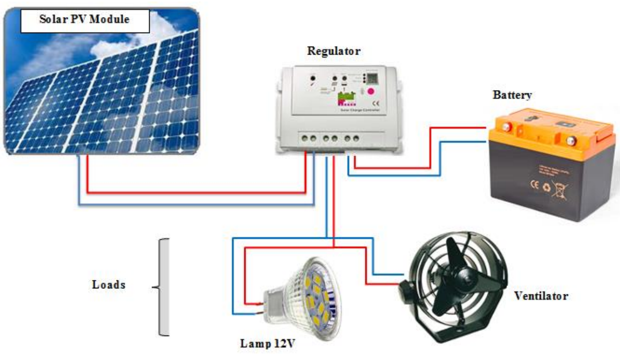

Fig .1. PV supply voltage for various loads.

The purpose of this process control is to maintain the state of a physical or electrical quantity stable, without human intervention, for a desired given value called the set point, per share on a manipulated variable.

The Fig. 2 presents the general block of a control system:

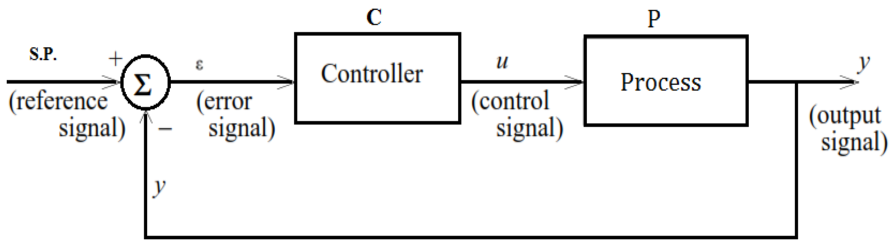

Fig .2. Block diagram of a controller process.

Where:

- ***S.P.*** : Set point, it is the desired output signal, also called reference (a voltage in proposed case).
- ***C*** : is the controller or corrector, namely the block that allows the control of the output voltage.
- ***P*** : process to control; a DC-DC converter in proposed case.
- ε **:** It is the error between the Set point (SP) and the measured value of the output y: $\varepsilon = SP - y$.
- u : The control signal generated by the controller.

The block calculates an error value that is equal to the difference between the measured process variable and the desired set point. The controller attempts to minimize the error by adjusting the process through the use of a manipulated variable: the control signal .

II. BUCK AND BOOST CONVERTER SYSTEM DESCRIPTION:

Fig. 3 shows the electronic circuit of the Buck and Boost converter. A resistive load that is called R_{Ch} is used, the output as V_{out} , and the set point or reference voltage as V_{ref}.

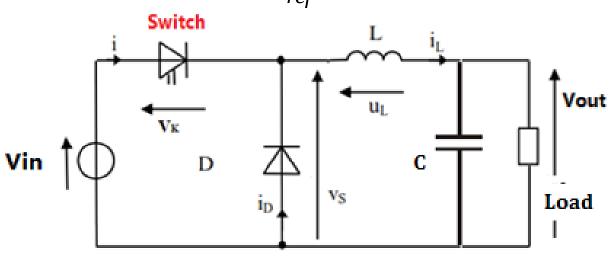

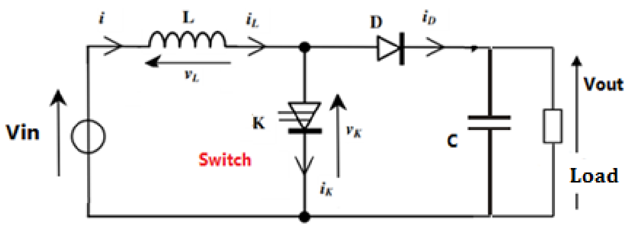

Fig .3. Topology of the buck and Boost converter respectively.

The electronic switch is controlled by a PWM signal (*Pulse Width Modulation*) whose duty cycle $\alpha = t_{ON}/T$.

- t_{ON} is the time with which the switch is on, and T represents the period of the switch control signal.

The circuit equations are written as bellow

$$\begin{cases} V_{out} = \alpha . V_{in} \\ I_{out} = \dfrac{I_{in}}{\alpha} \end{cases} \quad \text{for Buck converter} \qquad (1)$$

$$\begin{cases} V_{out} = \dfrac{V_{in}}{1-\alpha} \\ I_{out} = (1-\alpha).I_{in} \end{cases} \quad \text{for Boost converter} \qquad (2)$$

From the equations it becomes clear that it is possible to control the output voltage of a PWM signal whose duty cycle is variable according to the need.

The inductance is used for smoothing the chopped current that crosses it, thus reducing the ripple; it must have an induction factor greater than a critical value to ensure continuous conduction, avoid the cancellation of the current and guarantee the proper functioning of the circuit.

The critical value is calculated with $\alpha = 0.5$ when the ripple current is maximum $\Delta i_L(\max)$

$$L \geq L_{\min} = \frac{V_{in}}{4 f \Delta i_L(\max)} \qquad (3)$$

- f : Switching frequency.

III. CONTROL SYSTEM

The use of traditional corrector: proportional, integral and derivative , denoted P, I, and D to control a system is effective, but stay ineffective in front of the

Journal of Renewable Energy and Sustainable Development (RESD) Volume 2, Issue 1, June 2016 - ISSN 2356-8569
http://dx.doi.org/10.21622/RESD.2016.02.1.052

nonlinear system whose study becomes more complex. That is why this method is generally recommended for linear systems of which it is possible to describe in equations.

DC-DC converters have this problem of nonlinearity hence the interest to seek an alternative to these traditional correctors: a fuzzy logic controller (FLC), a relevant strategy offering outstanding performance and an interesting alternative approach such a raisonnement similar to that of man, and to manage complex systems intuitively.

Fuzzy logic allows reasoning not on numeric variables, but on linguistic variables, i.e., on qualitative variables (large, small, medium, far, near, etc.). The fact of reasoning about these linguistic variables will allow manipulating knowledge in natural language. The only thing which can be introduced in the system is what is called inference rules which are expressed in natural language.

As shown in Fig. 4, the fuzzy logic controller block is divided into three sub block: Fuzzification, fuzzy inference engine with rules, and defuzzification.

A. PI Fuzzy logic controller

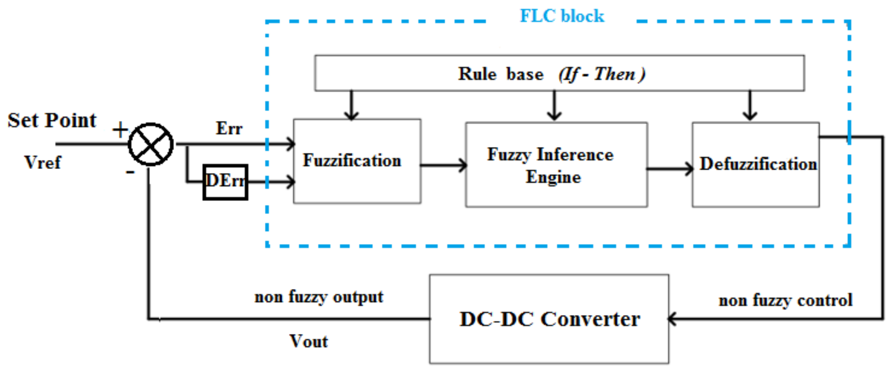

Fig .4. Block diagram of a PI fuzzy controller

B. Fuzzification

The input and output variables chosen to model the system are numerical quantities. The fuzzification step is to transform the actual magnitudes linguistic variables for an inference processing. Thus, for each input and output variable there are associated sets, characterizing the linguistic terms taken by these variables. These terms will be used to write the rules of inference.

The linguistic variables -as shown in Fig. 5- are modeled in the form of a function, called membership function; the choice of the form is arbitrary. The most frequently used fuzzy control shape is the triangular shape.

In this paper, a PI controller has been used, it has as inputs: the error and the change of error:

$$E = \varepsilon = V_{ref} - V_{out} \qquad (4)$$
$$DE = \Delta\varepsilon = \varepsilon(t) - \varepsilon(t-1)$$

Seven memberships for each input and output are used (Asymmetric ones for input "error" and the output), where N and G mean negative and positive. B, M, S And ZO are respectively: Big, Medium, Small and Zero.

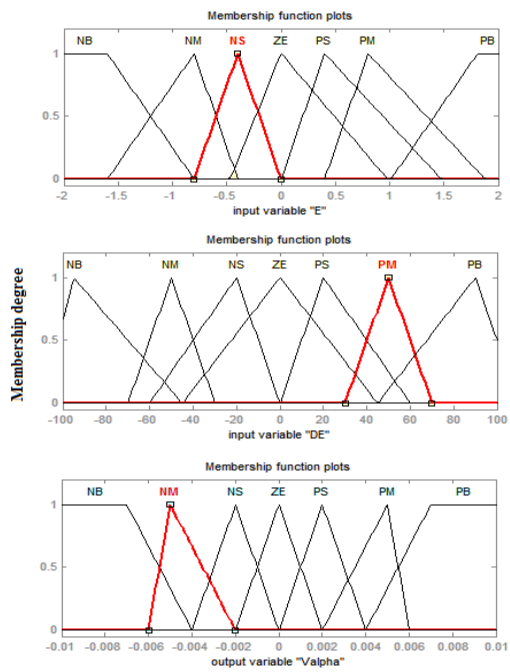

Fig .5. Variables inputs/output linguistic

C. Rules base

A fuzzy rule base is a collection of rules that allows linking the fuzzy variables of input and output. The description of the control is via these rules; it has the following form:

- If E is NS and DE is PM, then dValpha is NM.

Corresponds to: If the error is negative and the error variation is fairly large, then the duty cycle will be decreased.

These rules can be presented as in Table 1. A graphic view of output response according to the inputs is shown in Fig. 6.

D. Fuzzy inference engine

It allows calculating the fuzzy set associated with the command, and is done with fuzzy inference operations and rules aggregation. For each rule, the fuzzy inference is based on the use of a fuzzy implication operator.

This operator quantifies the binding strength between the premises and the conclusion of the rules.

There are many ways to express inferences: by linguistic description, matrix or array of inference.

Mamdani's fuzzy inference method is the most commonly used and is based on the recovery of the minimum value of the degrees of membership of the input variables. It allows calculating the fuzzy set associated with the command and is done with fuzzy inference operations and rules aggregation.

Consider the previous example:

$$\mu_{NM}(V_\alpha)=\min(\mu_{NS}(\varepsilon),\mu_{PM}(\Delta\varepsilon)) \quad (5)$$

Table 1. Fuzzy rules

DE	E: NB	NM	NS	ZE	PS	PM	PB
NB	ZE	ZE	ZE	PS	PM	PB	PB
NM	NS	ZE	ZE	PS	PM	PB	PB
NS	NM	NS	NS	ZE	PS	PM	PB
ZE	NB	NM	NS	ZE	PS	PS	PB
PS	NB	NM	NS	NS	ZE	PS	PM
PM	NB	NB	NM	NS	PS	ZE	PM
PB	NB	NB	NB	NB	PS	ZE	ZE

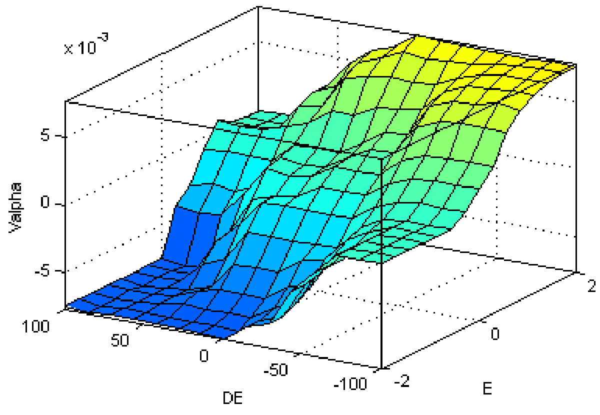

Fig .6. Control Surface View.

E. Defuzzification

After the inference step, the overall result is a fuzzy value. This result should be defuzzifed to obtain a final crisp or non-fuzzy output. There are several defuzzification methods to achieve, such as: the mean of maxima, the center of areas, and the center of maxima.
Center of gravity (area) is the most prevalent and physically appealing of all the defuzzification methods.

The general expression of the center of area is given by the equation:

$$dV_\alpha = \frac{\sum_i \mu(x(i)).x(i)}{\sum_i \mu(x(i))} \quad (6)$$

- $x(i)$: Output variable equivalent to $dV_\alpha(i)$
- $\mu(x(i))$: Membership degree for sampled value of the output.
- i : Sample of the interval of the output variable.

The obtained signal is defined by the following relationship:

$$V_\alpha(t) = V_\alpha(t-1) + dV_\alpha \quad (7)$$

It is an analog signal which is incremented or decremented by the output of the FLC controller dV_α .
The signal is proportional to the desired duty cycle.

Another block comes after to convert the output signal in a PWM signal via a comparator block with a sawtooth signal, to order and control DC-DC converter as shown in Fig. 7.

Journal of Renewable Energy and Sustainable Development (RESD) Volume 2, Issue 1, June 2016 - ISSN 2356-8569
http://dx.doi.org/10.21622/RESD.2016.02.1.052

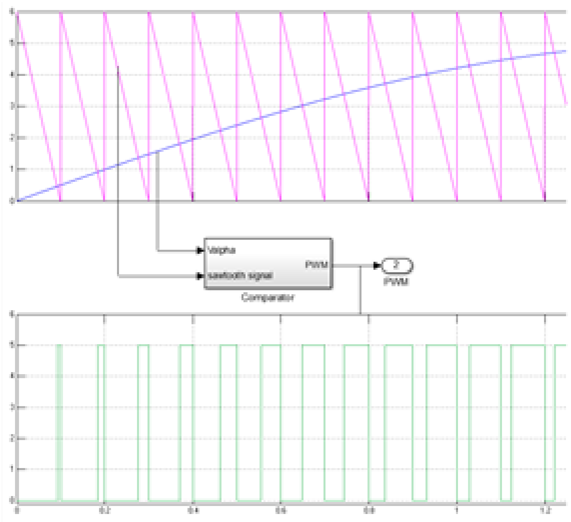

Fig .7. PWM signal generator.

IV. SIMULATION RESULT OF BUCK CONVERTER WITH FLC ON MATLAB SIMULINK

The complete circuit studied in this article using the MATLAB SIMULINK is shown in Fig. 8.

The simulation parameters used in these simulations are shown in Table 2:

Switching Frequency	$f = 10KHz$
Filter Inductance	$H = 4mH$ with $r_L = 2m\Omega$
Filter Capacitance	$C = 560\mu F$
Kp and **Ki** for the FL control are respectively	0.0125 ; 0.067

To verify the proper functioning of the control system by fuzzy logic, several simulations were processed and compared with a classical PI control, in presence of modification of some variables.

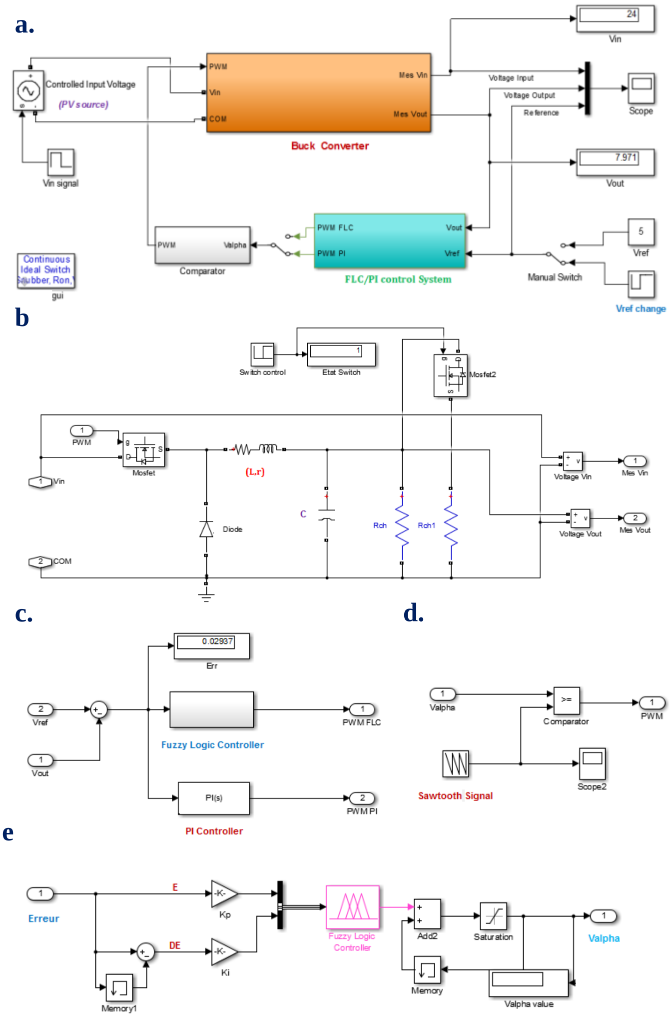

Fig .8. a. Buck converter with FLC/PI controller.
b. Buck converter topology.
c. FLC and PI block controller.
d. PWM generator.
e. FLC structure.

A. Speed pursuit of the reference voltage (set point) in presence of an irregular voltage source

For this simulation the load is fixed to $R_{ch} = 10\Omega$, reference voltage to $V_{ref} = 5V$. The circuit is powered by a voltage variable in time as follows:

$$V_{in} = \begin{cases} 24V & 0 \le t \le 0.5s \\ 20V & t > 0.5s \end{cases}$$

The result in Fig. 9 shows the evolution of the output voltage and its pursuit to the set point (reference voltage) for the two control commands.

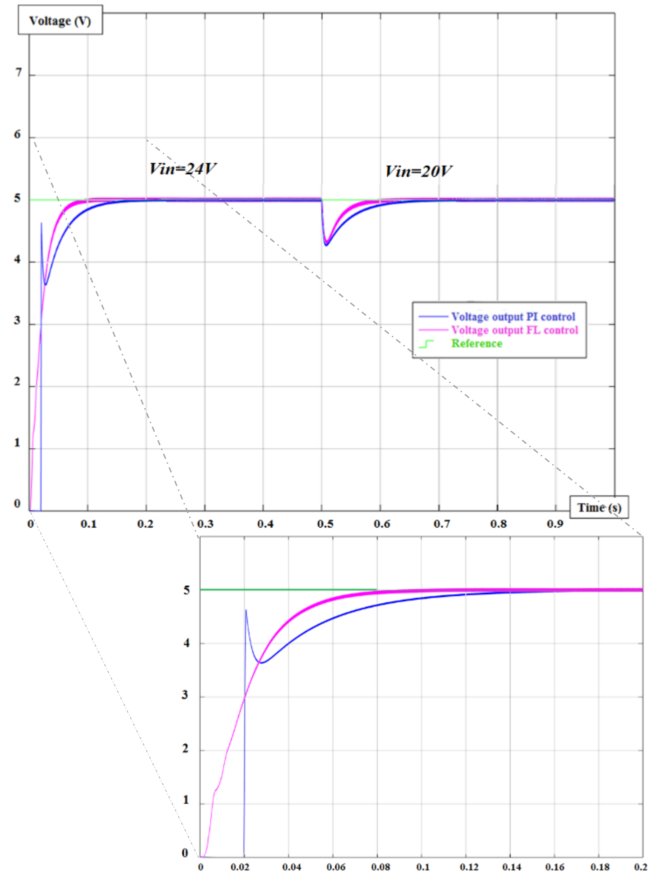

Fig .9. Simulation with irregular supply voltage.

As shown, the response time for the fuzzy-PI control compared with the classical one is better: respectively $0.1s$ against $0.15s$.

At $t = 0.5s$, the input voltage drop from ***24V*** to ***20V*** causes a loss of voltage output. Quickly, the FLC changes the duty cycle to correct the error, and then brings back the output voltage to the desired value for a reduced response time $t_r < 0.1s$ for the FLC against $0.15s$ for the classical PI control.

B. Variable set point pursuit

In this second simulation, the simulation parameters are given as follows:

$V_{in} = 24V$ and $R_{ch} = 10\Omega$ with a reference voltage

$$V_{ref} = \begin{cases} 5V & 0 \le t \le 0.5s \\ 8V & t > 0.5s \end{cases}$$

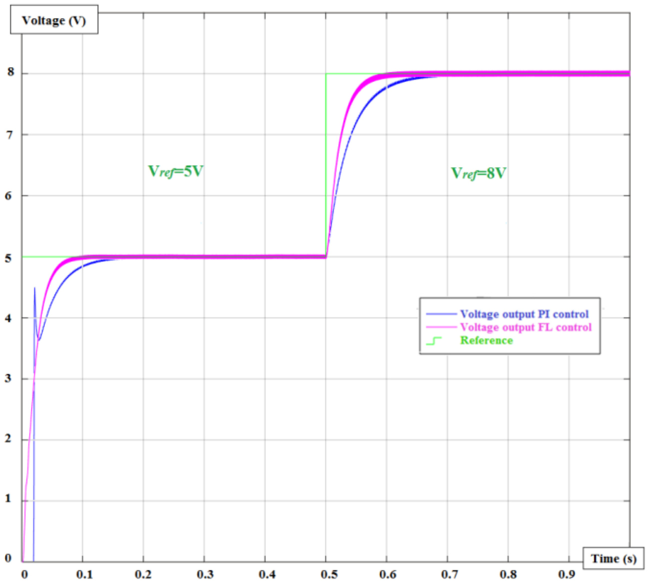

Fig .10. Simulation with variable set point.

Fig. 10 shows again the pursuit of the fuzzy system even if the set point changes during the simulation, the output voltage follows the new set point once it is changed.

C. Simulation with a variable load

The output voltage for a control process has to be independent of the choice of the load. The system should keep at any instant the output voltage close to the set point even when the load changes.

It is the case of the studied control system: during the simulation, whose result is presented in Fig. 11, at $t = 0.5s$ the load changes from $R_{ch} = 10\Omega$ to 5Ω.

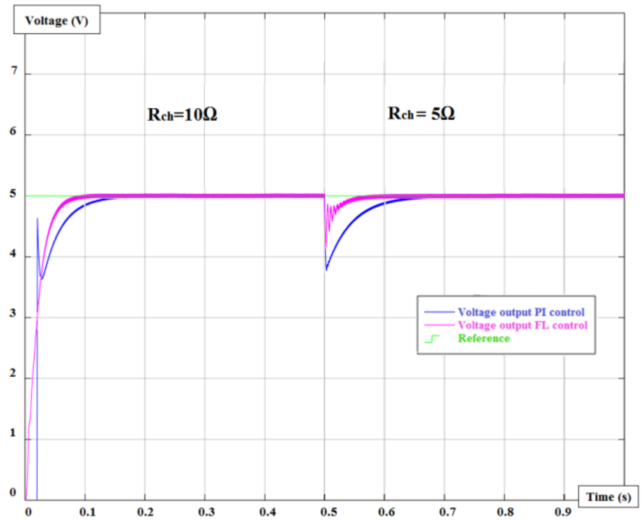

Fig .11. System Response with a variable Load.

http://dx.doi.org/10.21622/RESD.2016.02.1.052

It is concluded that, the PI-Fuzzy control guarantees the pursuit of the set point voltage in a reduced time compared to the conventional PI control.

D. Precision

Among the major points in the regulatory system is the precision. A system whose output is far from the set point is considered nonfunctional. The system presents the study advantage to have a reinforced precision as shown in Fig. 12, case of $V_{in} = 24V$ and $R_{ch} = 10\Omega$.

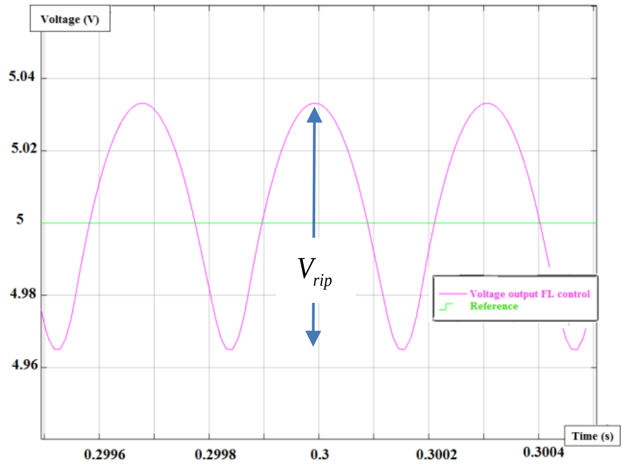

Fig .12. Output voltage ripple.

According to the figure, the ripple rate is given by:

$$\eta = {V_{rip}}/{V_{ref}} = {35\times10^{-3}}/{5} = 0.7\% \quad (8)$$

Too low rate means better precision.

V. CONCLUSION

In this paper, an alternative of an order for voltage regulation via a DC-DC converter was proposed, powered by an irregular source voltage as photovoltaic.

To illustrate the work, several simulations were treated under MATLAB SIMULINK environment for a Buck converter equipped with a Fuzzy PI Controller (FLC) against a classical PI control. The analysis given can extend this work to other converters (boost converter, buck-boost converter, etc.).

The obtained results strongly confirm the effectiveness of the proposed control process system, which has both: high precision and a set point tracking speed.

REFERENCES

[1] Cetin Elmas, Omer Deperlioglu, Hasan Huseyin Sayan, “Adaptive fuzzy logic controller for DC–DC converters”, Expert Systems with Applications, Vol 36, Issue 2, Part 1, March 2009, pp. 1540-1548. ISSN 0957 4174.

[2] First K.V.Hari Prasad; Second CH.Uma Maheswar Rao; Third A.Sri Hari; Dept. of Electrical Engineering, Vignan University. “Design and simulation of a fuzzy logic controller for buck & boost converters,” International Journal of Advanced Technology & Engineering Research (IJATER). Vol. 2, Issue3. MAY 2012, pp. 218-224, ISSN 2250-3536.

[3] Dr.T.Govindaraj, Rasila R, Muthayammal Engineering College, Rasipuram, Tamil Nadu, India. “Development of fuzzy logic controller for DC – DC buck converters,” Int J Engg Techsci Vol. 2, no.2 2011, pp. 192-198.

[4] Sahin, M.E. ; Dept. of Phys., Univ. of Rize, Rize, Turkey ; Okumus, H.I. “Fuzzy logic controlled buck-boost DC-DC converter for solar energy-battery system,” Innovations in Intelligent Systems and Applications (INISTA), 2011 International Symposium on. 15-18 June 2011 IEEE, pp. 394 – 397.

[5] Cheng-Shion Shieh, “Fuzzy PWM based on Genetic Algorithm for battery charging,” Applied Soft Computing, Vol. 21, August 2014, pp. 607-616, ISSN 1568-4946.

[6] Mamun Rabbani, Student Member IEEE, H. M. Mesbah Maruf, Tanvir Ahmed, Md. Ashfanoor Kabir, Member IEEE, y Upal Mahbub, Bangladesh University of Engineering and Technology. “Fuzzy logic driven adaptive PID controller for PWM based buck converter,” IEEE/OSA/IAPR International Conference on Informatics, Electronics & Vision. 18-19 May 2012.

[7] Liping Guo, John Y. Hung, R.M. Nelms, “Design of a fuzzy controller using variable structure approach for application to DC–DC converters,” Electric Power Systems Research, Vol. 83, Issue 1, February 2012, pp. 104-109, ISSN 0378-7796.

[8] Ahmad El Khateb, Member, IEEE, Nasrudin Abd Rahim, Senior Member, IEEE, Jeyraj Selvaraj, and M. Nasir Uddin, Senior Member, IEEE. “Fuzzy logic controller based SEPIC converter for maximum power point tracking,” IEEE Transactions on industry applications, Vol. 50, Issue 4, Feb 2014, pp. 99.

[9] Augusti Lindiya, S. Palani, Iyyappan, “Performance comparison of various controllers for dc-dc synchronous buck converter,” Procedia Engineering, Vol. 38, 2012, pp. 2679-2693, ISSN 1877-7058.

[10] Chaoui, H.; Miah, S.; Sicard, P., “Adaptive fuzzy logic control of a DC-DC boost converter with large parametric and load uncertainties,” Advanced Intelligent Mechatronics (AIM), 2010 IEEE/ASME International Conference on, Montreal, ON, 6-9 July 2010, pp. 575-580.

[11] Qing Wang; Chuang-Yuan Chang; Long-Xing Shi, “Design of adaptive fuzzy logic controller for auto-adjustable DC-DC converters,” Solid-State and Integrated Circuit Technology (ICSICT), 2010 10th IEEE International Conference on, 1-4 Nov. 2010, pp. 469-471.

Scan the QR Code

Journal of
Renewable Energy and Sustainable Development

RESD

Volume 2 Issue 1, June 2016 ISSN 2356-8569

ISSN 2356-8518

http://apc.aast.edu

مركز الأكاديمية للنشر
ACADEMY Publishing Center